An observational and theoretical study of the structure and propagation of the Madden-Julian Oscillation

Ángel F. Adames

A dissertation submitted in partial fulfillment of
the requirements for the degree of

Doctor of Philosophy

University of Washington

2016

Reading Committee:

John M. Wallace, Chair

Daehyun Kim, Chair

Christopher S. Bretherton

Program Authorized to Offer Degree:
Atmospheric Sciences

University of Washington

Abstract

An observational and theoretical study of the structure and propagation of the Madden-Julian Oscillation

Ángel F. Adames

Co-Chairs of the Supervisory Committee:
Title of Chair John M. Wallace
Atmospheric Sciences

Title of Chair Daehyun Kim
Atmospheric Sciences

This study is composed of two parts. In the first part of this dissertation, the large-scale circulation features that determine the structure and evolution of MJO-related moisture and precipitation fields are examined using a linear analysis protocol based on daily 850- minus 150-hPa global velocity potential data. The analysis is augmented by a compositing procedure that emphasizes the structural features over the Indo-Pacific warm pool sector (60°E−180°) that give rise to the eastward propagation of the enhanced moisture and precipitation.

It is found that boundary layer (BL) convergence in the low level easterlies to the east of the region of maximum ascent produces a deep but narrow plume of equatorial ascent that moistens the mid-troposphere, while weakly diffluent flow above the BL spreads moisture away from the equator. Vertical advection of moisture from this plume of ascent accounts for the eastward propagation of the positive moisture anomalies across the Maritime Continent into the western Pacific. When the convection is first developing over the Indian Ocean, horizontal moisture advection contributes to both the eastward propagation and the amplification of the positive moisture anomalies along the equator to the east of the region of enhanced convection.

The results of the first part of the dissertation are used to develop a linear wave theory for the MJO, shown in part two. The theory is largely based on a framework previously developed by Sobel and Maloney. In this treatment, column moisture is the only prognostic variable and the horizontal wind is diagnosed as the forced Kelvin and Rossby wave responses to an equatorial heat source/sink. In contrast to the original framework, the meridional and vertical structure of the basic equations are treated explicitly, and values of several key model parameters are adjusted, based on observations.

A dispersion relation is derived that adequately describes the MJO's signal in the wavenumber-frequency spectrum and defines the MJO as a dispersive equatorial moist wave with a westward group velocity. On the basis of linear regression analysis of satellite and reanalysis data, it is estimated that the MJO's group velocity is $\sim$40% as large as its phase speed. This dispersion is the result of the anomalous winds in the wave modulating the mean distribution of moisture such that the moisture anomaly propagates eastward while wave activity propagates westward.

The moist wave grows through feedbacks involving moisture, clouds and radiation, and is damped by the advection of moisture associated with the Rossby wave. Additionally, a zonal wavenumber dependence is found in cloud-radiation feedbacks which causes growth to be strongest at planetary scales. Our results suggest that this wavenumber dependence arises from the non-local nature of cloud-radiation feedbacks; that is, anomalous convection spreads upper-level clouds and reduces radiative cooling over an extensive area surrounding the anomalous precipitation.

TABLE OF CONTENTS

LIST OF FIGURES

LIST OF TABLES

ACKNOWLEDGMENTS

I would like to thank the endless support and patience from the chairs of my committee, Mike Wallace and Daehyun Kim. I would also like to extend my gratitude to my committee: Chris Bretherton, Dennis Hartmann, Bob Houze, Eric D'Asaro for useful comments and constructive conversations I've had with them over the course of the PhD. Numerous reviewers have challenged and given important feedback that has helped improve the science of this thesis and its related publications.

I would like to also thank the endless support I have received from my family, in particular my parents, as well as the friends I have made in Puerto Rico and Seattle. Your support has been critical in my completing the PhD.

Finally, I would like to thank all the friends that I have made throughout my life, especially those that have stayed in touch throughout the years. Too many to count, I thank you for your friendship, your patience and for always pushing me to new limits.

DEDICATION

To my parents, Diana and Ángel David, my brothers Ángel Ricardo (Richi), Ángel Sigfredo (Angelo) and my grandmother Judith (Yiyí).

Chapter 1

INTRODUCTION

The Madden-Julian Oscillation (MJO, after Madden and Julian 1971, 1972) is the dominant mode of tropical intraseasonal variability. It is a distinct type of convectively coupled tropical wave that is characterized by: (i) a zonal scale of several thousand kilometers, (ii) a phase speed of about 5 m s^{-1}, and (iii) eastward propagation. The MJO's slow rate of eastward propagation and the similarity of its horizontal structure to the wave response to an equatorial heat source (Matsuno, 1966; Gill, 1980), suggests that the interaction between large-scale motions and diabatic heating associated with deep convection plays a central role in its dynamics. The early theoretical study of Lau and Peng (1987) invoked wave-induced convective instability of the second kind (wave-CISK, Lindzen 1974), an extension of the original CISK idea by Charney and Eliassen (1964) in an effort to model this interaction. Neither wave-CISK nor any other wave-convection coupling mechanism proposed thereafter has been proven capable of realistically simulating the aforementioned characteristics of the MJO, and it is not yet clear what are the processes that explain the distribution, morphology, and eastward propagation of its envelope of deep convection. Some authors have emphasized the processes that moisten and dry the air column in the vicinity of individual cloud clusters while others have emphasized the role of the instantaneous, planetary-scale wind field. In order to improve MJO simulation, a better understanding of the fundamental processes driving its dynamics is required.

The deep tropics are characterized by weak spatial and temporal variability in temperature and surface pressure and large variability in free-tropospheric moisture and precipitation (Charney, 1963; Sobel and Bretherton, 2000). Held et al. (1993) noted that regions of precipitation are characterized by enhanced column-integrated water vapor, and concluded that

water vapor provides the "memory" necessary to ensure the development and maintenance of convection over an isolated region. Subsequent studies by Bretherton et al. (2004); Holloway and Neelin (2009); Muller et al. (2009); among others, have reported strong correlations between tropical precipitation and column-integrated water vapor, and similar correlations have been found in the convectively active phase of the MJO. Analysis of satellite data by Myers and Waliser (2003), and Jiang et al. (2011), and in-situ observations by Johnson and Ciesielski (2013), and Xu and Rutledge (2014) suggest that the MJO modulates the free-tropospheric moisture profile, which then influences both the frequency of occurrence and the morphology of large-scale organized convection. These results have inspired a number of authors to construct models of the MJO in which convection is strongly coupled to the moisture field (Raymond and Fuchs, 2009; Majda and Stechmann, 2009; Sobel and Maloney, 2013).

There is a growing body of theoretical work in which the MJO is considered to be a "moisture mode" (Neelin and Yu 1994; Raymond 2000b, 2001; Sobel et al. 2001; Sobel and Gildor 2003; Fuchs and Raymond 2002, 2005, 2007; Sugiyama 2009a,b; Majda and Stechmann 2009; Sobel and Maloney 2012, 2013; Sukhatme 2014). In the moisture mode paradigm, humidity anomalies are of first order importance, convection is assumed to be tightly coupled to column-integrated water vapor (Bretherton et al., 2004), and temporal and horizontal variations in temperature are often neglected, which is referred to as the weak temperature gradient (WTG) approximation (Charney, 1963; Sobel et al., 2001). Under these approximations, the processes that determine the growth and propagation of the large-scale moisture envelope also explain those of the MJO.

Several mechanisms have been proposed to explain the moistening of the free troposphere prior to the onset of deep convection. Benedict and Randall (2007) argued that cloud-related moisture fluxes gradually moisten the lower troposphere to the east of the rain area, causing the rain area to propagate eastward. Other studies have focused on the role of the large-scale circulation in organizing the moisture field. Maloney (2009); Pritchard and Bretherton (2014); DeMott et al. (2014); and Zhu and Hendon (2015) attributed the moistening to the

east of the region of strongest ascent to anomalous horizontal moisture advection. Wang (1988); Seo and Wang (2010), and Hsu and Li (2012) proposed that frictionally-driven moisture convergence, in association with planetary-scale equatorial waves, moistens the lower troposphere to the east of the rain area.

This study seeks to elucidate the mechanisms responsible for the eastward propagation of the MJO, and use these results to expand on our current understanding of MJO theory. The analysis in this study is separated into two parts.

In Part I, we will make use of a time varying MJO index based on the difference between 850 and 150 hPa velocity potential to analyze the planetary-scale structure of the MJO and elucidate the processes that lead to the eastward propagation of the rain area. We will show in Chapter 3 that the equatorial vertical velocity anomaly field (ω) can be represented in terms of two orthogonal modal structures. The leading mode (ω_1) is dominated by a deep overturning circulation in the zonal plane while the second mode (ω_2) is related to shallow overturning circulations in the meridional plane that are driven by friction in the boundary layer (BL, 850$-$1000 hPa). We will show evidence that the forced, planetary wave response to an equatorial heat source consisting of equatorial Kelvin and Rossby waves (Gill, 1980) gives rise to an equatorially-trapped region of shallow ascent to the east of the region of enhanced rainfall, as in the frictional convergence mechanism proposed by Wang (1988). The band of ascent widens, deepens and eventually becomes elevated toward the west, exhibiting a characteristic "swallowtail" shape when viewed from above.

In Chapter 4 we show the evolving three-dimensional structure of the moisture field in the MJO and identify the dynamical processes that produce moistening and drying. The three essential ingredients that determine the evolution of moisture are shown to be: (1) deep tropospheric ascent associated with the zonal overturning circulation in the equatorial plane, (2) meridional advection of moisture in the Rossby wave cyclones and anticyclones in the lower free troposphere and (3) shallow, frictionally-induced, meridional circulations associated with the easterly and westerly wind anomalies in the Kelvin and Rossby waves to the east and west of the heat source.

Most of the plots shown in Part I are based on the compositing scheme that averages the three-dimensional structure of the MJO as it propagates eastward across the Indo-Pacific warm pool. This "warm pool composite" yields a robust description that elucidates structural elements of the MJO that might otherwise be obscured by sampling variability and therefore be difficult to interpret in maps and cross-sections for instantaneous MJO phases. We also extend the use of the warm pool compositing technique by using it to reconstruct the evolution of the MJO, yielding a cleaner, more concise representation of its structure at the time when its rainfall anomalies are characterized as a dipole with enhanced convection centered over the Indian Ocean and suppressed convection over the western Pacific.

In Part II, we will use the results of Part I to build upon the linear theoretical model of (Sobel and Maloney (2012, 2013), from here on collectively referred to as SM), which will enable us to obtain a more robust theoretical representation of the MJO. The model of SM uses zonally-varying column-integrated water vapor as the single prognostic variable to represent the processes that modulate the large-scale, low-frequency moisture variability. The linearity of their theory makes it possible to analytically estimate the contribution of the processes that lead to the growth and propagation of the MJO. The modified framework presented in this study explains the most salient characteristics of the MJO, including:a dispersion relationship for the wave and a potential mechanism for horizontal scale-selection.

Chapter 2

DATA AND METHODS

The data and methods used in this study closely follow those used in AW1 and AW2. We make use of the 1.5° longitude × 1.5° latitude horizontal resolution, 00Z daily surface and pressure level fields in the ERA-Interim dataset (Dee et al. 2011) for the 33-yr time period 1979 through 2011. The horizontal wind components (u, v) are used in this study as field variables and in the calculation of velocity potential (χ), and divergence (Div). Specific humidity (q), vertical velocity (ω), and surface and top of atmosphere longwave radiative fluxes (Q_{LW}) are also used as field variables and for the calculation of the terms in the moisture budget tendency equation. For pressure level fields, we use all 29 pressure levels from 1000 to 50 hPa. Unless otherwise noted, all the fields described in this study correspond to MJO-related anomalies. Fields involving products of individual ERA-Interim variables are also used in this study, as will be seen in Chapter 4. These products are calculated at each time step, and the procedure afterwards is identical to the individual fields discussed above.

We make use of outgoing longwave radiation (OLR) from NOAA's polar orbiting satellites (Liebmann and Smith, 1996) as an indicator of the extent of cold cloud tops associated with deep convection. The daily-averaged precipitation from the 3B42 version 7 product of the Tropical Rainfall Measurement Mission (TRMM-3B42, Huffman et al. 2007), based on the period of record from 1998-2011, is used in addition to the ERA-Interim product. This dataset is interpolated onto a 1.5° longitude × 1.5° latitude horizontal resolution to facilitate comparison with ERA-Interim data. Finally, in Part II we make use of column-integrated water vapor ($\langle q \rangle$), obtained from the daily, 0.25° horizontal resolution, combined precipitable water (PW) product from the Special Sensor Microwave Imager (SSM/I) and the Tropical

Rainfall Measurement Mission's Microwave Imager (TMI) (obtained from Remote Sensing Systems, http://www.remss.com/) for the time period 1998-2011. The temporal tendency in $\langle q \rangle$, $\partial \langle q \rangle / \partial t$ is calculated by taking the two-day centered differences in $\langle q \rangle$. For the MJO filtering procedure discussed below, the SSM/I-TMI PW anomalies have been interpolated in space in order to remove missing data over the land masses.

We remove the mean and first three harmonics of the annual cycle, based on the 1979-2011 reference period, and subtract out the running mean of the previous 120 days. Regression maps for each field are obtained through the equation:

$$\mathbf{D} = \mathbf{S}\hat{\mathbf{P}}^{\top}/N \tag{2.1}$$

where $\mathbf{S}$ is a two-dimensional matrix that represents a variable field S, $\hat{\mathbf{P}}$ is a standardized MJO index, $\mathbf{D}$ is the regression pattern for $\mathbf{S}$ upon $\hat{\mathbf{P}}$, expressed in dimensional units, and N is the sample size in days. Most of the patterns shown here are obtained by regressing fields upon MJO indices defined as linear combinations of the two leading principal components (PCs) of daily-mean, global fields of 850 minus 150 hPa velocity potential ($\Delta\chi$).

The OLR pattern observed in association with PC1 (Fig. 2.1*a*) is characterized by negative values, indicative of active convection centered over the Maritime Continent and positive values, indicative of sup- pressed convection, centered over South America. The 150-hPa wind anomalies are mainly zonal. The pattern is suggestive of an equatorial Kelvin wave signature that extends from the western Pacific to South America, but rather than being equatorially trapped, the band of westerlies extends out to well beyond 20°N/S. At this time in its cycle, the MJO exhibits a remarkable amount of symmetry with respect to the Maritime Continent (∼130°E), with the patterns west of the Dx maximum of nearly equal amplitude and opposing polarity to the patterns east of it. These results are qualitatively consis- tent with those obtained in previous studies of Knutson and Weickmann (1987); Hendon and Salby (1994); Matthews (2000); Sperber (2003); Kiladis et al. (2005). In the patterns based on PC2 of $\Delta\chi$ (Fig. 2.1*b*), the enhanced convection has propagated eastward

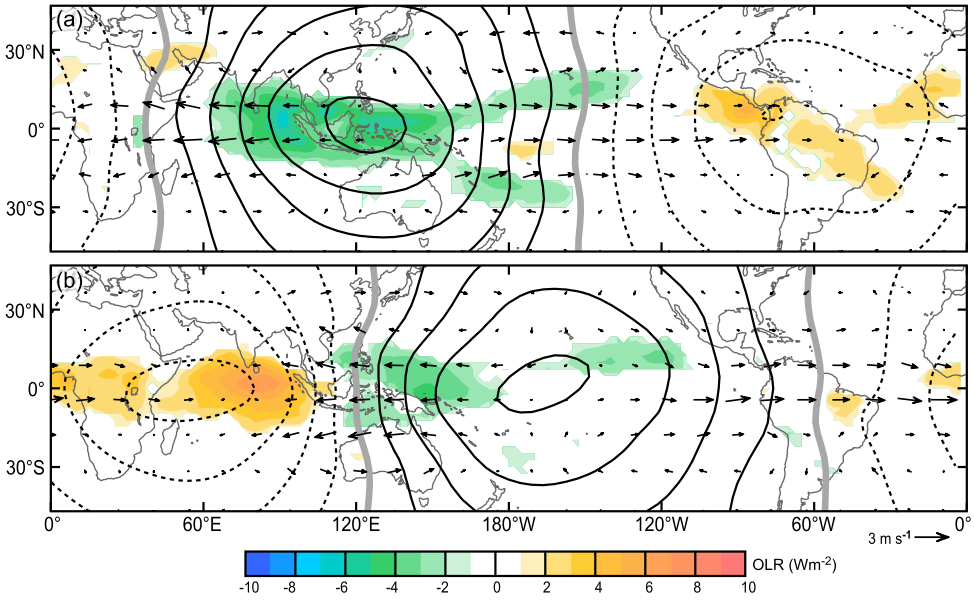

Figure 2.1: Leading EOFs of 850- minus 150-hPa velocity potential $\Delta\chi$ with the corresponding regression patterns for OLR (colored shading) and the total 150-hPa wind vectors (arrows) based on data for all 12 calendar months: (a) EOF1; (b) EOF2. Dashed (solid) contours denote negative (positive) $\Delta\chi$ anomalies and the gray contour depicts $\Delta\chi = 0$. Contour interval is 0.75 $\times 10^6$ m^2 s^{-1}.

into the western and central Pacific. The band of westerlies that was over the Pacific at the time of maximum PC1 become elongated and its front edge has nearly completed its circuit around the equatorial band and is seen returning to the Indian Ocean sector. At this time in the MJO cycle, westerlies span ∼3/4 of the tropical belt, and atmospheric angular momentum is at its peak (Weickmann and Sardeshmukh, 1994; Weickmann et al., 2000).

Most of the figures in Part I of this study are "warm pool composites". A warm pool composite is created as follows: We generate a series of regression maps based on linear combinations of PC1 and PC2 of $\Delta\chi$ for the MJO phases in which the $\Delta\chi$ maximum is centered over the Indo-Pacific warm pool (60°−180°E), as shown in the left column of Fig. 2.2. Each of these maps is then zonally shifted such that the longitude at which $\Delta\chi$ is a maximum corresponds to the reference longitude (0°). Compositing these shifted regression

maps yields a single map that describes the mean structure of MJO-related features as they propagate across the Indo-Pacific warm pool from 60°E to the Date Line, as shown in the right column of Fig. 2.2.

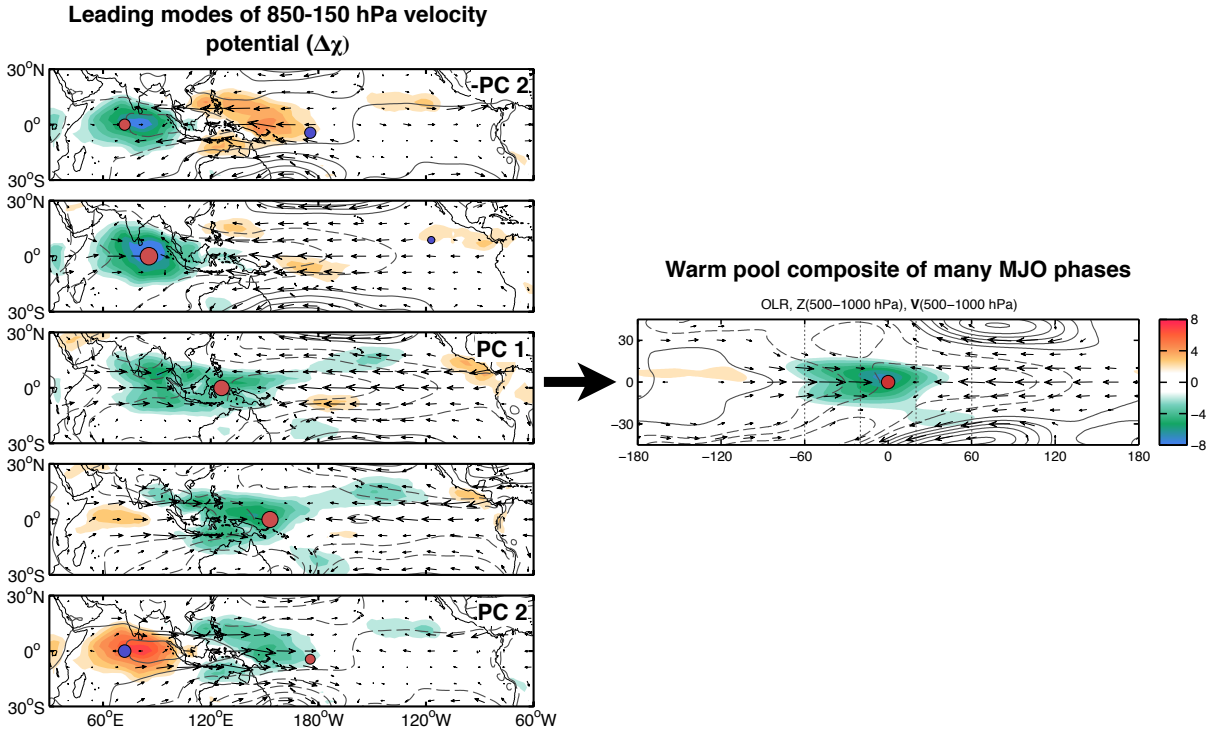

Figure 2.2: Example of the warm pool compositing procedure. Linear combinations of PC1 and PC2 $\Delta\chi$ (left coloum) are zonally shifted such that the longitude at which $\Delta\chi$ is a maximum corresponds to the reference longitude. These regression maps are then averaged to create the "warm pool composite" map, shown in the right column. Red and blue circles depict the regions where $\Delta\chi$ is a maximum and a minimum, respectively. The fields shown are OLR (shaded), and 500-1000 hPa layer averaged wind anomalies (arrows), 500-1000 hPa layer averaged geopotential height Z.

Results presented in this paper are based on data for all calendar months and the contour intervals in all the plots are scaled to the approximate value of the 95% confidence interval based on a two-sided t-test. The physical consistency of our results and their similarity to results of previous studies based on different analysis techniques also attests to their

statistical significance.

In Part II we estimate the phase speeds and group velocities of different MJO-related anomaly fields occurring within 25 days of the reference time (lag 0). These calculations are performed only for MJO-filtered anomalies in order to prevent smaller scale features such as interactions with the Maritime Continent from affecting these calculations. Choosing extrema that occur within 25 days of the reference time ensures that only the most representative anomalies are used in the calculation. Phase speeds are calculated for each time-longitude section by averaging the MJO-filtered anomaly fields across the longitude intervals ranging from 80°−100°E, 100°−120°E, 120°−140°E and 140°−160°E. The time when a statistically-significant extremum occurs is calculated within each interval for each field. Phase speed is then calculated by linear least squares fit for each propagating extremum. If multiple propagating envelopes are found, the phase speed is estimated by averaging all of them.

For the group velocity calculation, we calculate the zonal and temporal position of each local extremum. A local extremum is defined here as a local maximum/minimum occurring within 25 days of the reference time that is statistically significant at the 95% confidence interval. For a local maximum/minimum to be considered, it must be the largest anomaly in space and time within an interval of 10 days. Limiting the calculation to this time interval prevents more than one extremum to be obtained for a single propagating envelope. After all the local extrema are identified, the group velocity is calculated through a linear least squares fit.

For the spectral analysis shown in Chapter 5, we calculate the space-time power spectrum (P_{xx}) of NOAA OLR through the use of fast Fourier transforms (FFTs), as in Wheeler and Kiladis (1999), and Hendon and Wheeler (2008). We divide the time series of the anomaly fields into 180-day segments that overlap by 90 days, as in Waliser et al. (2009) and Kim et al. (2009). Then, the space-time mean and linear trends are removed by least squares fits and the ends of the series are tapered to zero through the use of a Hanning window. After tapering, the complex FFTs are computed in longitude and then in time. Finally, the power

spectrum is averaged over all segments and over the 15°N−15°S belt. The number of degrees of freedom is calculated to be 133 [2 (amplitude and phase) × 33 (years) × 365 (days)/180 (segment length)]. The signal strength is calculated as $(P_{xx} - P_{red})/P_{xx}$, where P_{red} is the red spectrum, calculated analytically using Eq. (1) of Masunaga (2007), and values above 0.4 are considered to be statistically significant in this study. We will show only the equatorially symmetric component (Yanai and Murakami, 1970) in order to facilitate comparison with other studies, though we have verified that the results presented here are insensitive to separation of the anomaly fields into symmetric and antisymmetric components.

Part I

THE OBSERVED STRUCTURE AND EVOLUTION OF THE MJO

Chapter 3

THE PLANETARY WAVE STRUCTURE OF THE MJO

3.1 Overview of the structure of the MJO

First we consider the variability associated with the MJO from a global perspective. We calculate the root-mean-squared (rms) amplitude of the respective fields averaged over the MJO cycle, which is half the square root of the sum of the squared amplitude of the anomalies in regression maps (D) based on PC1 and PC2 of $\Delta\chi$:

$$D_{rms} = 1/2\sqrt{D_1^2 + D_2^2} \tag{3.1}$$

The top panel of Fig. 3.1 shows the rms amplitude of the 400 hPa ω field layer superimposed upon the annual mean, climatological-mean zonal wind field averaged over the 100−300 hPa layer. The largest amplitudes are observed over equatorial Indo-Pacific warm pool region (60°E−180°, 10°N/S), but large rms values of ω can also be found over the eastern Pacific south of Central America. The tropical (< 30°N/S) regions of large rms ω are also regions in which large OLR and precipitation anomalies are observed. Patches of enhanced ω are also observed 30°− 40°N/S, in regions of strong (>30 m s^{-1}) climatological-mean westerly winds.

The rms amplitude of the Z field averaged over the 100-300 hPa layer is shown in the middle panel. Among the most prominent features in this pattern are elongated equatorially-symmetric maxima centered along 28°N and 28°S, just equatorward of the climatological mean jet streams. The subtropical features are most clearly defined over the Indo-Pacific warm pool region but are apparent at other longitudes as well. The locations of the MJO-related variance maxima and their relation to the climatological-mean flow in the middle

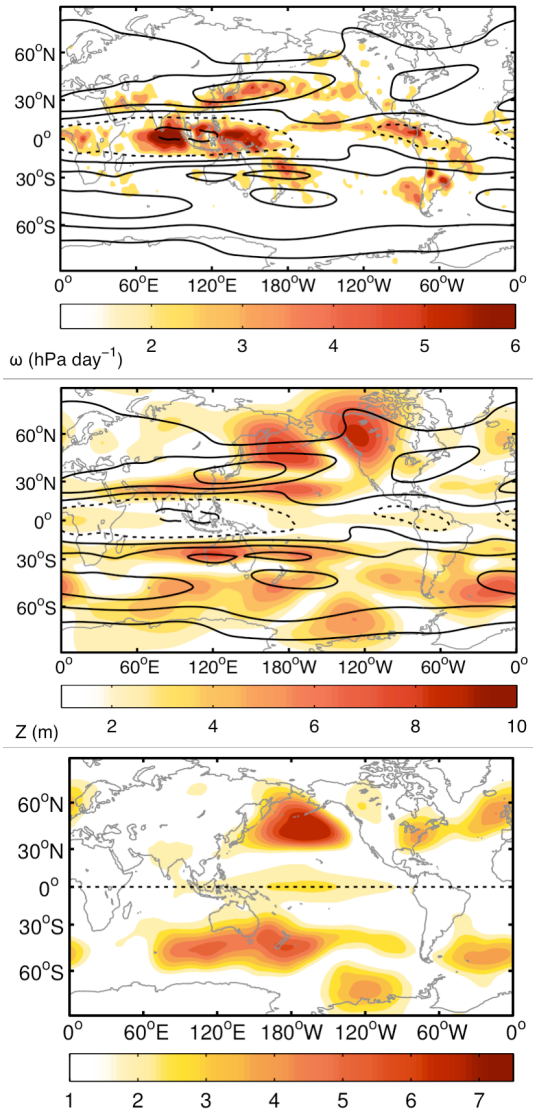

Figure 3.1: Root mean squared (rms) amplitude of 400 hPa ω (top panel), the 100-300 hPa layer-mean Z (middle) averaged over the MJO cycle superimposed upon the annual mean, climatological mean 100-300 hPa u (contours). Shading interval 1 m beginning at 2 m. Solid contours denote annual mean westerlies, dashed contours denote annual mean easterlies and the zero line is rendered as a dotted contour. Contour interval interval 10 m s^{-1}. Bottom panel: rms 500-1000 hPa layer-mean Z.

panel of Fig. 3.1 suggest the existence of upper tropospheric Rossby waveguides centered

along ∼28°N/S. Poleward of the Northern Hemisphere jet streams are a pair of equatorially-symmetric wavetrains centered over the central Pacific reminiscent of the Pacific-North American pattern (PNA, Wallace and Gutzler 1981) and the Pacific- South American Pattern (PSA, Karoly 1989; Ghil and Mo 1991; Mo and Higgins 1998). Features associated with these extratropical wavetrains can also be seen in the lower troposphere, defined here as the 500-1000 hPa layer (bottom panel). However, the flanking Rossby waves are largely absent in the lower troposphere.

Figure 3.2 shows 5-panel sequences of upper and lower tropospehric u and Z. In the upper tropospheric layer equatorially symmetric circulation couplets are centered $\sim$ 28°N/S both to the east and west of the extremum in velocity potential. These centers are responsible for the maxima in the rms Z in the middle panel of Fig. 3.1, and they correspond to the subtropical cyclonic and anticyclonic gyres pointed out by Murakami (1988); Knutson and Weickmann (1987); Rui and Wang (1990); Hendon and Salby (1994), and in subsequent studies. As suggested by Barlow (2011) and AW1, and confirmed in a modeling study by Monteiro et al. (2014), these waves owe their existence to the strong westerly winds observed in the upper troposphere associated with the climatological-mean jets located 30°N/S.

A sequence of maps for the lower troposphere (Fig. 3.2, right column), exhibits an equatorial signature to the east of the reference longitude reminiscent of an equatorial Kelvin wave. This feature corresponds to the low-level pressure signal noted by Milliff and Madden (1996), Matthews (2000) and Sperber (2003). It is wider in meridional extent than the equatorial signature in the upper tropospheric layer. To the west of the reference longitude, a pair a cyclonic centers is located near 30∘N/S, flanking a region of equatorial westerlies. These lower tropospheric Rossby waves exhibit a stronger meridional wind component along their eastern flank than the upper level flanking Rossby waves. The implications of this meridional wind component are discussed further in the following section. The pair of extratropical anticyclonic gyres located 45°N/S, to the east of the reference longitude contributes to widening the region of easterlies well beyond the equatorial belt (see also Adames et al. 2013). The pattern in the lower tropospheric Z and wind field over the warm pool is remi-

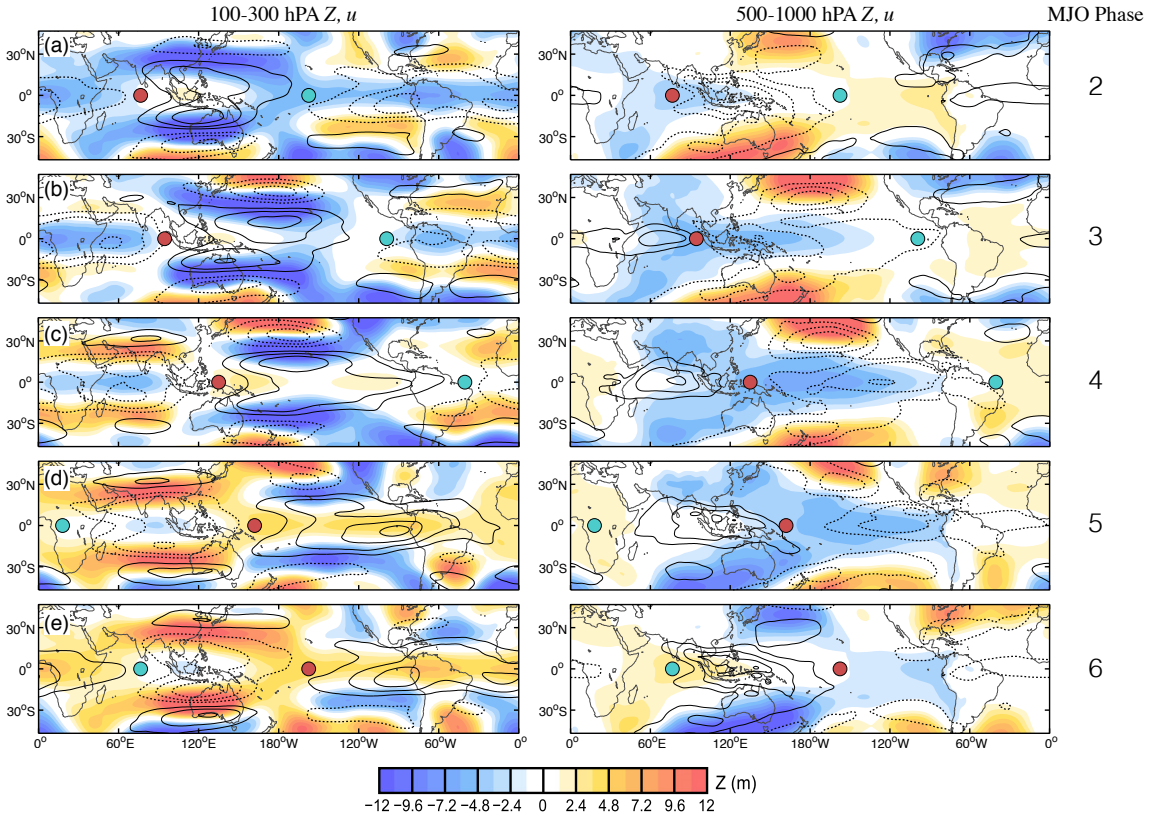

Figure 3.2: Geopotential height (Z, colored shading) and zonal wind (u) at the 100-300 hPa layer (left) and the 500-1000 hPa layer (right), regressed on linear combinations of the PC1 and PC2 of $\Delta\chi$ based on data for all 12 calendar months. (a) $-$PC2, (b) (PC1 $-$ PC2)/$\sqrt{2}$, (c) PC1, (d) (PC1 + PC2)/$\sqrt{2}$, and (e) PC2. Blue (orange) shading denotes negative (positive) Z anomalies. Solid (dashed) contours denote positive (negative) u anomalies. Contour interval is 0.5 m s^{-1} in the left column, and 0.25 m s^{-1} in the right column. The red (green) circles indicate $\Delta\chi$ maxima (minima). The approximate MJO phases in the Wheeler and Hendon (2004) MJO index are shown to the right, for reference.

niscent of the planetary wave response to an isolated, stationary heat source as described by Gill (1980).

Zonal mean rms amplitudes of Z, zonal mass flux ρu, and ω are shown in Fig. 3.3. As in Fig. 3.1 Flanking Rossby waves are evident in both hemispheres along 28°N/S equatorward of the cores of the climatological mean westerly jets. The signature of the flanking Rossby

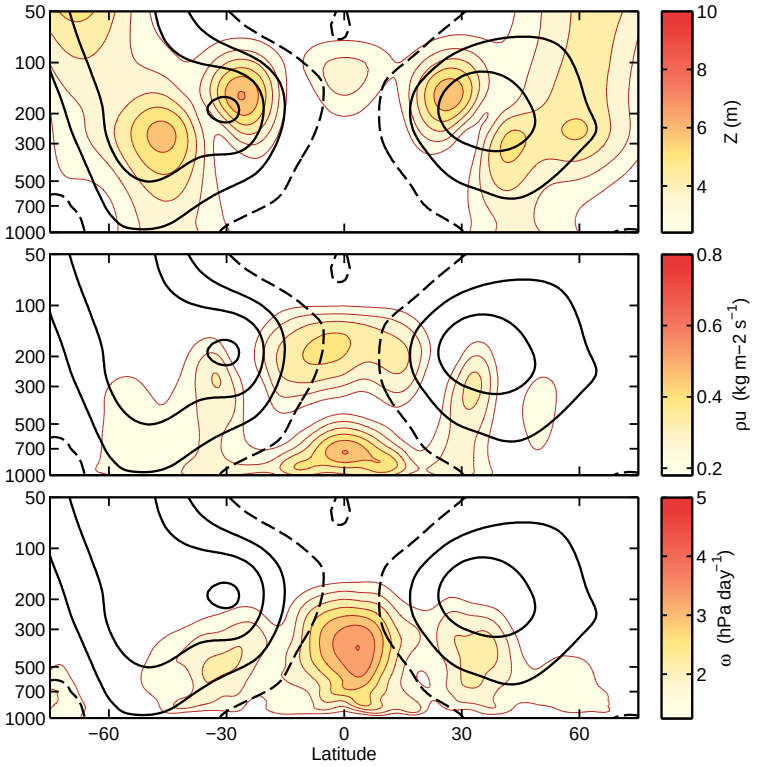

Figure 3.3: RMS amplitude of MJO-related anomalies obtained from the regression patterns based on PC1 and PC2 of $\Delta\chi$, overlain by the climatological-mean zonal wind field for each season (contoured). The shaded fields are: (top) geopotential height Z, (middle) zonal mass flux (ρu), and (bottom) vertical velocity ω. Contour interval 10 m s^{-1}.

waves in the upper tropospheric zonal mass flux and vertical velocity fields (Fig. 3.3*b*,*c*) are alsod observed on the vicinity of the maximum in the jet streams. It was shown by Barlow et al. (2005); Hoell et al. (2012) that the regions of ascent associated with the flanking Rossby waves are induced by the advection of temperature anomalies in the flanking Rossby waves by the zonal mean wind, both of which tend to be stronger in the winter hemisphere.

3.2 Temperature, vertical velocity and divergence

From here onward, all the figures presented in this chapter are "warm pool composites" as described in Chapter 2, and in Fig. 2.2. Each regression map is then zonally shifted such that

its "reference longitude" (0°) corresponds to the longitude at which $\Delta\chi$ is a maximum. These shifted maps are then composited, yielding a single map that describes the mean structure of MJO-related features relative to the reference longitude as they propagate eastward from 60°E to the Date Line. For reference, a warm pool composite of the u and Z fields shown in Fig. 3.2 is shown in Fig. 3.4.

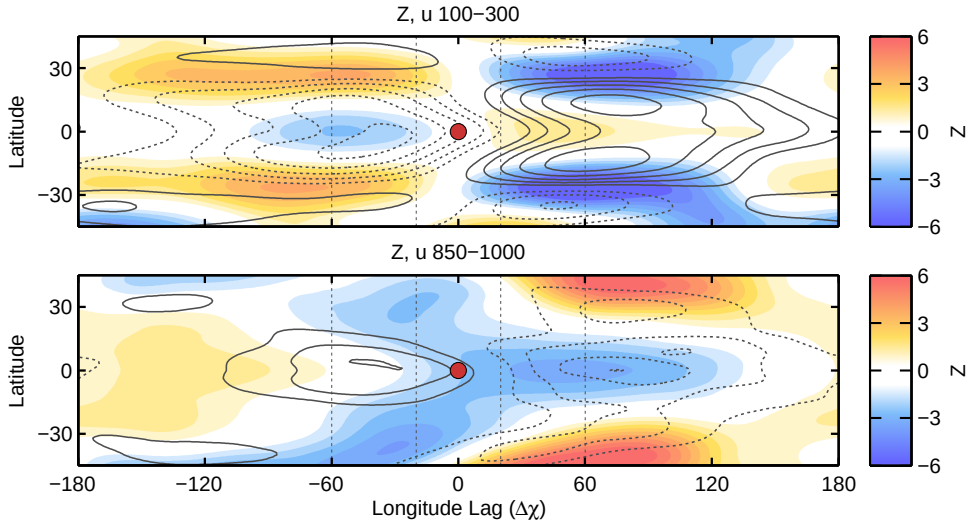

Figure 3.4: Warm pool composite of upper (top) and lower tropospheric (bottom) Z (shaded) and u (contoured). Contour interval 0.2 m s^{-1} The region where $\Delta\chi$ is a maximum is depicted as a red circle. Vertical dashed lines are placed 20 and 60 degrees to the east and to the west of the reference longitude.

In this section we discuss the structure of T, ω and Div in the MJO. Figure 3.10 shows longitude-height cross-sections of T (contoured), the mass circulation ($\rho u, \rho w$. arrows). and the mass divergence (Div, shading), averaged over the equatorial belt 10∘S to 10∘N, composited over the warm pool region. The middle and bottom panels are as in the top panel but showing the zonal ($\rho\partial u/\partial x$, middle) and meridional ($\rho\partial v/\partial y$, bottom) contributions to the mass divergence field. Over the pool region the MJO-related T anomalies are strongest $\sim 30\circ$ to the east of the reference longitude at the 250 hPa level, and exhibit significant eastward tilt with height above that level, and westward tilt with height below it. This warm region

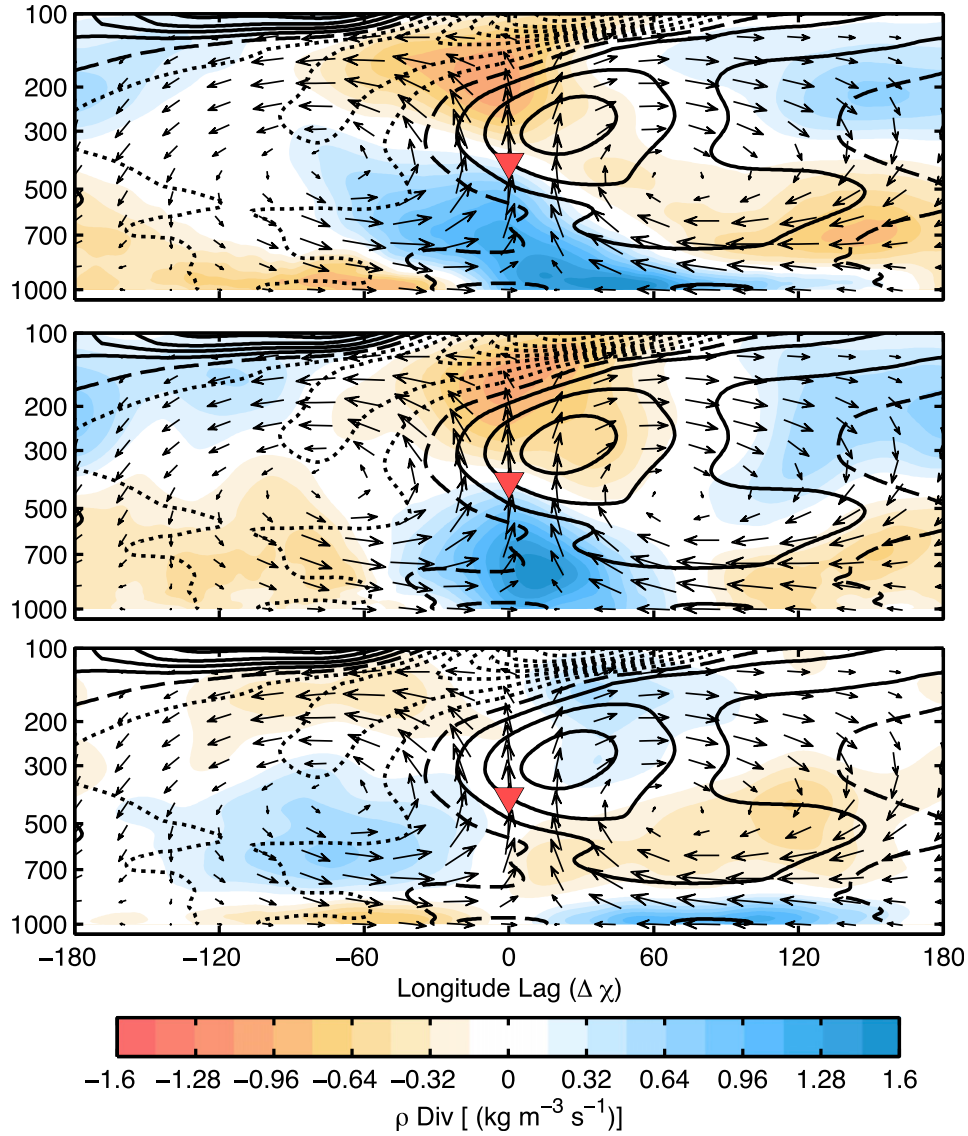

Figure 3.5: Warm pool composite equatorial (10°S-10°N) vertical cross sections of temperature (contours) and (top) mass divergence ρDiv, (middle) $\rho \partial u/\partial x$, and (bottom) $\rho \partial v/\partial y$. Vectors depict zonal equatorial mass circulation $(\rho u, \rho w)$. Contour interval is 0.05°C. The red triangle indicates the maximum in $\Delta\chi$. The ρw component has been multiplied by a factor of 250. The largest zonal flux vector is ~ 0.6 kg m^{2}s^{-1}, and the largest vertical flux vector is $\sim 7 \times 10^{-4}$ kg m^{2}s^{-1}. The zero value of T is depicted as a dashed contour. The sign of Div has been reversed for presentation.

extends up to 150∘ to the east of the reference longitude and exhibits a structure similar to that in an equatorial Kelvin wave (see Kiladis et al. 2009 for a review on this topic). This region is also characterized by boundary layer (1000-850 hPa) convergence capped by divergence in the lower-free troposphere, implying the existence of shallow convection. This layer of ascent deepens quickly as one approaches the reference longitude. To the west of the reference longitude, ascent becomes more elevated with weak downward motion underneath it, implying the prevalence of elevated stratiform ascent.

When inspecting the individual contribution to the divergence field, it is clear that $\rho\partial u/\partial x$ is dominant near the reference longitude but elsewhere $\rho\partial v/\partial y$ plays an equally important role in shaping the divergence field. The $\rho\partial u/\partial x$ field exhibits a single node near the 400 hPa level with convergence throughout the lower troposphere centered at 800 hPa. In contrast, $\rho\partial v/\partial y$ exhibits a more complex vertical structure with two nodes, one at the top of the boundary layer near 850 hPa and a second in the mid-troposphere. The vertical structure of in $\rho\partial v/\partial y$ is suggestive of an important contribution from friction in the boundary layer. Neither $\rho\partial u/\partial x$ nor $\rho\partial v/\partial y$ exhibits a vertical tilt but they are zonally shifted with respect to one another such that the total divergence field exhibits a substantial vertical tilt. We can therefore interpret the large-scale circulation of the MJO as the superposition of a deep overturning circulation ($\rho\partial u/\partial x$) in the zonal plane and shallow, equatorially symmetric meridional circulation ($\rho\partial v/\partial y$) that is at least partially driven by friction.

To further elucidate the structure of temperature and vertical velocity, Figure 3.6 shows warm pool composites of of u, v, ω, and T, partially zonally averaged 20°?60° to the east and 20°?60° to the west of the longitude where $\Delta\chi$ is a maximum. The cross sections are analogous to those in Fig. 3.6 but show the zonal mass flux (ρu) as contours and the meridional mass circulation (ρv, ρw) as vectors. To the east of the $\Delta\chi$ maximum (right panel), broad, equatorially centered ρu anomalies centered around 700 and 150 hPa are associated with the baroclinic modal structure described in Adames and Wallace (2014a).

In the lower troposphere the westerlies to the west of the heat source (i.e., the $\Delta\chi$ maximum) shown in the left panel of Fig. 3.6 are stronger and more narrowly focused on

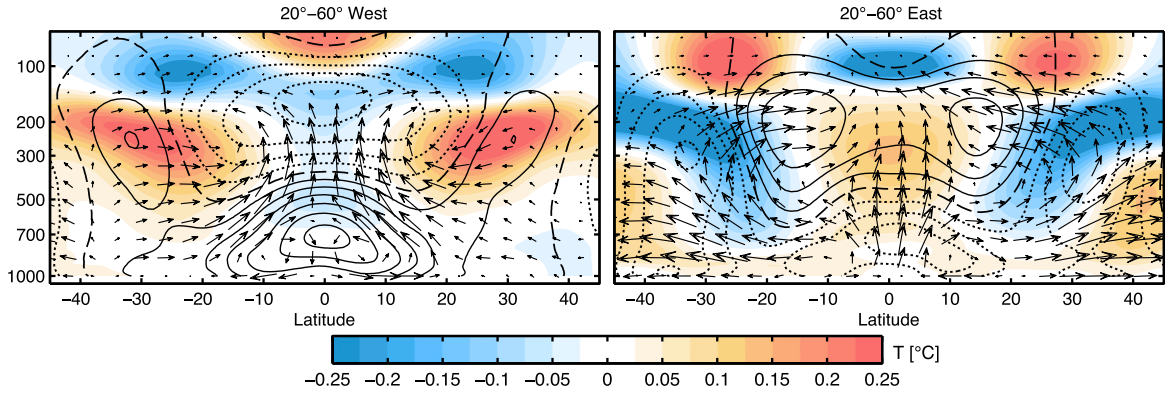

Figure 3.6: Warm pool composite latitude-height cross sections of temperature (shading), zonal mass flux (ρu, contours), and meridional mass circulation ($\rho v, \rho w$) represented as vectors, partially zonally averaged from 20° to 60° to the (left) west and (right) east of the longitude at which $\Delta\chi$ is a maximum. Contour interval is 0.1 kg m^2 s^{-1}. The ρw component has been multiplied by 250 to make it consistent with the aspect ratio of the plot. The largest meridional flux vector is ~ 0.1 kg m^2 s^{-1} and the largest vertical flux vector $\sim 4 \times 10^{-4}$ kg m^2 s^{-1}. The zero value of ρu is depicted as a dashed contour.

the equator than the easterlies to the east of it. Consistent with the thermal wind equation, the corresponding temperature anomalies, warm to the east of the heat source and cold to the west, are centered in the layer of strongest vertical wind shear near the midtropospheric node in u. The vertical velocities are upward in the equatorial belt in both sections, but the centroid of the ascent is more elevated to the west of the heat source than to the east of it. This distinction is consistent with the bottom-up development of the region of ascent in Fig. 3.10. Equatorially symmetric, lower-tropospheric meridional flows are clearly evident in both sections: equatorial outflow to the east of the heat source and inflow to the west of it. The center of mass is higher for the inflow than for the outflow. The near-surface confluent flow to the east contributes to the near-equatorial ascent while the diffluent flow to the west opposes it.

Figure 3.7 is as in Fig. 3.6, but a center panel is included to show the region within 20° of the $\Delta\chi$ maximum, and mass divergence ρDiv is shown as the shaded field. The bottom up

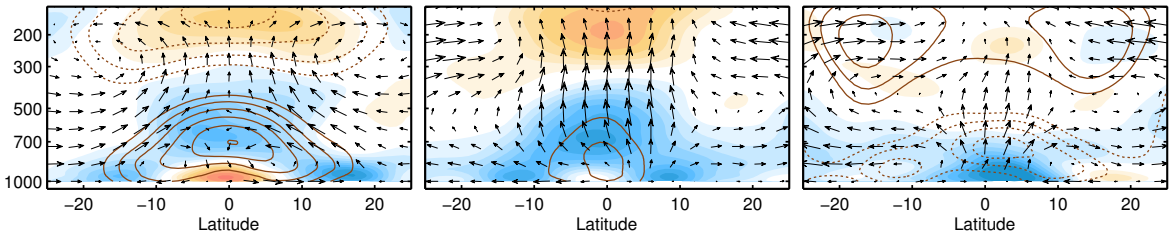

Figure 3.7: Warm pool composite latitude-height cross sections of mass divergence (ρDiv, shading), zonal mass flux (ρu, contours), and meridional mass circulation ($\rho v, \rho w$) represented as vectors, partially zonally averaged from 20° to 60° to the (left) west and (right) east of the longitude at which $\Delta\chi$ is a maximum, and within 20° of the reference longitude (center). The ρw component has been multiplied by 250 to make it consistent with the aspect ratio of the plot. The largest meridional flux vector is ~ 0.1 kg m^2 s^{-1} and the largest vertical flux vector $\sim 4 \times 10^{-4}$ kg m^2 s^{-1}. The zero value of ρu is depicted as a dashed contour.

evolution of equatorial (10°N/S) divergence seen in Fig. 3.10 is seen in this figure. However, the region of boundary layer convergence widens near the reference longitude and splits into two off equatorial regions of convergence to the west of the reference longitude. These regions of convergence appear to flank the region of equatorial westerlies, suggesting the role of Rossby waves in the observed motion.

We will now decompose the three-dimensional vertical velocity (ω) fields into modal structures with orthogonal vertical profiles through the use of EOF. The analysis is carried out using all grid points within the equatorial band 10°S-10°N. The leading mode of the vertical motion field, ω_1, which accounts for 72% of its variance is indicated by the solid line in Fig. 3.8. It is of the same polarity at all levels and exhibits a maximum near 400 hPa. The second mode, ω_2, which accounts for another 18% of the variance, is characterized by perturbations of opposing polarity above and below 600 hPa, attaining its largest amplitudes near 850 and 300 hPa. The vertical profiles of ω_1 and ω_2 are analogous to linear combinations of the "deep convective" and "elevated stratiform" categories used by Houze (1982, 1989); Schumacher et al. (2004); Haertel et al. (2008), among others to characterize latent heating

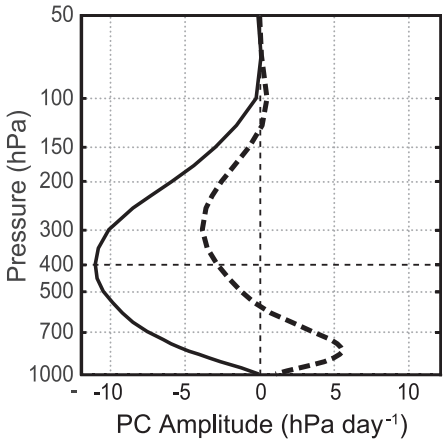

Figure 3.8: Leading principal components (PCs) of ω derived from EOF analysis of the vertical profiles of ω regressed on PC1 and PC2 of $\Delta\chi$ as explained in the text. The analysis is based on grid points in the 10°S−10°N latitude belt. The solid line denotes the first mode and the dashed line denotes the second mode. The PCs are scaled in proportion to their eigenvalues and expressed in units of hPa day^{-1}. By convention, negative values of ω_1 and ω_2 are indicative of ascent. The dimensional values are representative of amplitudes of the respective PC time series.

profiles in tropical convective systems.

Warm pool composites of the horizontal maps associated with the modal structures in Fig. 3.8 are shown in Fig. 3.9, alongiside the MJO-related OLR anomalies (top panel). The negative ω_1 anomalies, shown in the middle panel, exhibit a structure to the OLR anomalies shown in the top panel but the east-west asymmetries in the shape of the area of enhanced ascent are more pronounced. To the east of the reference longitude anomalous ascent (negative ω_1) is bowed forward along the equator, and it widens and splits into two off-equatorial lines of anomalous ascent to the west of the reference longitude with edges near 18°N/S. This structure is reminiscent of the "swallowtail pattern" described by Zhang and Ling (2012).

Regions of anomalous ascent are also observed poleward and to the west of the flanking Rossby cyclones. No OLR anomalies are seen accompanying these regions of ascent

since cooling associated with adiabatic lifting is approximately being balanced by anomalous horizontal temperature advection Barlow et al. (2005); Hoell et al. (2012).

The pattern for ω_2 is much more equatorially focused. It is positively correlated with the patterm in the lower tropospheric winds. While the horizontal pattern in ω_1 bears a stronger resemblance to the OLR anomaly field, areas of widespread stratiform clouds associated with the negative ω_2 anomalies to the west of the reference longitude are likely responsible for the OLR anomalies observed in this region. Regions of stronger anomalous ascent (ω_1) flank this

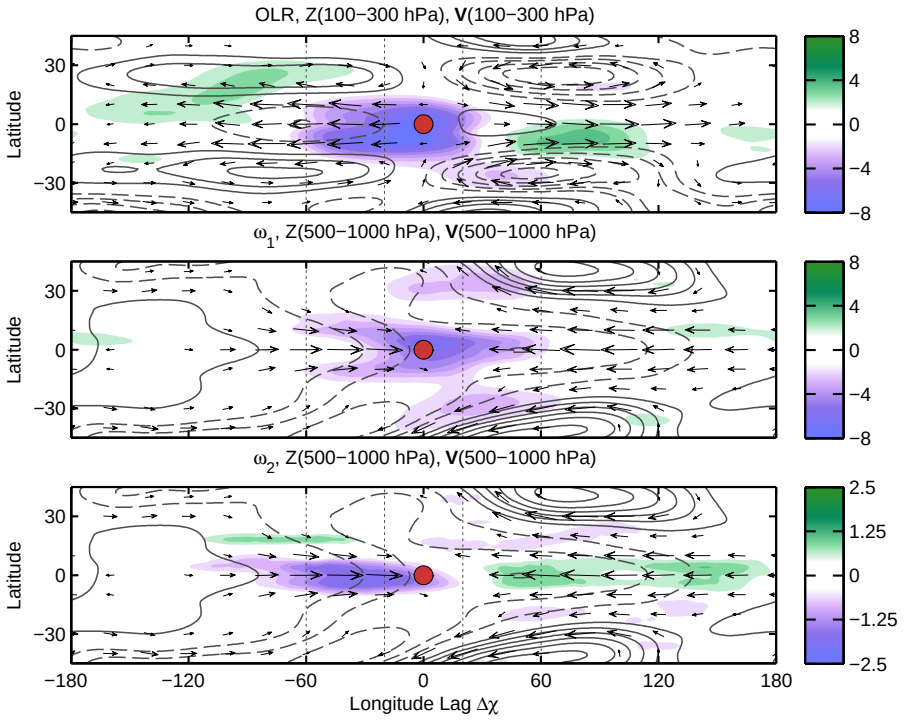

Figure 3.9: (Top) Warm pool composite WPC1 of OLR (shaded) and 100-300 hPa averaged Z (contours) and horizontal winds (arrows). Contour interval 1.5 m. Only arrows corresponding to wind anomalies that are found to be statistically significant at the 95% confidence interval are shown. The largest wind vector is ∼2 m s^{-1}. (middle and bottom) Warm pool composite of 500-1000-hPa layer-averaged winds (vectors), Z (contours), ω_1 (shading in middle panel), and ω_2 (shading in lower panel). Contour interval is 1 m. The ω_1 and ω_2 are scaled to the 300-hPa level. The largest wind vector is ∼0.75 m s^{-1}. The red circle indicates the maximum in $\Delta\chi$.

region of equatorial elevated stratiform convection to the west of the reference longitude.

When considered in combination, the patterns in ω_1 and ω_2 are indicative of a "bottom up" evolution: with convection beginning shallow and capped by anomalous descent, but becoming deeper and evolving into stratiform convection with elevated bases.

3.3 Relationship between vertical velocity and lower-tropospheric divergence

We will now consider the structure of the lower-tropospheric divergence field and how it relates to the ω_1 and ω_2 modes described in the previous section. Figure 3.10 shows the structure of Div, $\mathbf{V}$ and Z within the boundary layer (BL, the 850-1000 hPa layer) and the lower free troposphere (FT, the 500-850 hPa layer). The FT pattern (top panel) resembles the response to a stationary equatorial heat source described by Matsuno (1966) and Gill (1980), with divergence concentrated over the equatorial belt over the region of strongest diabatic heating. It is different from the Matsuno / Gill solution in the sense that the contribution of the Rossby waves to the west of the heating is not as well defined and the Z anomalies extend well beyond the equatorial belt. The FT near-equatorial winds exhibit a clearly discernible meridional component, with diffluence to the east of the reference longitude and confluence to the west. It is worth noting that Div_{FT} exhibits a structure similar to the OLR field seen in the top panel of Fig. 3.9.

The structure of the divergence field in the BL (Div_{BL}) is different from that of Div_{FT}. The maximum in convergence is shifted $\sim$35$\circ$ of longitude to the east of the strongest FT convergence, as noted by Hendon and Salby (1994); Maloney and Hartmann (1998). The wind field in this layer exhibits a meridional component that is of opposing sign to that in the FT. To the west of the region of maximum large-scale convergence is a region of equatorial BL divergence flanked by lines of off-equatorial convergence ($\sim$18°N/S).

The structure of the DivBL can be represented in terms of the Laplacian of the BL geopotential field ($\phi = gZ$), augmented the divergence of the Coriolis parameter [i.e.$\nabla \cdot$

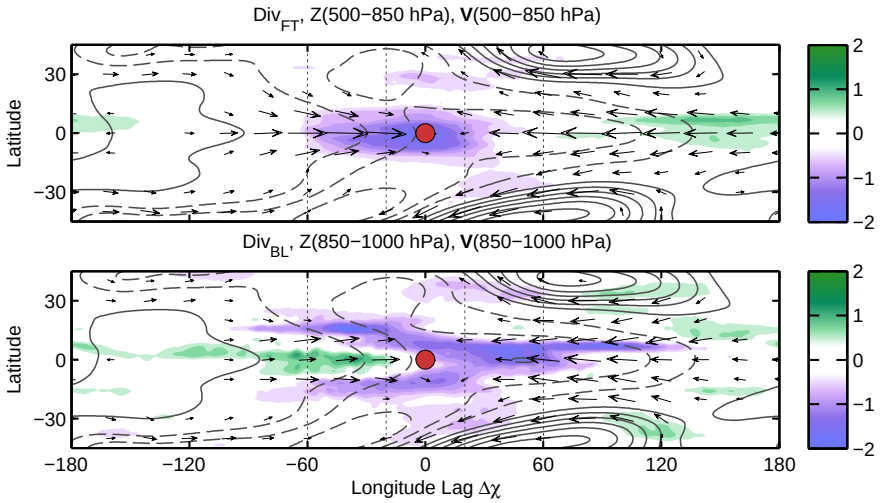

Figure 3.10: Warm pool composite of: (a) lower free-tropospheric (FT, 500−850 hPa averaged) divergence (shaded), Z and horizontal wind anomalies (arrows). (b) As in the top panels but averaged over the boundary layer (BL, 850−1000 hPa). Only arrows corresponding to wind anomalies that are found to be statistically significant at the 95% confidence interval are shown. The largest wind vector is ∼0.75 m s^{-1}.

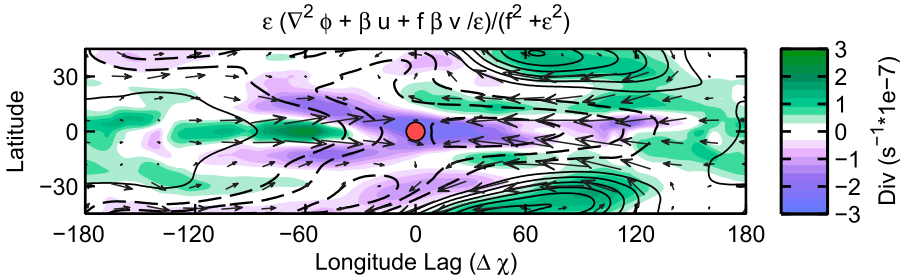

Figure 3.11: Estimate of BL divergence based on Eq. (3.2). The shading depicts Div_{BL} calculated applying Eq. (3.2) to the observed BL (850-1000-hPa layer averaged) Z, u, and v fields. Contour interval is 1 m. The largest wind vector is ∼0.75 m s^{-1}. The red circle indicates the maximum in $\Delta\chi$.

$(fk \times u)$, see Eq. 6.2a of Wang and Li 1994]:

$$Div_{BL} \approx \frac{-\varepsilon}{\varepsilon^2 + \beta^2 y^2} \left(\nabla^2 \phi + \beta u + f \beta^2 v \varepsilon^{-1} \right) \tag{3.2}$$

where $\varepsilon = 2.6$ day^{-1} is the Raleigh friction coefficient, chosen to be consistent with results of studies by Deser (1993); Li and Wang (1994); Stevens et al. (2002), and $\beta = 2.28 \times 10^{-11}$ m^{-1} s^{-1} is the beta parameter ($\beta = df/dy$). A warm pool composite of the estimated divergence field is shown in Fig. 3.11. That the estimated divergence field based on the previous equation closely matches the structure of the observed Div_{BL} field suggests that it is driven by planetary-scale wave motions in the presence of BL friction. It is possible to represent the modal structures of ω in terms of linear combinations of BL and FT Div through the continuity equation. The deep convective profile, ω_1 can be represented as the sum of the divergence in the two layers. In the case of ω_2, descent should peak near 850 hPa and weaken above it. Expressions for ω_1 and ω_2 take the form:

$$\omega_1 \propto Div_{BL} + Div_{FT} \tag{3.3a}$$

$$\omega_2 \propto Div_{BL} - Div_{FT} \tag{3.3b}$$

The correspondence is nearly perfect, as seen in Fig. 3.12. This result implies that the different profiles in divergence in the BL and FT conspire to create the observed vertical velocity fields, its westward tilt with height and its characteristic swallowtail shape (as seen in Fig. 3.9). As it will be seen in the next Chapter, these superposition of BL and FT convergence also shapes the observed structure of moisture and precipitation.

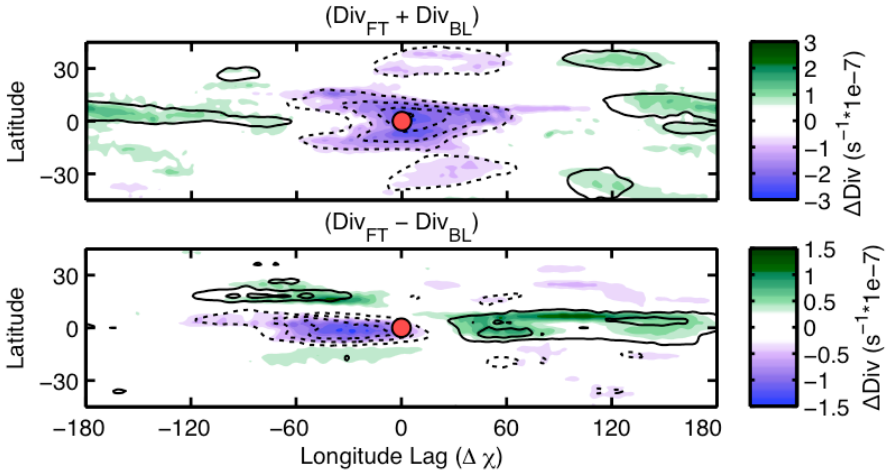

Figure 3.12: Warm pool composite of ω_1 scaled to the 300-hPa level (contours) and the sum of FT and BL divergence. Contour interval is 1.5 hPa day^{-1}. (bottom) Warm pool composite of ω_2 scaled to the 300-hPa level (contours) and the difference between FT and BL divergence Contour interval is 0.5 hPa day^{-1}. The red circle indicates the maximum in $\Delta\chi$.

Chapter 4

THE MJO-RELATED STRUCTURE AND EVOLUTION OF MOISTURE

4.1 Vertical velocity, moisture and precipitation in the MJO warm pool composite

We first examine the spatial relationship between deep tropospheric ascent, as defined by negative anomalies in ω_1, and anomalies in moisture and precipitation. The top three panels of Fig. 4.1 show a warm pool composite (hereafter referred to simply as "composite") of TRMM-3B42 rainfall (P_{TRMM}), ERA-Interim precipitation (P_{ERA-I}) and ERA-Interim column-integrated water vapor ($\langle q \rangle = g^{-1} \int_{100hPa}^{1000hPa} q dp$) as contoured fields, superimposed upon the field of ω_1 (colored shading). All the fields exhibit the characteristic "swallowtail" shape pointed out by Zhang and Ling (2012) and extensively analyzed in AW2. However, the TRMM precipitation anomalies are larger in amplitude than the ERA-Interim anomalies by about a factor of two and shifted slightly to the west of them. Both TRMM and ERA-Interim precipitation exhibit an extratropical quadrupole pattern with centers ∼35°N/S in which precipitation is enhanced ∼30° to the east of the reference longitude (hereafter RL) and suppressed ∼120° to the east it. These features are accompanied by vertical velocity perturbations of the corresponding sign, which are related to the regions of zonal temperature advection in the flanking Rossby waves (see Fig. 5 in AW2). The distribution of $\langle q \rangle$, shown in Fig. 4.1*c*, closely resembles the distribution of TRMM precipitation.

The $\langle q \rangle$ tendency $\partial \langle q \rangle / \partial t$, calculated by taking a two-day centered difference of $\langle q \rangle$, is shown in of Fig. 4.1*d*. It exhibits a narrow maximum north of the equator centered ∼120° to the east of the RL, which may be related to the modulation of the ITCZ by the MJO. A narrow equatorial band of drying is centered ∼20° to the west of the RL, between the wings of

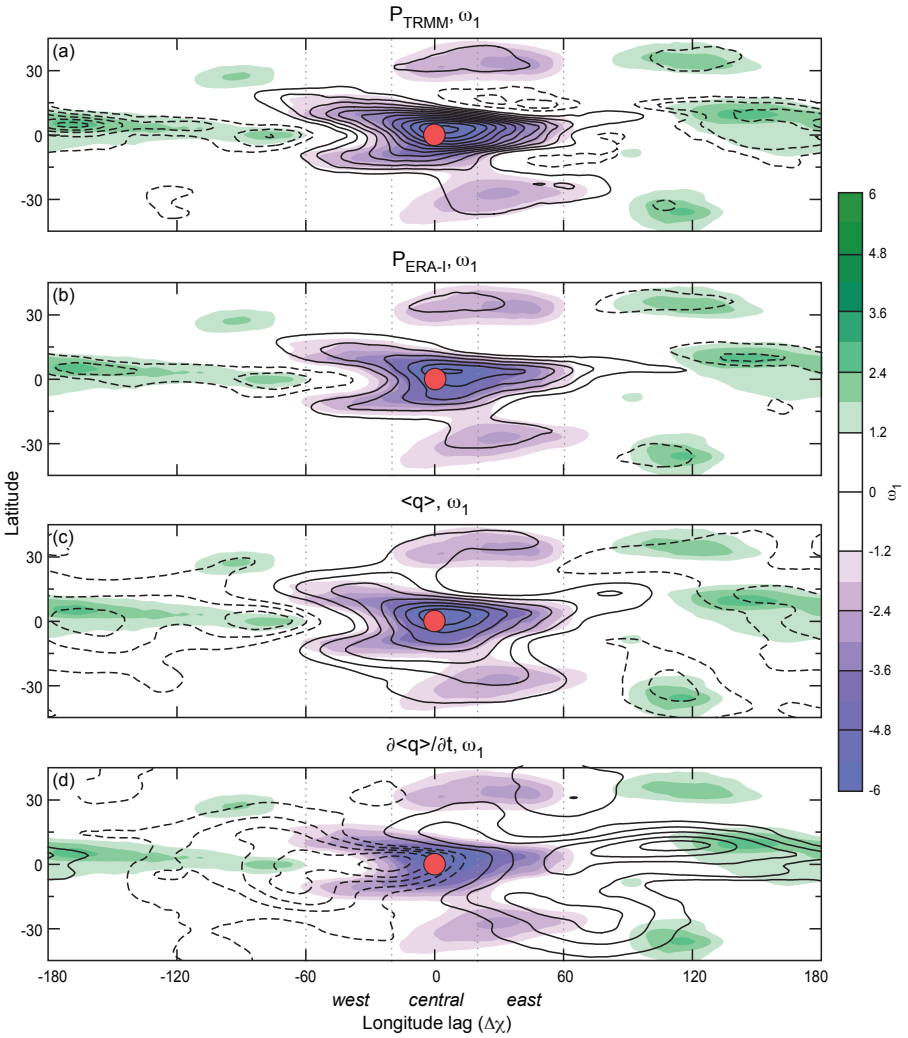

Figure 4.1: Warm pool composite showing ω_1 (colored shading), scaled to its 300 hPa value and (a) TRMM-3B42 precipitation, (b) ERA-Interim precipitation, (c) ERA-Interim column integrated water vapor $\langle q \rangle$ and (d) ERA-Interim $\langle q \rangle$ tendency $\partial \langle q \rangle / \partial t$. Warm pool composites are constructed as described in Chapter 2. Contour interval 0.1 mm day^{-1} for precipitation, 0.125 kg m^{-2} for $\langle q \rangle$, and 0.025 kg m^{-2} day^{-1} for $\partial \langle q \rangle / \partial t$.

the swallowtail pattern in vertical velocity and precipitation. The bands of enhanced rainfall and ascent in the tail itself correspond to the bands of strong cyclonic wind shear along the axes of the lower-tropospheric Rossby wave couplet. The two off-equatorial maxima in

$\partial\langle q\rangle/\partial t$ along 30°N/S, 60° to the east of the RL likely correspond to moistening in advance of the region of the enhanced rainfall to the west of the troughs in the upper-level flanking Rossby waves.

To document the vertical structure of moisture over the equatorial belt, Fig. 4.2*a* shows longitude-height cross sections of q (contoured) overlain by the mass circulation $(\rho u, \rho w)$ in the equatorial plane. Positive moisture anomalies extend as far as 130° to the east of the RL. These anomalies are confined to the 700−1000 hPa layer at the eastern end of the section, but become progressively deeper and stronger as one approaches RL in the rising branch of the zonal overturning circulation. The strongest positive q anomalies occur ∼10° to the east of the RL at the 700 hPa level, above the leading edge the advancing westerly wind anomalies. Progressing farther toward the west, the moisture anomalies rapidly weaken and become more elevated.

Figure 4.2*b* shows zonal profiles of anomalies in $\langle q\rangle$, $-\omega_1$, ω_2 and $\partial\langle q\rangle/\partial t$. The $\langle q\rangle$ and $-\omega_1$ profiles are similar, with maxima a few degrees to the east of the RL. A strong correspondence between the profiles of ω_2 and $\partial\langle q\rangle/\partial t$ is evident, with shallow ascent (positive ω_2) associated with moistening and stratiform ascent (negative ω_2) associated with drying. It was shown in AW2 that ω_2 anomalies are related to shallow, frictionally driven meridional circulation cells observed in association with the lower tropospheric zonal wind anomalies in equatorial Kelvin and Rossby waves forced by an equatorial heat source. Figure 4.2*c* will be described in a later section.

In order to examine changes in moisture in the mid to upper troposphere, we divide the specific moisture anomaly q by $\bar{q}_s$, the value of the mean saturation specific humidity at that level, to obtain the relative humidity anomaly RH. $\bar{q}_s$ is calculated using the relation $\bar{q}_s \approx 0.622 \times [e_s/(p - 0.378e_s)]$, where the saturation vapor pressure e_s is obtained using the Clausius-Clapeyron equation (see Eq. 3.97 of Wallace and Hobbs 2006), and both p and e_s are in units of hPa. Composite RH is shown as the shaded field in Fig. 4.2*a* and Fig. 4.3*a*, along with the specific humidity and $-\omega$ anomalies, respectively. The ω and RH profiles are similar, but the maximum value in RH is located slightly to the west of the

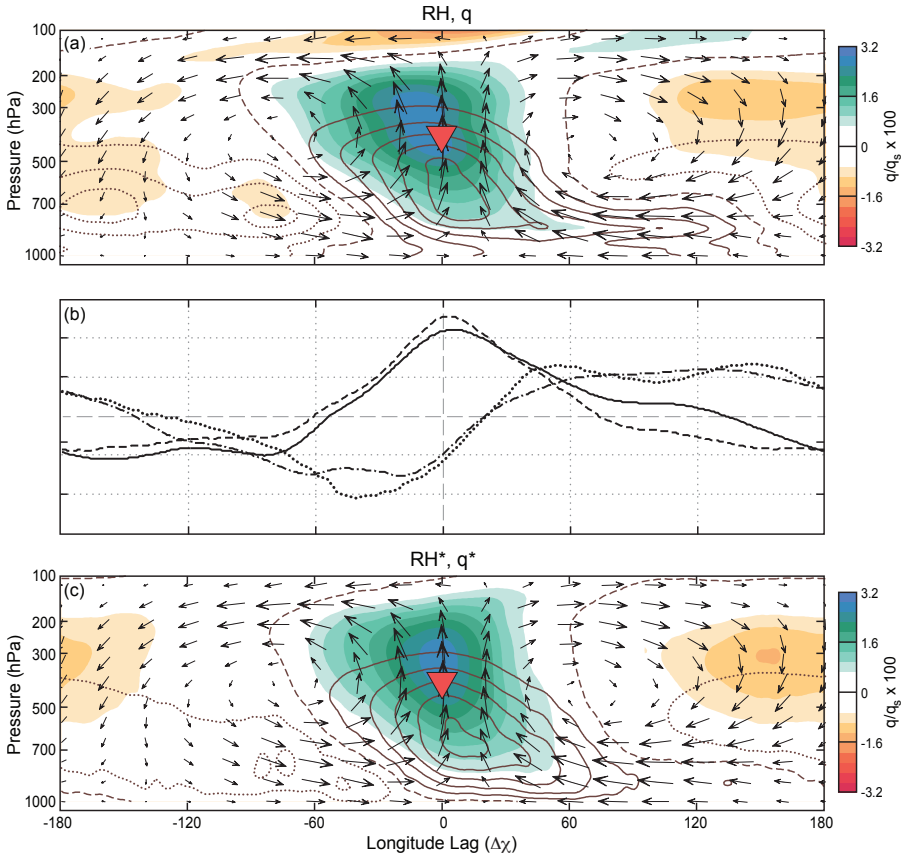

Figure 4.2: (a) Composite longitude-height cross sections of zonal mass circulation (arrows), relative humidity anomalies (RH, shaded) and q (contoured). Contour interval 0.025 g kg^{-1}. The largest meridional flux vector is ∼0.1 kg m^{-2} s^{-1}, and the largest vertical flux vector ∼4 × 10^{-4} kg m^{-2} s^{-1}. The zero contour of q is depicted as dashed. (b) $\langle q \rangle$, (black solid), $\partial \langle q \rangle / \partial t$ (gray solid), $-\omega_1$ (dashed) and ω_2 (dotted), all arbitrarily scaled to facilitate comparison. (c) As in the top panel but q^* and RH^* derived diagnostically from the vertical velocity field using Eq. (4.5). All fields are averaged from 10°S−10°N.

region of maximum ascent. The distinction is more clearly revealed by the line plots shown in Fig. 4.3b. These line plots also show that the RH anomalies are closely aligned with OLR anomalies. Thus, large values of vertically-integrated RH are associated with regions of widespread upper-level clouds, in agreement with observational studies of Powell and Houze (2013), and Xu and Rutledge (2014). Both q and RH (Fig. 4.2a) exhibit a "bottom-up"

development as one moves from east to west, in the same sense that the vertical velocity anomalies do.

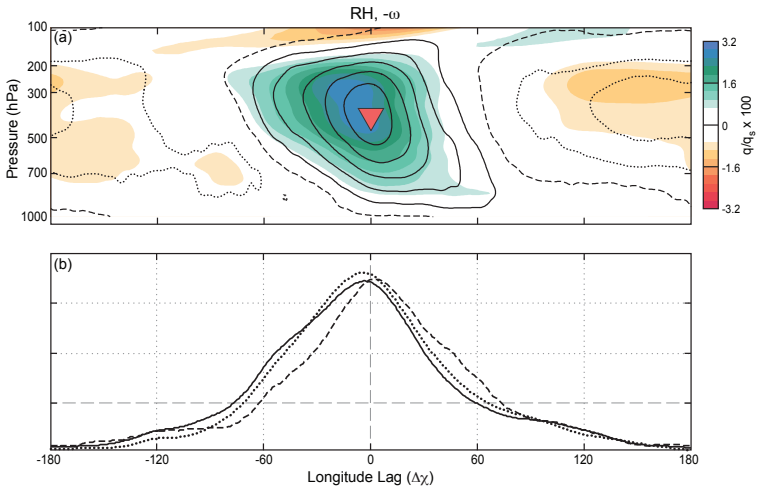

Figure 4.3: (a) Composite longitude-height cross section of RH (shaded) and $-\omega$ (contoured). Contour interval 1 hPa day^{-1}. (b) OLR (black solid), $-\omega_1$ (dashed) and $\langle RH \rangle$ (dotted), scaled arbitrarily to facilitate comparison. All fields are averaged from 10°S−10°N.

The results presented in this section are indicative of a strong relationship between the moisture and vertical velocity fields in this warm pool composite framework. There is also an indication that the processes that lead to a systematic bottom-up evolution in ω are also responsible for the moistening to the east of the RL and drying to the west of it.

4.2 Analysis of the ERA-Interim moisture budget

In this section we perform a comprehensive analysis of the three-dimensional moisture budget, using the warm pool composites shown in Chapter 4.1 in order to obtain a more detailed description of the processes that produce the systematic moistening to the east of the region of maximum ascent and the drying to the west of it. The MJO-related local time rate of

change of specific humidity $\partial q/\partial t$ is given by

$$\frac{\partial q}{\partial t} = -\mathbf{V} \cdot \nabla q - \omega \frac{\partial q}{\partial p} - \frac{Q_2}{L_v} \tag{4.1}$$

where the terms on the right-hand-side are the horizontal moisture advection, the vertical moisture advection and the apparent moisture source and sink Q_2 as defined in Yanai et al. (1973), which represents the combined effects of evaporation and condensation and the flux of moisture by unresolved eddies (Yanai and Johnson 1993). Because the ERA-Interim dataset does not have an explicit representation of Q_2, we obtain it as a residual from the sum of the other terms. By defining Q_2 in this way we are including the so-called "residual" term in the moisture budget that is included among the reanalysis products, which represents a missing moisture source or an excessive moisture sink (Kiranmayi and Maloney, 2011; Mapes and Bacmeister, 2012). We have verified the existence of this residual in our study by analyzing the vertically-integrated moisture budget (Eq. 2 in Kiranmayi and Maloney 2011) and, while it complicates the interpretation of the results presented, it does not affect the main findings discussed from here on. We believe that this residual is the result of an inadequate treatment of precipitation in the reanalysis because including it as part of the vertically-integrated Q_2 anomalies yields a spatial structure that agrees more closely with the TRMM-3B42 precipitation anomalies, as discussed later in this section. The evaporation anomalies, on the other hand, contribute little to the observed structure of Q_2 within 60° of the reference longitude (not shown).

4.2.1 Composite longitude-height cross sections

It has been shown in previous studies (López Carrillo and Raymond 2005; Kiranmayi and Maloney 2011; Hsu and Li 2012; DeMott et al. 2014; among others) that vertical advection and Q_2 are the dominant terms in Eq. (4.1), and that they largely cancel one another. Panels (*a*) and (*b*) of Fig. 4.4 show equatorial (10°S−10°N) longitude-height cross sections of these two terms overlain by ω anomaly contours. The two fields exhibit a bottom-up

development from east to west, analogous to the ω anomalies, with the strongest anomalies colocated with the largest ω anomalies near the RL. The strongest anomalies in these terms are slightly shifted to the east of the peak RH anomalies near the 400 hPa level in Fig. 4.3a.

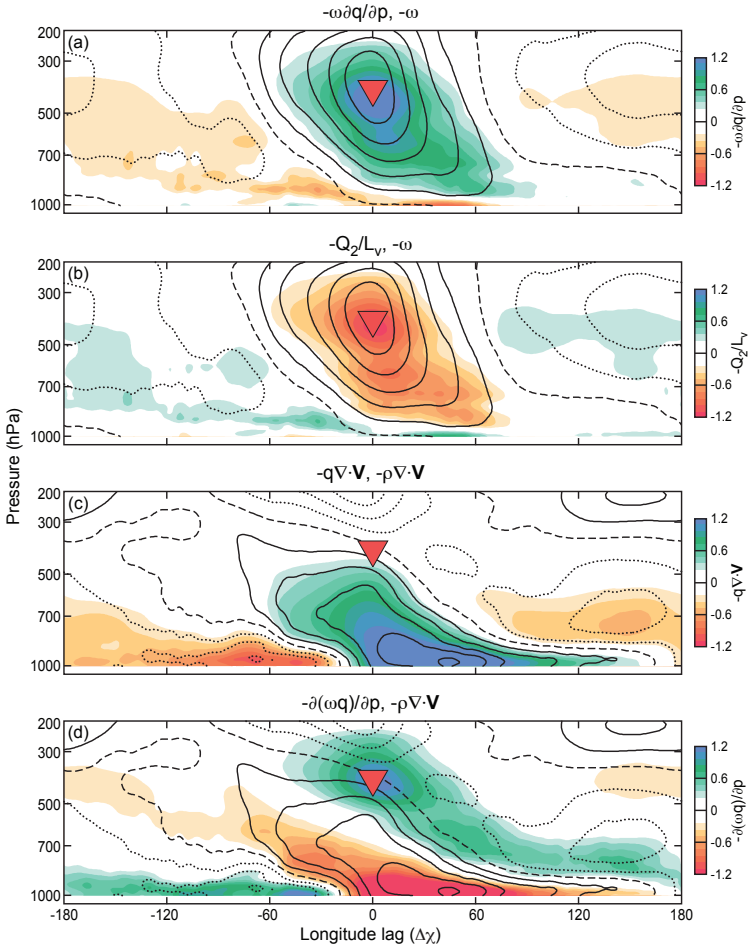

Figure 4.4: Composite longitude-height cross sections of $-\omega$ (contoured in panels a and b), mass convergence (contoured in panels c and d) and the terms in the moisture budget: (a) vertical moisture advection, (b) apparent moisture sink Q_2, (c) horizontal moisture convergence and (d) convergence of the vertical moisture flux. Contour interval 1 hPa day^{-1} for $-\omega$ and 3 $\times$ 10^{-8} kg m^{-2} s^{-1} for $-\rho Div$. Shading in units of 10^{-1} g kg^{-1} day^{-1}.

The strong correspondence between vertical moisture advection and Q_2 indicates that condensation in regions of ascent, due to the convective parameterization schemes and the

linearized large-scale condensation in ERA-Interim is the largest contributor to Q_2. We refer the reader to Bechtold et al. (2004); Dee et al. (2011), and Zhu and Hendon (2015) for further documentation and interpretations on convection in model analysis and their contribution to Q_2.

The vertical moisture advection term can be further broken down into a vertical moisture flux convergence term and a horizontal moisture convergence term:

$$\omega \frac{\partial q}{\partial p} = \frac{\partial(\omega q)}{\partial p} + q \nabla \cdot \mathbf{V} \tag{4.2}$$

Longitude-height composites of these two terms along with contours depicting horizontal mass convergence are shown in panels (c) and (d) of Fig. 4.4. That the composite horizontal moisture convergence field is nearly identical to the overlain mass divergence field indicates that the variability in horizontal moisture convergence is dominated by the variability in horizontal mass convergence, consistent with results of Hsu and Li (2012). To first order, the horizontal moisture convergence (panel c) moistens the region of the wave near the RL where ω_1 is strongest, and the convergence of the vertical flux of moisture (panel d) reflects the transport of moisture upward into the mid-troposphere.

Because Q_2 and vertical moisture advection exhibit nearly canceling patterns, it is instructive to consider the net effect of these two terms, shown in Fig. 4.5a. Note that the scale on the color bars is 1/3 of that in the previous figure. Moistening due to the net effect of these two terms (green shading Fig. 5.5a) occurs in the BL to the east of the RL and in the mid-troposphere in the vicinity of the RL. The contribution from horizontal moisture advection to $\partial q/\partial t$ is shown in Fig. 5.5b. Drying from horizontal moisture advection (orange shading Fig. 5.5b) is seen near and to the west of the RL from ∼850 hPa up to ∼400 hPa, co-located with the region where $\partial q/\partial t$ is a minimum. Drying by horizontal advection and the net moistening from vertical moisture advection and Q_2 approximately cancel one another in the mid-troposphere within ∼20° of the RL. Neither of the shaded fields in Fig. 5.5 exhibits any significant tilt with height, but they are shifted zonally such that when added

together they produce the westward tilt with height observed in $\partial q/\partial t$.

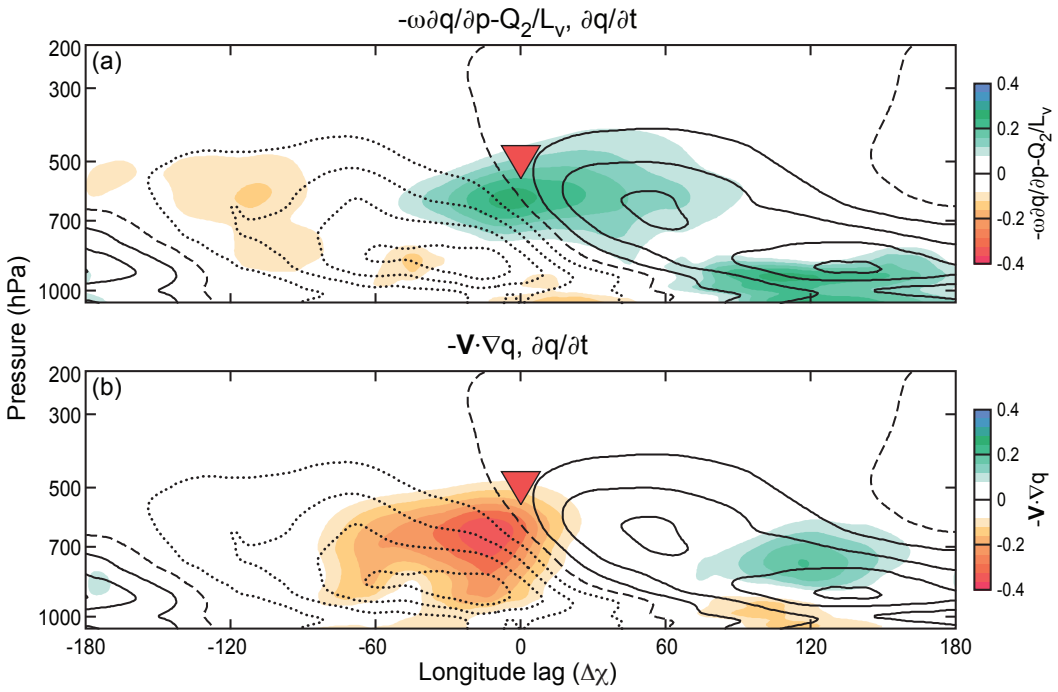

Figure 4.5: Composite longitude-height cross sections, as in the previous figure, but showing (a) the sum of vertical moisture advection and the apparent moisture sink Q_2 (shaded), and $\partial q/\partial t$ (contoured), and (b) the horizontal moisture advection (shading) and $\partial q/\partial t$(contoured). Contour interval 0.005 g kg^{-1} day^{-1}. Shading is in units of 10^{-1} g kg^{-1} day^{-1}. Superposing the shaded fields in the two panels yields the contoured field.

4.2.2 Composite latitude-height cross sections

We will now focus on the meridional structure of the MJO's moisture budget. For this purpose we subdivide the active envelope of the MJO into three subdomains with respect to the longitude of strongest ascent: the western sector (60°−20° to the west of the RL), the central sector (within 20° of the RL) and the eastern sector (20°−60° to the east of the RL) as indicated by the vertical dashed lines in Fig. 4.1. The panels in the top row of Fig. 4.6 are meridional cross sections averaged over these sectors and the panels in the bottom row

show the corresponding meridional profiles of OLR and TRMM-3B42 rainfall. The region of maximum ascent (middle column) is characterized by large values of RH, $-\omega$, and rainfall.

The patterns of RH and $-\omega$ are notably different in the eastern and western sectors (right and left columns of Fig. 4.6). In the eastern sector, ascent and positive RH anomalies are narrowly focused within the equatorial belt while in the western sector the RH and $-\omega$ anomalies are elevated and exhibit an equatorial minimum, consistent with Fig. 4.3 in AW2. These distinctions are also apparent in the meridional profiles shown in the lower panels of Fig. 4.6. The western sector is characterized by weaker equatorial rainfall anomalies but stronger RH and OLR anomalies than the eastern sector. This difference is likely a reflection of the different cloud populations: the eastern sector is dominated by convective clouds that cover less area than the broad, stratiform anvils in the western sector (Lau and Wu 2010; Barnes and Houze 2013, among others).

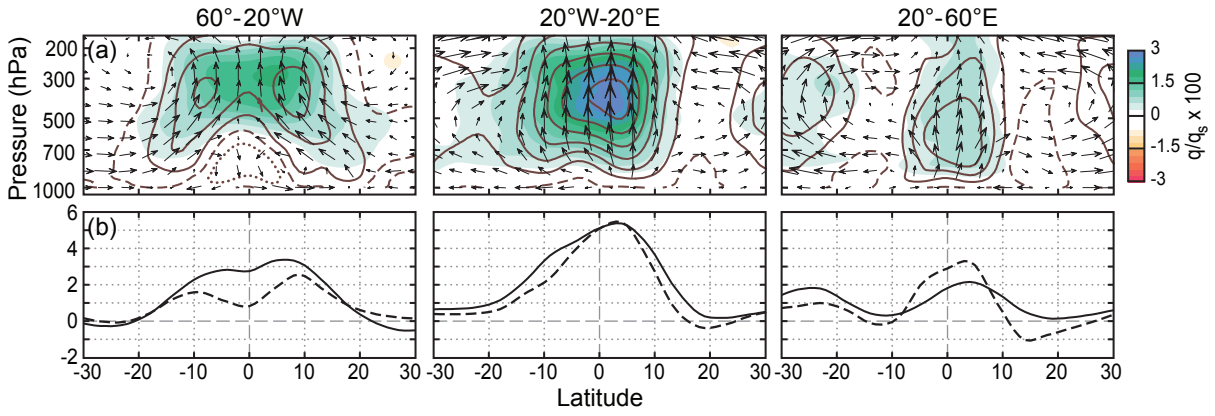

Figure 4.6: Composite meridional cross sections partially averaged in regions defined as western sector extending from 20° to 60° to the west of the RL (left column), the central sector (within 20° of the RL, middle column) and the eastern sector (20°−60° to the east of the RL, right column). (a) Meridional mass circulation (arrows), RH (shading), and $-\omega$ (contours). Contour interval 1 hPa day^{-1}. The largest meridional flux vector is ∼0.1 kg m^{-2} s^{-1}, and the largest vertical flux vector ∼4 × 10^{-4} kg m^{-2} s^{-1}. (b) −OLR (solid, in W m^{-2}), and TRMM precipitation rate × 5 (dashed, in mm day^{-1}).

Figure 4.7 shows meridional cross-sections of the individual terms in Eq. 4.1. The

distribution of q is included in the top row for reference, and contours showing the zonal mass flux ρu are superimposed as contours. The second row shows the moisture tendency, $\partial q/\partial t$. In the eastern sector, a moistening tendency is observed above the layer in which the q anomalies are a maximum, within a region of anomalous easterlies. In the central and western sectors a drying tendency is observed, collocated with lower-tropospheric westerly winds. The region of westerlies and drying widens from the central sector to the western sector. Rows (c)-(e) show the contributions from vertical moisture advection, Q_2, and their net contribution, respectively. In the eastern and central sectors the moistening of the equatorial mid-troposphere by the vertical advection term exceeds the moisture sink Q_2, and there is net moistening. The region to the west exhibits a more complex pattern. The vertical advection term produces moistening in the off-equatorial plumes of ascent identified in AW2. Below 700 hPa, anomalous descent produces drying in the equatorial belt. The net contribution of vertical advection and Q_2 is moistening in the outer tropics and drying in the equatorial lower troposphere.

The bottom row of panels in Fig. 4.7 (row f) shows the contribution of horizontal moisture advection to the observed tendency. In the eastern sector, the contribution from the horizontal advection term is negligible within the equatorial belt and positive poleward of 10°N/S. In the central sector horizontal moisture advection produces significant drying in the equatorial lower troposphere, which roughly balances the net moistening due to the vertical advection and Q_2 terms. The remaining drying tendency observed beneath the 700 hPa level is dominated by the contribution of horizontal moisture advection within that layer. Horizontal moisture advection dries a wider swath of the lower troposphere in the western sector, where it outweighs the net effect of the other terms in the balance. That the composite horizontal advection term is small in the eastern sector supports the notion that vertical velocity plays an important role in the eastward propagation of the MJO. However, horizontal moisture advection is strongly dependent on the phase of the MJO, as discussed in Section 4.4.

Figure 4.8 shows the individual contributions of the zonal (row a) and meridional (row

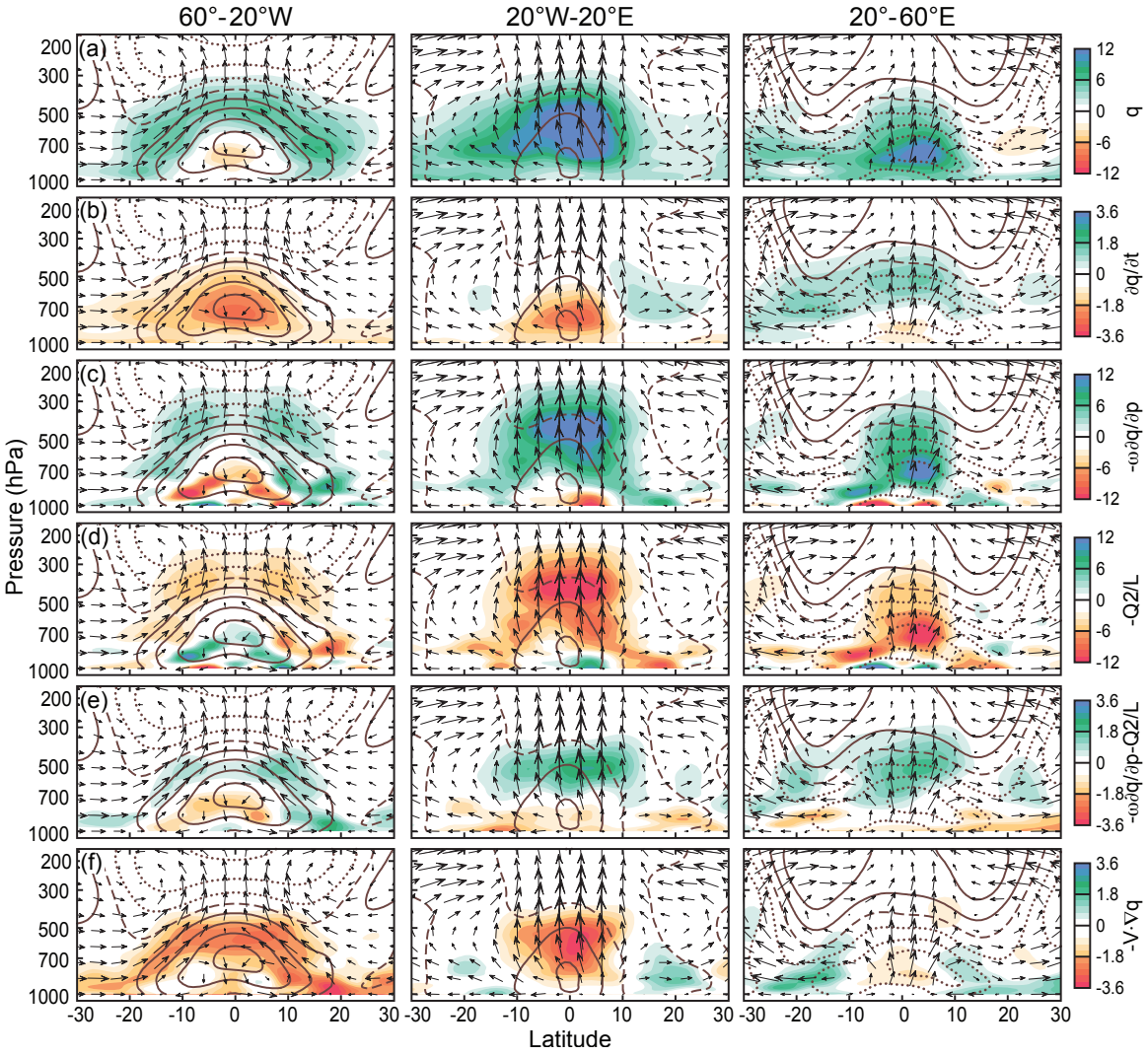

Figure 4.7: Meridional cross sections as in the top row of Fig. 4.6 but contours depict the zonal mass circulation ρu. Shaded fields in the respective columns correspond to: (a) specific humidity q, (b) specific humidity tendency $\partial q/\partial t$, (c) vertical moisture advection, (d) the apparent moisture source/sink, (e) the sum of the vertical moisture advection and the apparent moisture source/sink, and (f) horizontal moisture advection. Contour interval 0.15 kg m^{-2} s^{-1}. Shading is in units of 10^{-1} g kg^{-1} for q, 10^{-1} g kg^{-1} day^{-1} for $\partial q/\partial t$, and 10^{-2} g kg^{-1} day^{-1} for panels $(c)-(f)$.

b) wind components to the observed pattern of horizontal advection in Fig. 4.7f. Advection

of moisture by the zonal wind component is dominant in the central sector, while advection by the meridional component is mainly responsible for the strong drying tendency in the western sector and the moistening in the eastern sector. That the meridional component produces significant drying and moistening is indicative of the role of Rossby waves.

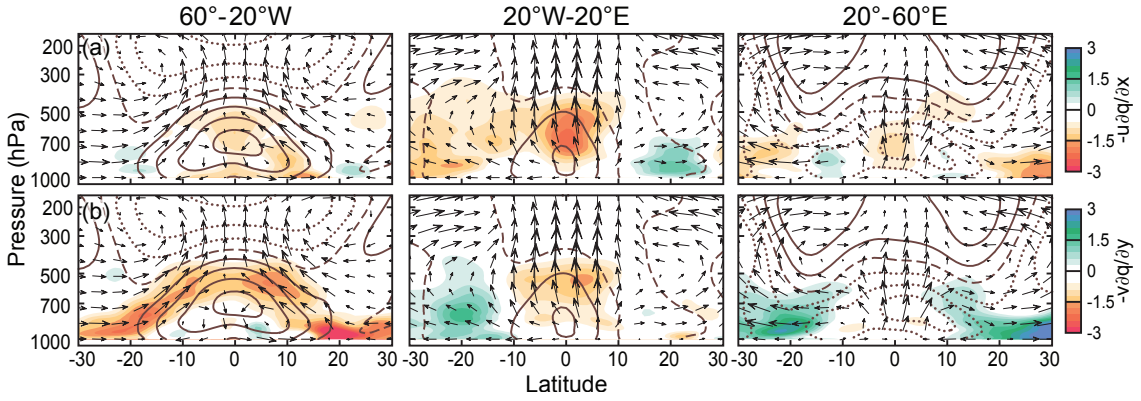

Figure 4.8: As in Fig. 4.7 but the shaded fields depict the advection of moisture by the zonal flow ($-u\partial q/\partial x$, row a) and the meridional flow ($-v\partial q/\partial y$, row b). Contour interval 0.15 kg m^{-2} s^{-1}. Shading in units of 10^{-2} g kg^{-1} day^{-1}.

4.2.3 Horizontal Maps

Figure 4.9 shows a series of horizontal maps summarizing and interrelating the salient features shown in Figs. 4.4-4.8. Vertical moisture advection averaged over the 250−600 hPa layer, shown as the shaded field in panel (a), is nearly identical in structure to the field of ω_1 (contoured), both exhibiting a characteristic "swallowtail" shape. Because ω_1 is related to the integral of the divergence averaged over the depth of the lower troposphere, it follows that:

$$\left\langle \omega \frac{\partial q}{\partial p} \right\rangle_{250-600hPa} \propto Div_{BL} + Div_{FT} \tag{4.3}$$

where Div_{FT} and Div_{BL} represent divergence occurring over the lower free troposphere (FT, 500−850 hPa) and the boundary layer (BL, 850−1000 hPa). In other words, moistening in

the mid-troposphere due to vertical moisture advection occurs when the vertically-integrated (surface to 500 hPa) divergence is negative. Figure 4.9*b* shows vertical moisture advection averaged over the layer just above the BL (700−850 hPa) superimposed upon the BL divergence. These two fields also exhibit nearly identical structures, consistent with the fact that

$$\left\langle \omega \frac{\partial q}{\partial p} \right\rangle_{700-850hPa} \propto Div_{BL} \tag{4.4}$$

or more generally that upward moisture advection at given level of the atmosphere is proportional to the vertically-integrated mass convergence in the underlying layer.

It is evident from Fig. 4.9*c* that neither the negative negative OLR anomalies, that define the region of extensive elevated cloud tops, nor anomalous lower free tropospheric convergence (Div_{FT}) exhibit the swallowtail shape characteristic of the ω_1 and the rainfall fields, and they are both displaced slightly to the west of the RL. Convergence within this layer of the atmosphere is predominantly induced by wave convergence, and its horizontal structure and corresponding wind field are qualitatively consistent with the shallow water, forced wave solutions of Matsuno (1966) and Gill (1980), as further documented in Fig. 4.13 of AW2. In contrast, it is evident from panels (*a*)-(*c*) in Fig. 4.1 and Fig. 4.6 that ascent, rainfall and specific humidity anomalies are stronger to the east of the RL. Thus, the region of ascent to the east of the RL, which appears to be moistening the mid and upper troposphere (Fig. 5.5*a*, Fig. 4.7), is fueled by BL convergence. Hence the frictional moisture convergence can be viewed as driving eastward propagation of the region of enhanced convection, as argued by Wang (1988); Maloney and Hartmann (1998); Hsu and Li (2012); among others. These results are also in agreement with studies by Hohenegger and Stevens (2013); Masunaga (2013); Kumar et al. (2014); and Hagos et al. (2014) who found that upward advection of moisture by the planetary-scale vertical velocity field is responsible for most of the mid- to upper tropospheric moistening, and with Fig. 5.5*a*, which shows that vertical moisture advection is mainly responsible for moistening the mid troposphere near and to the east of the RL.

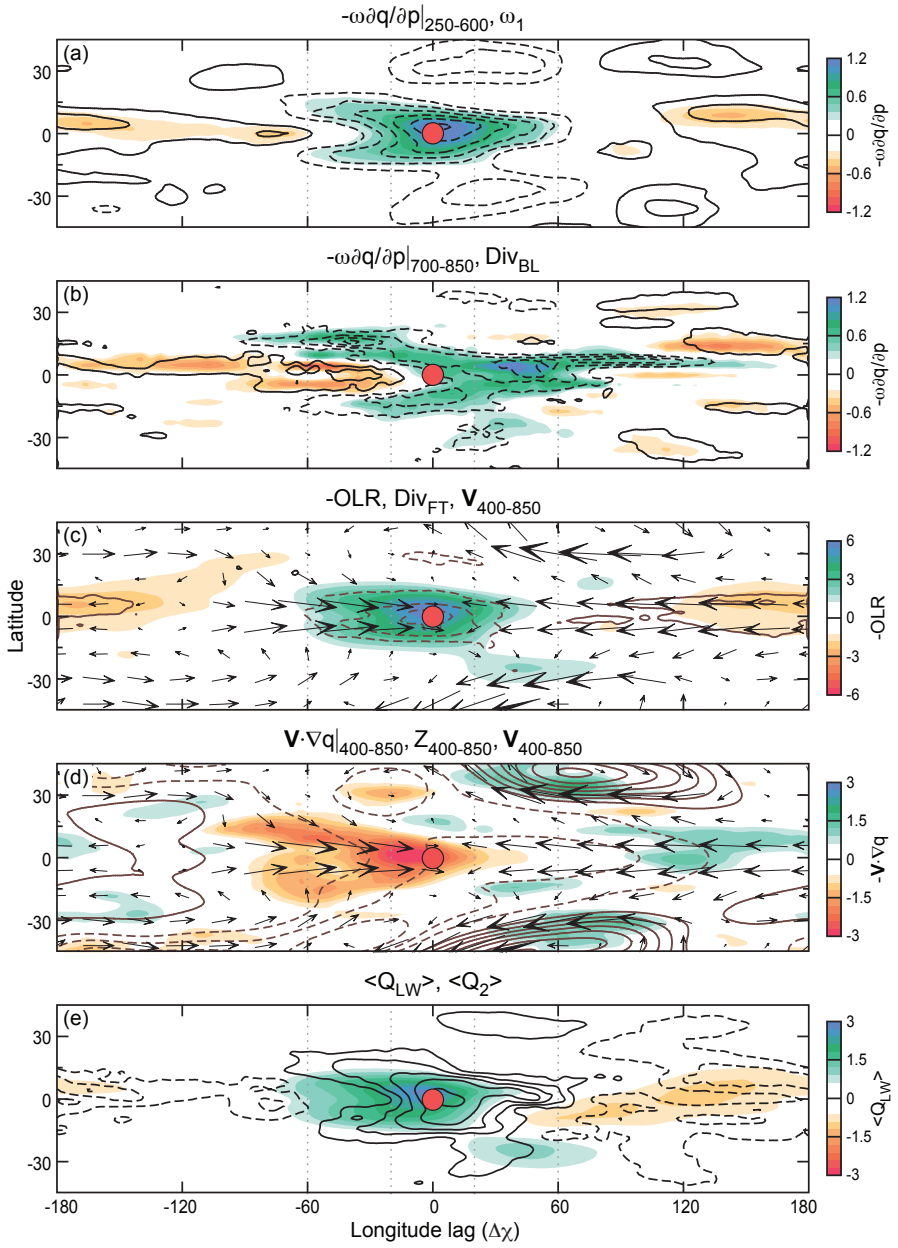

Figure 4.9: Composite maps of (a) vertical moisture advection averaged over the 250-600 hPa layer (shaded) and ω_1 (contoured) scaled to its 300 hPa value, (b) vertical moisture advection averaged over the 700-850 hPa layer (shaded) and boundary layer (BL, 850-1000 hPa) divergence (contoured), (c) OLR anomalies (shaded) and free-tropospheric (FT, 500-850 hPa) divergence (contoured), (d) horizontal moisture advection (shaded), geopotential height (Z, contoured) and winds (arrows) averaged over the 400-850 hPa layer, and (e) vertically integrated heating due to latent heat release $\langle Q_2 \rangle$ (contoured) and vertically integrated longwave radiative heating $\langle Q_{LW} \rangle$ (shaded, in units of J m^{-2}). Contour interval 1 hPa day^{-1} for ω_1, 0.5 $\times$ 10^{-7} s^{-1} for divergence and 1 m for Z. Shading is in units of 10^{-1} g kg^{-1} day^{-1} for panels a and b, W m^{-2} for panel c, 10^{-2} g kg^{-1} day^{-1} for panel d, and 0.1 mm day^{-1} ($\sim$3 J m^{-2}) for panel (e).

Figure 4.9*d* shows horizontal moisture advection overlain by Z and wind anomalies, averaged from 400 to 850 hPa. The pattern of horizontal moisture advection is nearly identical to the pattern of drying tendencies shown in Fig. 4.1*d*, further indicating the importance of horizontal moisture advection in drying the lower troposphere near and to the west of the RL. It is shown in the Appendix that horizontal moisture advection is dominated by the advection of the climatological-mean moisture field by the MJO-related anomalous wind field.

Because Q_2 is a large contributor to the total diabatic heating Q in the MJO, which maintains its large scale circulation pattern (Lin and Mapes, 2004b; Jiang et al., 2011), it is of interest to compare its spatial pattern with the heating pattern induced by radiation Q_R. Figure 4.9*e* shows a composite of the dominant components of vertically integrated diabatic heating, defined as $\langle Q \rangle \approx \langle Q_2 \rangle + \langle Q_{LW} \rangle$, where Q_{LW} is the contribution to diabatic heating from longwave radiation, which dominates the contribution of radiative transfer to Q (Lin and Mapes, 2004b; Bony and Emanuel, 2005; Johnson et al., 2014).

$\langle Q_2 \rangle$, which is approximately the difference between precipitation and evaporation in a closed moisture budget exhibits the distinctive "swallowtail" shape that characterizes the distributions of water vapor, precipitation and ω_1, suggesting that $\langle Q_2 \rangle$ is dominated by precipitation in regions of deep tropospheric ascent. That Q_2 exhibits this swallowtail structure and is shifted to the east of the FT convergence reflects the important contribution of BL friction to the observed structure of vertical motion and convection in the MJO.

If we compare the horizontal distribution of $\langle Q_2 \rangle$ to the TRMM-3B42 precipitation (P_{TRMM}) we find that $\langle Q_2 \rangle$ more closely resembles the pattern in precipitation from TRMM-3B42 over the equatorial belt (10°N/S) than the precipitation output from ERA-Interim shown in Fig. 4.1, in which the precipitation anomalies are displaced eastward. Since the contribution of surface evaporation to $\langle Q_2 \rangle$ is negligible in this warm pool composite reference frame (Fig 4.10), it follows that it is the "residual" in the moisture budget that accounts for the lack of this eastward displacement in $\langle Q_2 \rangle$. However, both $\langle Q_2 \rangle$ and P_{ERA-I} are smaller than P_{TRMM} by nearly a factor of two, and the discrepancies are especially large to the west

of the RL, where stratiform ascent (negative ω_2) is prevalent. This result is analogous those found by Mapes and Bacmeister (2012) for the MERRA reanalysis, which suggests that the the "residual" in the ERA-Interim reanalysis is mainly a reflection of the deficiencies in the simulation of precipitation.

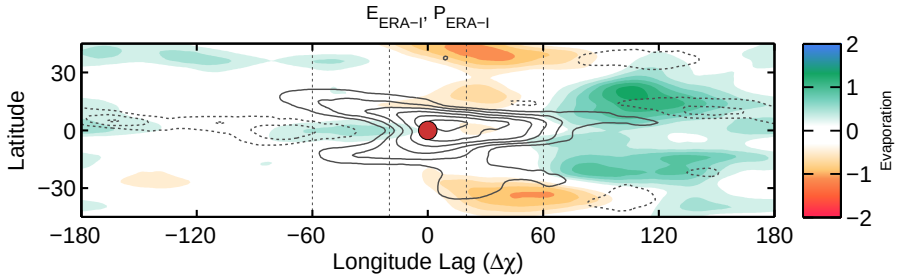

Figure 4.10: Warm pool omposite map of ERA-Interim anomalous surface latent heat flux (evaporation, shaded) and precipitation (contoured). Contour interval 0.1 mm day^{-1}.

Diabatic heating due to longwave radiation (the shaded field in Fig. 4.9*e*) exhibits a horizontal pattern similar to that of OLR (see Fig. 4.9*c*). It is ∼1/6 as large as $\langle Q_2 \rangle$ but is shifted to the west of the maximum in precipitation such that it explains 10-20% of the total heating in the western sector where $\langle Q_2 \rangle$ is smaller. The shortwave heating (not shown) is about half the magnitude of $\langle Q_{LW} \rangle$ and also exhibits a "swallowtail" shape. Thus, it can be said that diabatic heating in the MJO is dominated by latent heat release, augmented and spatially offset by longwave radiative heating.

4.3 Are the MJO-related ω and q fields linearly related?

Results of several previous studies have indicated that vertical motion is highly correlated in space and time with the moisture field (Raymond and Fuchs, 2009; Holloway and Neelin, 2009). In this section we explore the possibility of diagnosing relative humidity (RH) and q based on the observed three dimensional structure of ω, building upon the results presented in the two previous sections.

Here, we determine the degree to which MJO-related perturbations in RH and ω, scaled by a pressure dependent factor, are linearly related; i.e.:

$$RH^* = \frac{q^*}{\bar{q}_s} \approx -bp^{-n}\omega \tag{4.5}$$

where RH^* and q^* are the diagnostically-derived relative humidity and specific humidity fields and b is a pressure-independent scaling constant. RH^* is calculated by dividing q^* by the value of the mean saturation specific humidity $\bar{q}_s$ at a given pressure level p. To estimate n, we regress RH on ω at each individual pressure level to obtain the slope b, as shown in Fig. 4.11a. Note that the slopes of the clouds of points, which determine the values of b, are pressure dependent. Values of $\log b$ are then plotted versus $\log p$, as shown in Fig. 4.11b; and n in Eq. (4.5) is determined from the slope of the least squares best fit regression line, which is $\sim$0.4. Substituting this value into Eq. (4.5), we can now merge the data for all pressure levels and estimate b based on the full, three dimensional RH and ω fields. Since we are only interested in humidity anomalies in the free troposphere, we base this calculation on data for all pressure levels from 850 to 250 hPa. We include every third ERA-Interim grid point equatorward of 10°N/S in our warm pool composites, equivalent to a 4.5° longitude × 4.5° latitude grid. The resulting scatterplot is shown in Fig. 4.11c, and the value for b obtained through a least squares best fit is -4.94. The values of RH^* and q^* are obtained from Eq. (4.5) using the ω and $\bar{q}_s$ fields from the reanalysis data with these empirically-derived coefficients.

Figure 4.11c shows a scatterplot of RH versus RH^*. A robust fit between the two fields is observed, with a correlation coefficient of 0.95. Figure 4.2c shows the values of q^* and RH^* as estimated from Eq. (4.5) using the empirically derived regression line in Fig. 4.11c. These estimated values agree well with the observed values within 60° of the RL (Fig. 4.2a), both in terms of the amplitude and the positioning of the features. Using Eq. (4.5) leads to a slight overestimate of the negative q anomalies in the lower free troposphere $\sim$45° to the west of the RL, and to an underestimate the anomalies above the boundary layer beyond

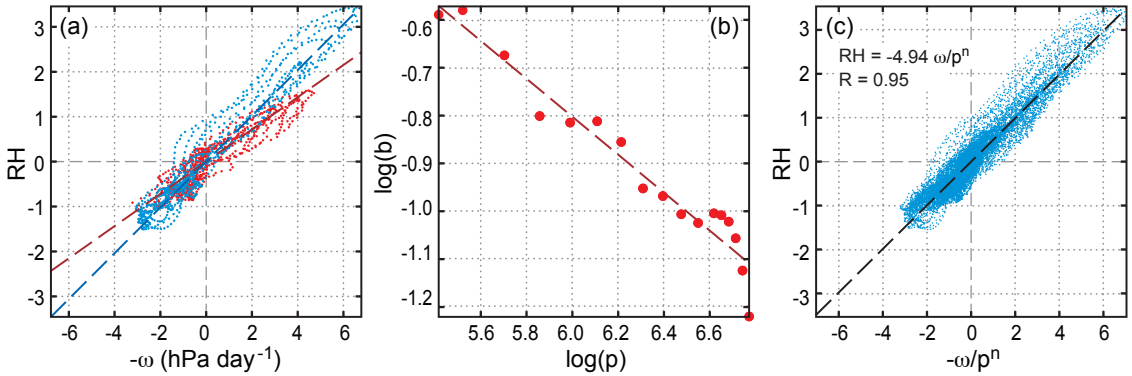

Figure 4.11: (a) Scatterplot of RH (in percent) against ω for every third grid point in the equatorial belt (<10°N/S) for the 700 hPa level (red) and 300 hPa layer (blue). The best fit linear regression is depicted as a dashed line. (b) Scatterplot and linear least squares fit for $\log b$ of the linear regression of RH on ω at each pressure level between 850 and 250 hPa, as a function of $\log p$. (c) Scatterplot of RH against ω/p^n based on data for all pressure levels from 850 to 250 hPa equatorward of 10°N/S. The best fit linear regression for all points is shown in the top left corner as well as the correlation coefficient. The sign of ω is reversed for presentation.

60° to the east of the RL.

The horizontal distributions of the diagnostic q^* and the discrepancies $q - q^*$, vertically integrated in the free tropospheric layer ranging from 250 to 850 hPa, are shown in Fig. 4.12. The inferred q^* captures the elongated swallowtail structure characteristic of the q field (Fig. 4.1c). The discrepancies $q - q^*$ are roughly 1/3 as large as the q anomalies themselves. The departures reflect the fact the q^* anomalies are too narrowly focused on the equator and they don't extend as far eastward as the q anomalies do. That $q^* > q$ to the east of the reference longitude within the equatorial belt and $q^* < q$ to the west indicates that the observed q anomalies are displaced slightly westward of the ω anomalies. This zonal displacement within the equatorial belt suggests that there exists a time delay between the anomalous ascent and positive q that is not taken into account in the diagnostic estimate.

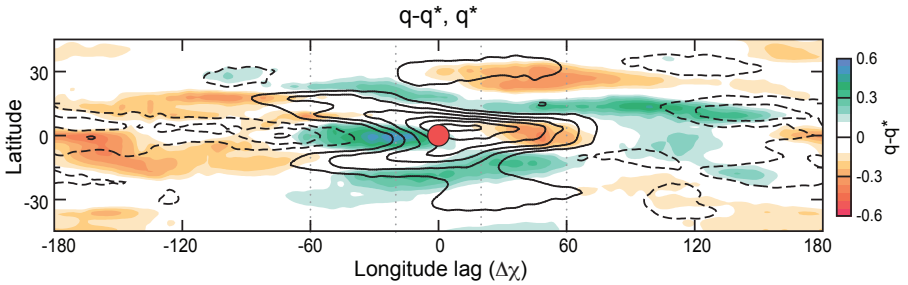

Figure 4.12: Composite map of q^* (contoured) and $q^* - q$ (shaded) vertically integrated from 250-850 hPa. Contour interval 0.125 kg m^{-2}.

4.4 Representation of the MJO dipole phase using warm pool composites

The warm pool composite described in the previous sections represents the mean structure of the MJO as it propagates across the Indo-Pacific warm pool. In this section we discuss the interpretation of this composite in the context of the time-dependent MJO cycle. Figure 4.13 shows a 5-panel sequence of the vertically-integrated horizontal moisture advection $-\langle \mathbf{V} \cdot \nabla q \rangle$ and $\partial \langle q \rangle / \partial t$. As noted in Chapter 2, our warm pool composites are constructed by averaging multiple maps based on many different linear combinations of PC1 and PC2 of $\Delta\chi$, whereas these 5-panel sequences represent discrete linear combinations. The patterns for discrete phases are much noisier than the warm pool composites shown in previous figures so we have meridionally averaged them from 10°S to 10°N to make the features of interest more clearly visible.

It is evident from Fig. 4.13 that horizontal moisture advection is an important contributor to the moisture tendency over the eastern Indian Ocean and the Maritime Continent at the time of minimum PC2 (top panel), which corresponds to the MJO phase when the equatorial heat source is characterized by a dipole, with suppressed convection over the western Pacific and enhanced convection over the central Indian Ocean. Maps of OLR at these times are shown in Fig. A2 of AW2. In this phase of the MJO cycle, the circulation anomalies over the Maritime Continent are influenced not only by the enhanced convection over the central

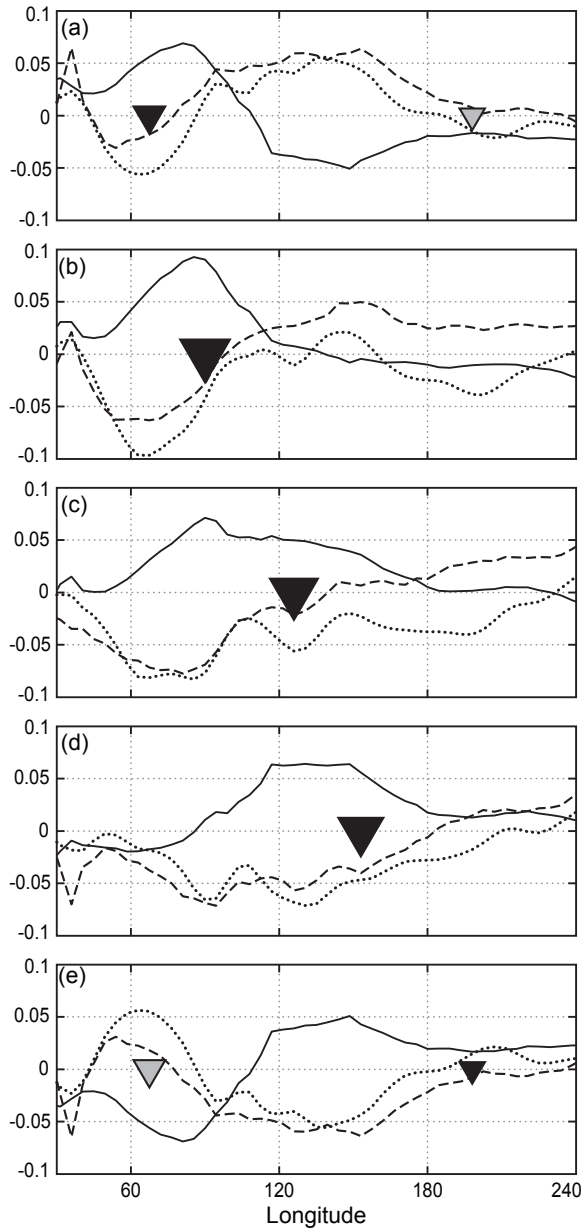

Figure 4.13: Five-panel sequence of −OLR (solid), and vertically-integrated $\partial q/\partial t$ (dashed) and horizontal moisture advection $-\langle \mathbf{V} \cdot \nabla q \rangle$ (dotted) meridionally averaged from 10°S−10°N, regressed on linear combinations of PC1 and PC2 of $\Delta\chi$: (*a*) −PC2, (*b*) (PC1 − PC2)/$\sqrt{2}$ (*c*) PC1, (*d*) (PC1 + PC2)/$\sqrt{2}$; and (*e*) PC2. The black and gray triangles indicate $\Delta\chi$ maxima and minima, respectively, and are sized accordance with the amplitude of the $\Delta\chi$ maximum/minimum. The *y*-axis is in units of kg m^{-2} day^{-1}. OLR has been arbitrarily scaled for reference.

Indian Ocean but also by the suppressed convection over the western Pacific. At other times in the MJO cycle, horizontal advection plays a lesser role in moistening the atmosphere to the east of the enhanced convection, and the structures of horizontal advection and $\partial\langle q\rangle/\partial t$ more closely resemble the warm pool composites presented in the previous sections.

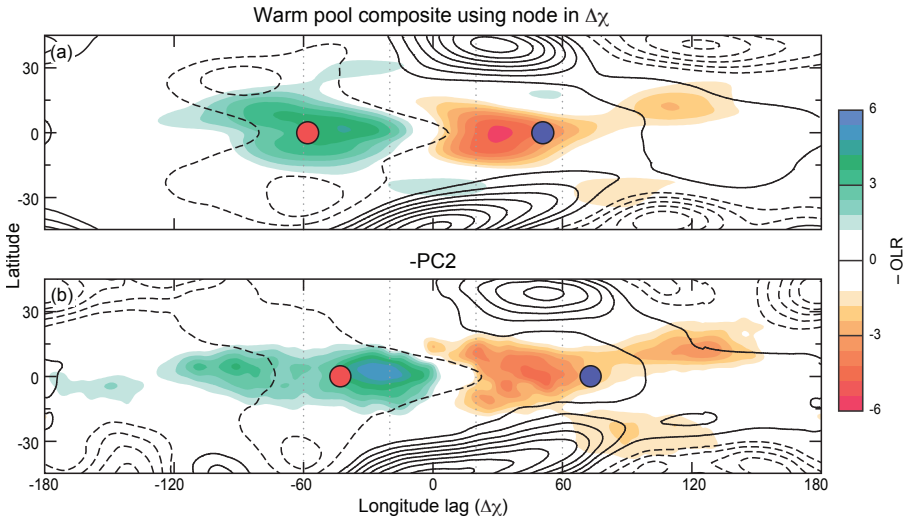

Figure 4.14: (a) Warm pool composite, constructed by using the node in $\Delta\chi$ as the reference longitude instead of the maximum in $\Delta\chi$ (see Chapter 4.4 for further details), showing OLR (shaded) and 500-1000 hPa averaged Z. (b) As in the top panel but showing the MJO-related fields at the time when PC2 is a negative maximum. Red and blue circles depict the $\Delta\chi$ maximum and minimum, respectively. Contour interval 1 m.

In order to obtain a more robust description of the MJO's moisture budget at the time when PC2 is a minimum, we created a warm pool composite analogous to those presented in the previous sections, but zonally shifted such that the node in $\Delta\chi$ in which $\partial\Delta\chi/\partial x$ is negative corresponds to the reference longitude (0°). The resulting composited Z and OLR patterns, shown Fig. 4.14a, are remarkably similar to the observed patterns for this phase, shown in panel (b). Hence, much of the noise in the patterns for individual MJO phases can be eliminated by using phase-shifted warm pool composites as building blocks for reconstructing the evolving MJO structure.

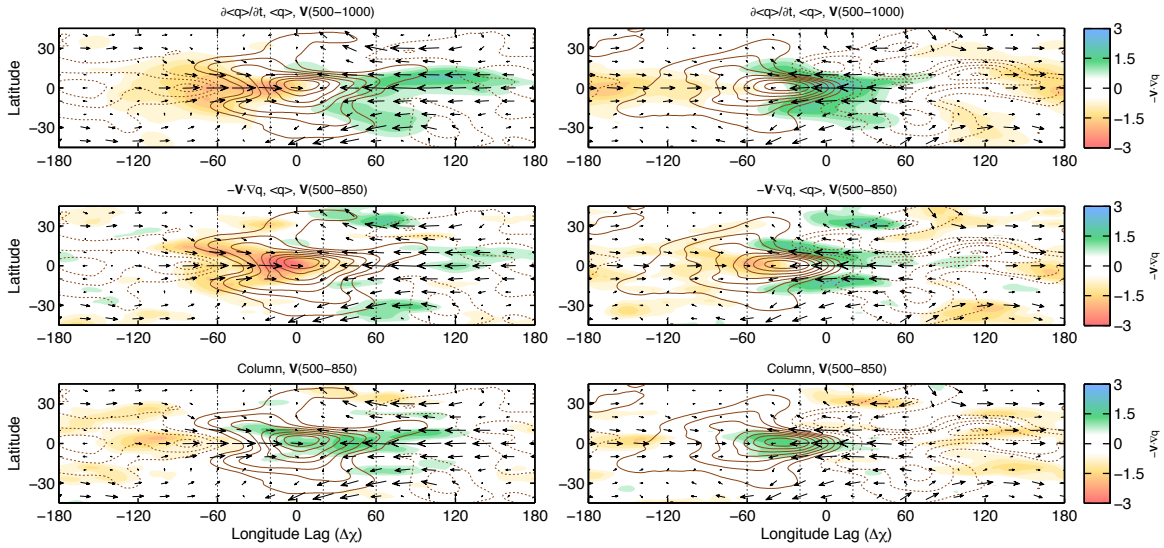

Figure 4.15: As in Fig. 4.9*d* but for but for a warm pool composite made by using the node in $\Delta\chi$ as the reference longitude, and showing $\langle q \rangle$ as the contoured field. Contour interval 0.125 kg m^{-2}.

Now we will use this approach to obtain a more comprehensive understanding of the role of horizontal moisture advection in moistening the atmosphere to the east of the region of enhanced convection over the Indian Ocean at the time of minimum PC2. Figure 4.15 shows the warm pool composite obtained using the node in $\Delta\chi$ as the RL, for the fields of $\langle q \rangle$, lower free-tropospheric wind and horizontal moisture advection. Horizontal moisture advection at this time exhibits the distinctive swallowtail shape observed in $\langle q \rangle$, ω_1, and other fields in our warm pool composites (see Fig. 4.1), but whose maximum is instead centered $\sim$20° to the east of the RL, near the node in the $\langle q \rangle$ field. This pattern is dominated by advection of moisture by the meridional wind component, though the contribution from the zonal wind component is large $\sim$20° to the east of the RL (not shown). The maximum in $\langle q \rangle$ occurs along the equator between the wings of the swallowtail, analogous to its positioning in Fig. 4.1*d*. This distinctive structure indicates that at the time of minimum PC2 horizontal advection contributes to the eastward propagation of the MJO and acts to widen the plume of ascent

associated with the positive moisture anomalies over the equatorial Indian Ocean.

Longitude-height cross sections of the moisture budget terms for the dipole case are shown in Fig. 4.16. Relative to the positive center of action in $\Delta\chi$, indicated by the red triangle, the patterns are similar, but horizontal moisture advection makes a more important contribution to moistening the lower free-troposphere to the east of the maximum in $\Delta\chi$.

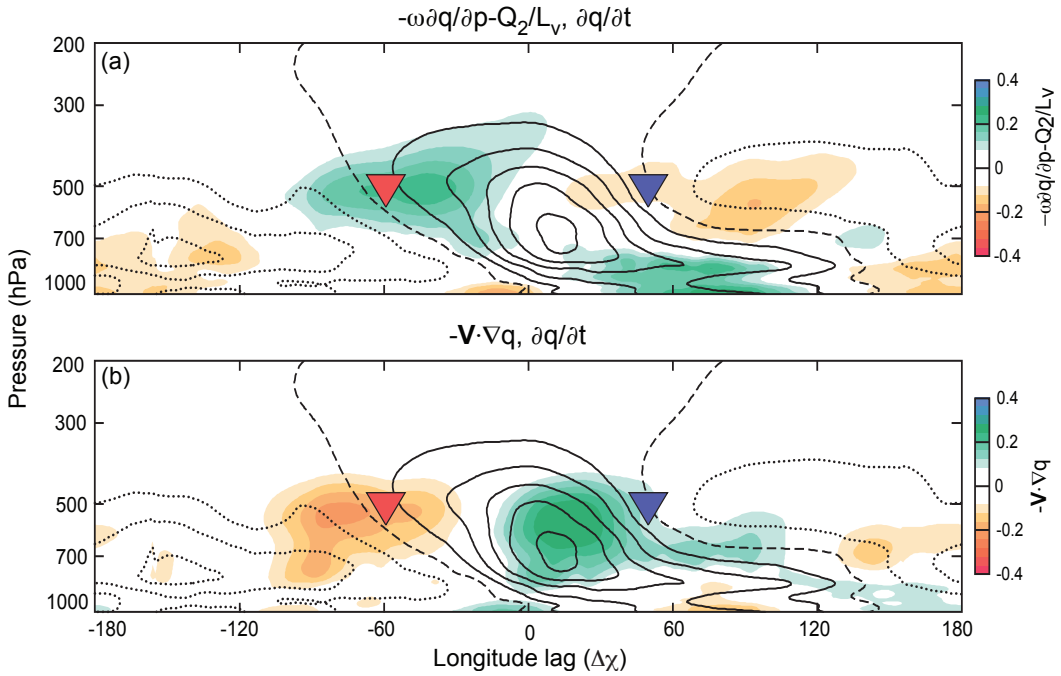

Figure 4.16: Composite longitude-height cross sections, analogous to those in Fig. 4.5 but for a warm pool composite made by using the node in $\Delta\chi$ as the reference longitude. Red and blue triangles depict the $\Delta\chi$ maximum and minimum, respectively. Superposing the shaded fields in the two panels yields the contoured field.

It is notable that in the reconstructed $-$PC2 composite shown in Fig. 4.16, the moistening tendency centered $\sim 60^\circ$ to the east of the $\Delta\chi$ maximum (the red triangle) is much stronger than the drying tendency to the west of it, and stronger than both the positive and negative $\partial q/\partial t$ anomalies in the simple warm pool composite in Fig. 5.5. Hence, the dipole configuration observed at the time of minimum PC2 contributes not only to the eastward

phase propagation but also the amplification of the moisture anomalies to the east of the center of enhanced convection, thereby strengthening the MJO-related enhanced convection as it moves into the middle of the warm pool sector.

4.5 Decomposition of the horizontal advection field

In previous sections, we analyzed the horizontal and vertical advection fields as MJO-related anomaly fields. As was shown in previous studies (Maloney, 2009; Kiranmayi and Maloney, 2011; Hsu and Li, 2012), these terms can be decomposed into the contribution from the low-frequency background state (LFBS, denoted by overbears) and eddy components (denoted by a prime) in order to analyze how interaction across different timescales shapes the MJO-related moisture budget. It was shown by Hsu and Li (2012) that vertical advection of moisture is mainly a reflection of the vertical advection of mean moisture by the anomalous ascent ($-\omega'\partial\bar{q}/\partial p$). However, it is not entirely clear from an inspection of Fig. 4.9*d* which of these terms shape the horizontal advection field. In this section, we decompose the horizontal advection field into its contributions from the climatological-mean background flow and the MJO-related anomaly:

$$(-\mathbf{V}\cdot\nabla q)^* \approx (-\mathbf{V}'^*\cdot\nabla\bar{q})^* + (-\bar{\mathbf{V}}\cdot\nabla q')^* + (-\mathbf{V}'\cdot\nabla q')^* \tag{4.6}$$

where the first term on the right hand side denotes the horizontal advection of background moisture by the anomalous winds, the second term is the advection of anomalous moisture by the background winds and the third term denotes the advection of the anomalous moisture by the anomalous winds. In this section, the LFBS and the eddy components are separated by using a 101-point Lanczos filter (Duchon, 1979) with a 100 day cutoff period. For reference, the annual mean and seasonal distributions of wind and column-integrated water vapor can be found in the ERA-40 Atlas (Section C in Kållberg et al. 2005). Note that asterisks correspond to the MJO-related anomalies.

In agreement with results from Maloney and Esbensen (2003), Kiranmayi and Maloney

(2011), and AW3, the non-linear term is dominated by moisture advection from eddies of frequencies higher than one cycle per 20 days (not shown). The other two terms are dominated by interactions of the intraseasonal (20-100 day) anomalies with the low-frequency background state, so that the following approximation is satisfied

$$-(\mathbf{V}' \cdot \nabla \bar{q})^* \approx -(\mathbf{V}^* \cdot \nabla \bar{q})^*$$

$$-(\bar{\mathbf{V}} \cdot \nabla q')^* \approx -(\bar{\mathbf{V}} \cdot \nabla q^*)^*$$

$$-(\mathbf{V}' \cdot \nabla q')^* \approx -(\mathbf{V}'' \cdot \nabla q'')^*$$

where the double primes denote a 20-day timescale highpass filter.

Warm pool composites of the four terms in Eq. (4.6), analogous to the one shown in Fig. 4.9*d*, are shown in Fig. 4.17. It is clear that the advection of mean moisture by the anomalous winds ($-\mathbf{V}' \cdot \nabla \bar{q}$), shown in panel (*b*), dominates the total horizontal moisture advection at all locations, exhibiting a shape nearly identical to that of the total horizontal advection field (shown in Fig. 4.17*a*) except near the RL, where the moisture gradient in the background field is weak. Drying in this sector is dominated by horizontal moisture advection resulting from the non-linear term ($-\mathbf{V}' \cdot \nabla q'$, panel *d*). It was found by Maloney and Esbensen (2003) and Kiranmayi and Maloney (2011) that an increase in high-frequency transient variability within the convectively active phases of the MJO enhances drying by horizontal moisture advection, and vice versa for suppressed phases.

Following Andersen and Kuang (2012) and Arnold et al. (2013), we assess the relative importance of the terms in Eq. (4.6) to the propagation of the rain bands by comparing the strength of their projections upon the column-integrated moisture tendency

$$S_t(F) = \frac{||F \cdot \partial \langle q' \rangle / \partial t||}{||\partial \langle q' \rangle / \partial t \cdot \partial \langle q' \rangle / \partial t||} \tag{4.8}$$

where F is the term in Eq. (4.6) and $||()||$ is the integral of () over the domain 30°N/S and

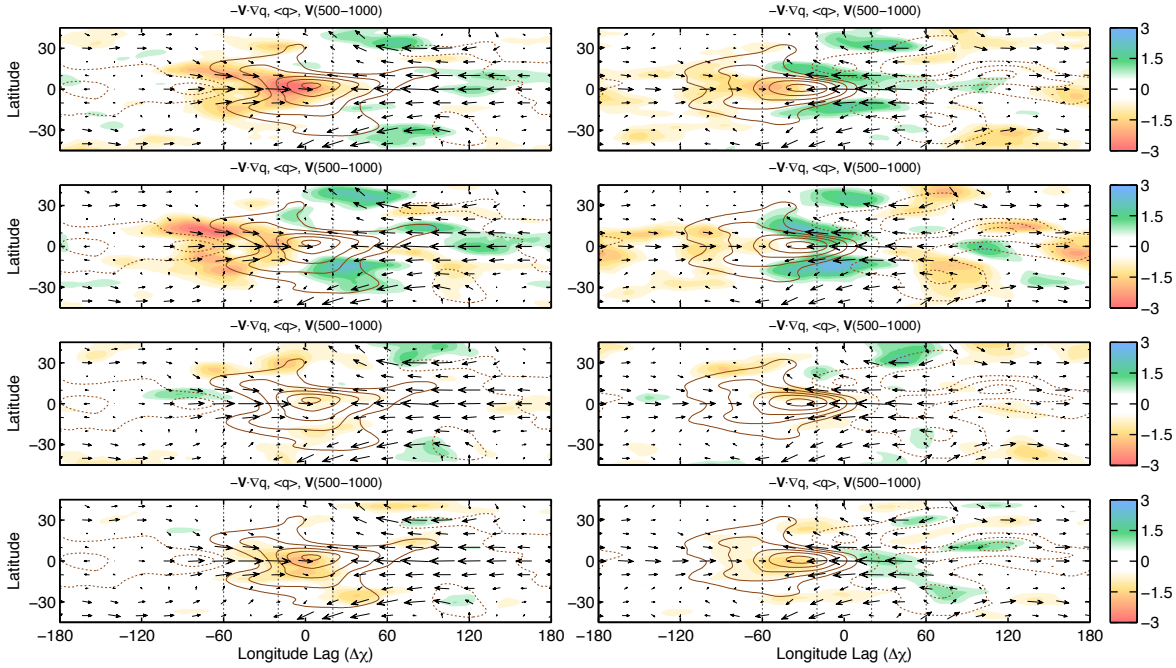

Figure 4.17: Composite maps of horizontal moisture advection (shaded), column integrated water vapor $\langle q \rangle$ (contours), and winds (arrows) averaged over the 400-850 hPa layer. Total anomalous horizontal moisture advection is shown in panel (a). Panel (b) shows the horizontal advection of background moisture by the anomalous winds, panel (c) shows the advection of anomalous moisture by the background winds and panel (d) shows the advection of the anomalous moisture by the anomalous winds.

within 90° east and west of the reference longitude. The results, shown in Fig. 4.18 are insensitive to the domain choice. Advection of mean moisture by the anomalous meridional flow is the dominant term in the budget, contributing to ∼40% of the total moisture tendency. Column processes and nonlinear horizontal moisture advection by high frequency eddies also contribute significantly to the propagation of the moisture anomalies.

4.6 Does the MJO have a westward group velocity?

The differences in the moisture tendency at the time when the MJO is characterize by a dipole, versus those in which it is characterize as a monopole indicate that the region when

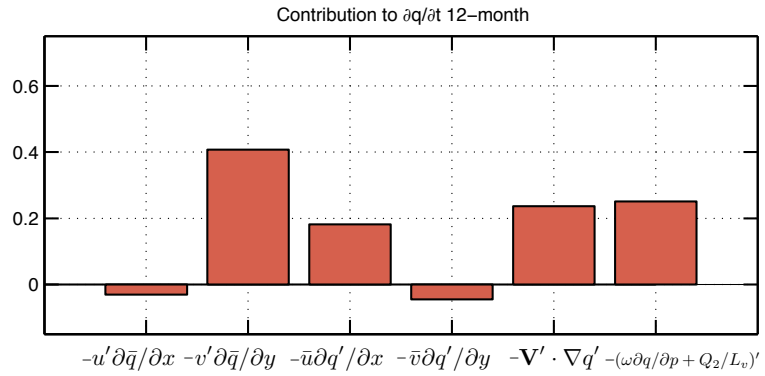

Figure 4.18: Normalized contribution of the individual terms in the column-integrated moisture budget (Eqs. 4.1 and 4.6) to the propagation of the moisture anomalies during an MJO cycle as defined by the warm pool composites. The contributions are obtained by using Eq. (4.8), projecting each term to the horizontal structure of column integrated moisture tendency within 120° to the east and west of the reference longitude and 30°N/S for the warm pool composites centered on PC1 and −PC2 of $\Delta\chi$.

the maximum drying and moistening tend to occur in regions where the Rossby wave response to a heat source is modulating the mean distribution of moisture through horizontal moisture advection. Because Rossby waves only develop to the west of the heat source, this tendency would imply that the regions of strongest enhanced and suppressed convection would drift westward with time throughout the MJO cycle. Figure 4.19 shows a time-longitude diagram of $\langle q \rangle$ and $\partial\langle q \rangle/\partial t$ lag regressed onto PC1 of $\Delta\chi$. A westward drift in both $\langle q \rangle$ and $\partial\langle q \rangle/\partial t$ is indeed observed.

Further documentation of the group velocity in the MJO is shown in Fig. 4.20. These time-longitude diagrams are warm pool composites based on data at lag day 0, as in the other figures shown in this Chapter. The left column shows composited OLR anomalies while the right column shows the OLR envelope, defined as

$$Env = 1/2\sqrt{R'^2 + (\tau_\alpha \partial R'/\partial t)^2} \tag{4.9}$$

where R' corresponds to the OLR anomaly field and τ_α is the timescale between maxima in

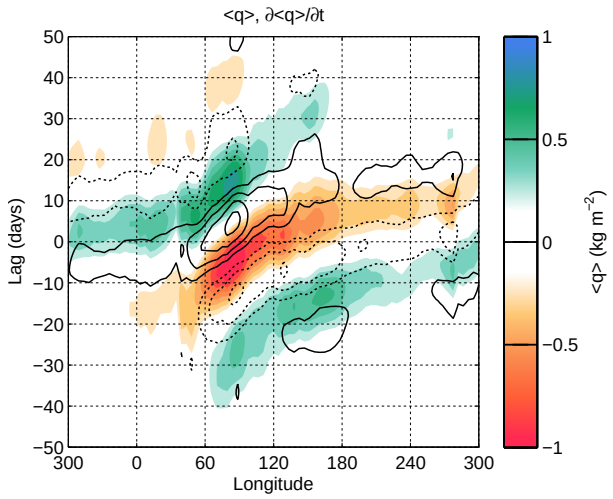

Figure 4.19: Time-longtiude diagram of $\langle q \rangle$ (shaded) and $\partial \langle q \rangle / \partial t$ (contoured) averaged over the equatorial belt 15°N/S. Lag day 0 corresponds to the time when PC1 of $\Delta\chi$ reaches a maximum. Contour interval 0.125 mm day^{-1}.

PC1 and PC2 of $\Delta\chi$ ($\tau_\alpha = 6.75$ days, see also AW1). In all four panels, it is clear that the anomalies drift westward with, suggesting that the MJO may be characterized by a westward group velocity. Traces of the circumnavigating Kelvin wave can also be observed, emanating to the east of the convective anomalies near lag day -10, and completing a global circuit near lag day 5. This circumnavigating wave modulates water vapor over the Atlantic basin and over Africa. However, traces of westward energy dispersion in the MJO cycle can be seen between lag days -30 and 0, well before the signature of the circumnavigating Kelvin wave is observed. Theoretical considerations as well as further discussion on this feature of the MJO will be shown in Part II.

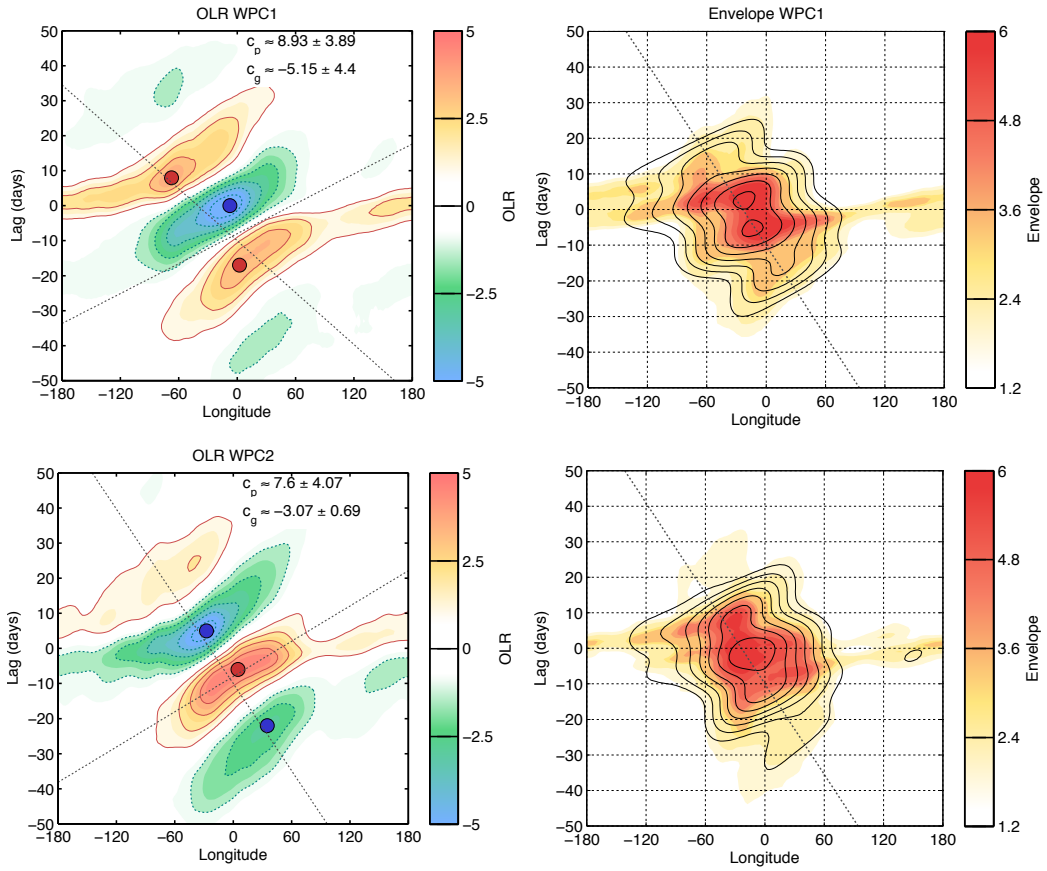

Figure 4.20: Warm pool composite time-longitude diagram. The top row shows warm pool composite time longitude diagrams for warm pool composites based on the maximum in $\Delta\chi$, as in Figs. 4.1-4.8, while the bottom row is based on maximum in $\partial\Delta\chi/\partial x$ as in Fig. 4.16. Contour interval 2 W m^{-2}. The red/blue circles depict the region where OLR is locally a maximum/minimum. The right column shows the OLR wave envelope, obtained through Eq. 4.9. OLR anomalies are shaded. The contoured field depicts the OLR anomaly field but zonally filtered to include only eastward-propagating zonal wavenumbers 1-5, using the method of Hayashi (1981).

Part II

THEORETICAL CONSIDERATIONS FOR THE MJO

Chapter 5

A LINEAR WAVE THEORY FOR THE MJO

5.1 Formulation of the governing equations

In this section we will use the results of Part I to build upon the model of SM in order to construct a dispersion relation that can describe the characteristics of the MJO. We will begin by developing a set of basic equations that can describe convectively-coupled equatorial perturbation. A thorough derivation and scaling of the governing equations is shown in the Appendix and the most important variables and definitions used in this Chapter are summarized in Tables 1 and 2. In deriving these equations we have linearized the field variables into time mean (denoted by an overbar) and perturbation (denoted by a prime) components. The field variables are also truncated meridionally using parabolic cylinder functions $\mathcal{D}_j$ (Majda and Shefter, 2001; Majda and Khouider, 2001; Majda and Stechmann, 2009) and vertically using basis functions (Neelin and Zeng, 2000; Haertel et al., 2008)

$$q(x,y,p,t) = \left\{ \sum_{j=1}^{\infty} \left\{ \bar{q}_j + q'_j(x,t) \right\} \mathcal{D}_j \left(y R_e^{-1} \right) \right\} b(p)$$

where $\bar{q}$ and q' are the mean and anomalous latent energy (specific humidity scaled by the latent heat of vaporization, L_v), respectively, b is the vertical structure function associated with moisture, $R_e = \sqrt{c/(2\beta)}$ is the equatorial Rossby radius of deformation, defined as in Gill (1980), and c is the phase speed of dry Kelvin waves. In order to obtain the simplest wave solution that can resemble the MJO, we will assume that the amplitude of the mean and anomalous q fields decay exponentially with the square of the distance from the equator, and thus their meridional variations can simply be expressed in terms of the zeroth-order

parabolic cylinder function $\mathcal{D}_0(yR_e^{-1}) = \exp\{-y^2/(4R_e^2)\}$

$$q'(x,y,p,t) = q_0'(x,t)\mathcal{D}_0(yR_e^{-1})b(p)$$

Furthermore, the governing equations are vertically integrated in order to simplify them and explicitly represent diabatic heating in terms of observable surface and top of the atmosphere (TOA) variables, as in Kiranmayi and Maloney (2011); Andersen and Kuang (2012); Sobel et al. (2014), among many others. Variables with angle brackets will denote a mass-weighted vertical integral from 100-1000 hPa:

$$\langle b \rangle = \frac{1}{g}\int_{p_T}^{p_s} b dp$$

where $p_T = 100$ hPa and $p_s = 1000$ hPa. From here on the vertically-integrated basis functions will be shown explicitly and variables with primes and overbars will implicitly incorporate the pararabolic cylinder functons $q'(x,y,t) = q_0'(x,t)\mathcal{D}_0(yR_e^{-1})$.

The linearized, truncated, vertically integrated equations for momentum, mass continuity and latent heat (moist static energy) on an equatorial beta (β) plane take the form

$$-\beta y v' + \varepsilon u' = -\frac{\partial \phi'}{\partial x} \tag{5.1a}$$

$$\beta y u' = -\frac{\partial \phi'}{\partial y} \tag{5.1b}$$

$$\varepsilon \phi' + c^2\left(\frac{\partial u'}{\partial x} + \frac{\partial v'}{\partial y}\right) = -\frac{c^2}{\bar{M}_s}\left(P' - R'\right) \tag{5.1c}$$

$$\langle b \rangle \frac{\partial q'}{\partial t} = -\langle F' \rangle - \langle \psi_q'' \rangle - \langle \Lambda b \rangle v' \frac{\partial \bar{q}}{\partial y} - \tilde{M}P' - (1-\tilde{M})R' + E' \tag{5.1d}$$

where ε is a Rayleigh damping coefficient, Λ is the vertical structure function associated with a first internal baroclinic mode (a function exhibiting opposite polarities in the upper and lower troposphere, see Appendix), ϕ' is the anomalous geopotential, $\langle F' \rangle$ is the net

Table 5.1: Basic variables and definitions used in Chapter 5.

Variable	Symbol	Definition	Value/Units
Vertical velocity basis function	Ω	Eq. (B.3)	$\langle\Omega\rangle = 7300\ \delta p/g$ Pa kg m^{-2}
Baroclinic wind/ geopotential basis function	Λ	Eq. (B.4)	$\Lambda(p_s) = 0.28$, $\langle\Lambda\rangle = -28$ kg m^{-2}
Temperature basis function	a	Eq. (B.5)	$\langle a\rangle = 0.41\ \delta p/g$ kg m^{-2}
Moisture basis function	b	Eq. (B.6)	$b(p_s) = 1$, $\langle b\rangle = 0.32\ \delta p/g$ kg m^{-2}
Integrated moisture advection constant	n	$\langle\Lambda b\rangle$	$-0.07\ \delta p/g$ kg m^{-2}
Parabolic cylinder functions	$\mathcal{D}_j$	Eq. (B.1)	
Specific heat of dry air at constant pressure	C_p		1004 J kg $^{-1}$ K^{-1}
Latent heat of vaporization	L_v		2.43 $\times 10^6$ J kg $^{-1}$
Gas constant for dry air	R_d		287 J kg $^{-1}$ K^{-1}
Acceleration due to gravity	g		9.8 m s^{-2}
Depth of the troposphere	δp	$p_s - p_T$	900 hPa
Surface pressure	p_s		1000 hPa
Tropopause-level pressure	p_T		100 hPa
Phase speed of free Kelvin waves in the troposphere	c	Eq. (5.3)	50 m s^{-1}
Free-tropospheric dissipation coefficient	ε		0.30 days^{-1}
Equatorial Rossby radius of deformation	R_e	$\sqrt{c/(2\beta)}$	$\sim$1050 km (10°)
Dissipation length scale of free Kelvin waves	L	c/ε	1.32×10^7 m
Surface mean specific humidity value at y=0	$\bar{q}_0$		$\sim 0.018\ L_v$ J kg^{-1}
Initial moisture perturbation	$\langle b\rangle\hat{q}$		1 L_v J m^{-2}
Convective adjustment timescale	τ_c	Eq. (5.28)	13.7 hours
Moist wave's angular frequency	$\tilde{\omega}$		s^{-1}
Moist wave's zonal wavenumber	k		m^{-1}
Magnitude of wind response to precipitation/heating	$\hat{V}$	$cg/\{\delta p L_v \Lambda(p_s)\}$	8.0×10^{-9} (J m^{-2})$^{-1}$
Magnitude of geopotential response to heating	$\hat{\Phi}$	$c^2 g/\{\delta p L_v \Lambda(p_s)\}$	4.0×10^{-7} m s^{-1} (J m^{-2})$^{-1}$

Table 5.2: Summary of variables and definitions used in Chapter 5.

Variable	Symbol	Definition	Value/Units
Mean gross dry stability	$\bar{M}_s$	$\langle \Omega \partial \bar{S}/\partial p \rangle$	3500 $\delta p/g$ J m^{-2}
Mean gross moisture stratification	$\bar{M}_q$	$\bar{q}\langle \Omega \partial b/\partial p \rangle$	3150 $\delta p/g$ J m^{-2}
Normalized gross moist stability	$\tilde{M}$	$(\bar{M}_s - \bar{M}_q)/\bar{M}_s$	1 - 0.9$\mathcal{D}_0$
Effective gross moist stability	$\tilde{M}_{eff}$	$\tilde{M}(1+r) - r$	
Total effective gross moist stability	$\tilde{M}^*_{tot}$	See Eq. (5.22)	See Fig. 5.11
Precipitation anomaly	P'	$\langle b \rangle q' \tau_c^{-1}$	W m^{-2}
Longwave radiative heating anomaly	R'	$-rP'$	W m^{-2}
Latent heat flux anomaly	E'	$C_u u'$	W m^{-2}
Greenhouse enhancement parameter	r	$r_0 e^{-L_r k}$	See Fig. 5.8
Constants in r calculation	r_0, L_r		0.21, 243 km
Moistening from frictionally-driven ascent	$\langle F' \rangle$	$nu'\bar{q}^*_z$	W m^{-2}
Moistening from modulation of high frequency eddies	$\langle \psi''_q \rangle$	$nu'q''_x$	W m^{-2}
Moisture tendency associated with u'	δq_u	Eq. (5.9)	J m^{-3}
Kelvin and Rossby wave moisture advection parameter	A_K, A_R	Eq. (5.19a), (5.19b)	m^{-1}
Total moisture advection parameter	A_{KR}	$A_K + A_R$	m^{-1}
Kelvin and Rossby Rayleigh damping weight function	$\tilde{p}_K$, $\tilde{p}_R$	Eqs. (5.20a), (5.20b)	
Kelvin and Rossby wave energy damping weight function	$\tilde{g}_K$, $\tilde{g}_R$	Eqs. (5.24a), (5.24b)	
MJO's mean timescale	$\bar{\tau}$		44 days
MJO's mean zonal wavenumber	$\bar{k}$		1.81 $\times 2\pi/(4 \times 10^7)$ m^{-1}
MJO's mean phase speed	$\bar{c_p}$		5.8 m s^{-1}
MJO's mean group velocity	$\bar{c_g}$		-2.3 m s^{-1}
MJO's mean moisture advection parameter	$\bar{A}_{KR}$		34.7 $\times 10^{-9}$ m^{-1}
MJO's mean phase angle between zonal wind and moisture	$\bar{\alpha}$		$\sim 66^\circ$

moistening associated with ascent forced by frictionally-driven boundary layer convergence and $\langle \psi_q'' \rangle = \langle \Lambda b \rangle (\mathbf{V}'' \cdot \nabla q'')'$ is the net moistening associated with the horizontal moisture advection by MJO-related high-frequency eddy activity. P', R' and E' are the anomalous precipitation, longwave radiation and surface latent heat flux expressed in units of W m^{-2}. $\tilde{M}$ is the normalized gross moist stability (Neelin and Held 1987, see also Raymond et al. 2009 for a review on gross moist stability), defined as

$$\tilde{M} = \frac{\bar{M}_s - \bar{M}_q}{\bar{M}_s} \tag{5.2a}$$

where $\bar{M}_s$ and $\bar{M}_q$ are the mean gross dry stability and the gross moisture stratification, respectively, defined as

$$\bar{M}_s = -\left\langle \Omega \frac{\partial \bar{S}}{\partial p} \right\rangle \tag{5.2b}$$

$$\bar{M}_q = \left\langle \Omega \frac{\partial b}{\partial p} \right\rangle \bar{q}_0 \mathcal{D}_0 = \bar{M}_{q0} \mathcal{D}_0 \tag{5.2c}$$

where $\bar{S} = C_p \bar{T} + \bar{\phi}$ is the mean dry static energy, assumed constant, and Ω is a structure function associated with deep convective ascent. In this framework, c is expressed as in Sugiyama (2009a):

$$c = \left(\frac{R_d \bar{M}_s}{C_p \langle a \rangle} \right)^{\frac{1}{2}} = \sqrt{g h_e} \tag{5.3}$$

where R_d is the dry gas constant C_p is the specific heat of air at constant pressure, and a is the basis function for temperature. For $\bar{M}_s = 3.2 \times 10^7$ J m^{-2} and $\langle a \rangle \approx 3740$ kg m^{-2}, values similar to those used by Neelin and Zeng (2000) and Sugiyama (2009a) (scaled by $\delta p/g$, δp = 900 hPa), $c \approx 50$ m s^{-1}, a value similar to those obtained by Bantzer and Wallace (1996) and Milliff and Madden (1996), which yields an equivalent depth value of $h_e \approx 250$ m.

It is worth noting that Eqs. (5.1a)−(5.1c) are the dimensional, modal forms of equations 2.6-2.8 in Gill (1980) which correspond to the steady-state wave response of u', v', and ϕ' to an equatorial heat source $P' - R'$. In this case, however, Eqs. (5.1a)-(5.1c) are coupled to a prognostic moisture equation (Eq. 5.1d) which determines the evolution of the heat

source. Therefore, as in SM, the momentum and mass fields are in quasi-equilibrium with the heating at all instances, making Eq. (5.1) a two-dimensional version of SM's governing equation. In the absence of a heat source, Eqs. (5.1a)−(5.1c) decouple from Eq. (5.1d). If ε is also neglected and the temporal tendencies in u', v' and ϕ' are included, then Eq. (5.1) would yield the free wave solutions of Matsuno (1966).

5.2 Derivation of a single moisture wave equation

In order to obtain a simple linear moisture equation that can describe the MJO, some of the terms in Eq. (5.1d) need to be parameterized in a simple manner. The term in the q' budget that corresponds to moistening by frictionally-induced moisture convergence F' was shown by Adames and Wallace (2014b) to be associated with the second EOF in the vertical velocity profile, which indicates whether the profile of vertical velocity is shallow or elevated. This second baroclinic mode is in turn associated with the difference in divergence between the boundary layer and the free troposphere, which is coupled to u' through wave-induced shallow meridional circulations (Figs. 3, 7 and 12 of Adames and Wallace 2014b) where regions of equatorial easterlies to the east of the strongest convection induces shallow ascent and moistening, while frictional divergence induces low-level descent and drying (see also Benedict and Randall 2007; Liu and Wang 2012; Hsu and Li 2012). Hence, the equation for F' can be approximated in terms of u' using the following relation:

$$\langle F' \rangle \approx \langle \Lambda b \rangle \bar{q}_z^* u' \tag{5.4a}$$

where

$$\bar{q}_z^* = \delta \tilde{M}_u \bar{q}_0 \mathcal{D}_0 \tau_c^{-1} \tag{5.4b}$$

where τ_c is the convective adjustment timescale (Manabe and Strickler, 1964), assumed to be constant in this study.

In defining F', we introduce an effective vertical moisture gradient $\bar{q}_z^*$ corresponding to the net moistening due to frictional convergence, recognizing the fact that much of the moisture

that is advected upward condenses into cloud liquid water, so that only a fraction of the vertically advected moisture contributes to the moisture tendency. We define $\bar{q}_z^*$ as a function of the mean moisture $\bar{q}$ and $\delta\tilde{M}_u$, a parameter corresponding to the amount $\tilde{M}$ would be reduced by wave-induced boundary-layer convergence. $\delta\tilde{M}_u$ is dimensionally expressed as the change in $\tilde{M}$ per m s^{-1} change in u'. F' is identical to the frictional convergence term in Eq. (12) of SM except the terms have been expressed differently. Condensation from frictionally-driven ascent also modulates the horizontal and vertical structure of diabatic heating, but for the sake of keeping the analysis linear it will be assumed that its contribution is negligible compared to $\tilde{M}P'$.

As discussed in SM, there is evidence that the low-level zonal wind anomalies in the MJO modulate synoptic-scale high frequency eddy activity (Maloney and Dickinson, 2003; Maloney, 2009; Andersen and Kuang, 2012), which results in anomalous moistening in regions of easterlies, and drying in regions of westerlies. We can approximate this moistening process through the following relation

$$\langle \psi_q'' \rangle \approx \langle \Lambda b \rangle q_x'' u' \tag{5.5}$$

where q_x'' is a parameter that indicates the amount of eddy moistening per m s^{-1} change in u', and can be thought as an effective zonal moisture gradient imparted by the modulated eddy activity.

The term involving surface latent heat fluxes is expressed as in SM, in terms of the u' by assuming that fluctuations in the wind field dominate the surface latent heat flux anomalies

$$E' \approx C_u u' \tag{5.6}$$

where C_u is a bulk formula for latent heat fluxes, whose sign depends on the nature of the mean flow (negative for $\bar{u} < 0$, positive for $\bar{u} > 0$).

The longwave radiative cooling term is expressed in terms of P' through the following relation

$$R' = -rP' \tag{5.7}$$

where r is the greenhouse enhancement parameter (Kim et al. 2015, also known as the cloud-radiative feedback parameter), which describes the amount of suppressed OLR per unit of precipitation arising from the presence of anomalous water vapor and upper level cloudiness.

With the aforementioned approximations, we can write the latent heat equation as follows

$$\langle b \rangle \frac{\partial q'}{\partial t} = -u' \delta q_u - n v' \frac{\partial \bar{q}}{\partial y} - \tilde{M}_{eff} P' \tag{5.8}$$

where $\tilde{M}_{eff} = \tilde{M}(1+r) - r$ is the effective gross moist stability, $n = \langle \Lambda b \rangle$, and

$$\delta q_u = n \bar{q}_z^* + n q_x'' - C_u \tag{5.9}$$

is the sum of all the moistening processes associated with the zonal wind anomalies. Note that δq_u is analogous to the $C_u - D$ term Eq. (17) of Sobel and Maloney (2013).

We will now proceed to write the terms of the right hand side of Eq. (5.8) in terms of q', and seek a solution in the form of a wave.

$$q_0'(x,t) = \hat{q} e^{i(kx - \tilde{\omega} t)} \tag{5.10}$$

where $\hat{q}$ is a constant defining the amplitude of the initial moisture perturbation, k is the zonal wavenumber and $\tilde{\omega}$ is the angular frequency (a tilde is used to distinguish it from the pressure velocity ω). The anomalous precipitation P' is expressed as in SM

$$P' = \langle b \rangle q' \tau_c^{-1} \tag{5.11}$$

In observations, P is an exponential function of $\langle q \rangle$ (Bretherton et al., 2004; Raymond et al., 2007; Holloway and Neelin, 2009), but is approximated as linear here, which is justifiable provided that the q perturbations are small.

Because the heating fields P' and R' decay exponentially with distance squared from the equator (arising from $\mathcal{D}_0$), we can solve Eqs. (5.1a)$-$(5.1c) to obtain expressions for u' and

v' in the form of Kelvin and n=1 equatorial Rossby wave responses to $P' - R'$, which can be expressed as follows

$$u' = \langle b \rangle \left(\Gamma_{uK} + \Gamma_{uR} \right) q' \tau_c^{-1} \tag{5.12a}$$

$$v' = \langle b \rangle \Gamma_{vR} q' \tau_c^{-1} \tag{5.12b}$$

where Γ is a complex function that describes the horizontal structure of the the Matsuno-Gill response to an equatorially-trapped heat source (expressed in terms of q') for each field, and the subscripts K and R denote the Kelvin and Rossby wave components, respectively.

$$\Gamma_{uK}(k) = -\hat{V}(1+r)\frac{L^{-1} - ik}{L^{-2} + k^2} \tag{5.13a}$$

$$\Gamma_{uR}(k) = \hat{V}(1+r)(3 - y^2 R_e^{-2})\frac{3L^{-1} + ik}{9L^{-2} + k^2} \tag{5.13b}$$

$$\Gamma_{vR}(k) = 8\hat{V}(1+r)y\left(\frac{1}{3} - L^{-1}\frac{3L^{-1} + ik}{9L^{-2} + k^2}\right) \tag{5.13c}$$

where $\hat{V}$ is a dimensional constant and the length scale L is the distance that free Kelvin waves travel in the presence of Rayleigh damping in the free troposphere $L = c/\varepsilon$. Further details on how these structures are obtained, as well as the solution for ϕ' can be found in the Appendix.

Substituting the aforementioned terms, we can write the latent energy anomaly equation (Eq. 5.8) in the following form

$$\tau_c \frac{\partial q'}{\partial t} = -q' \left\{ \delta q_u \left(\Gamma_{uK} + \Gamma_{uR} \right) + n \frac{\partial \bar{q}}{\partial y} \Gamma_{vR} + \tilde{M}_{eff} \right\} \tag{5.14}$$

We will complete the meridional truncation of the moisture equation by projecting it onto the zeroth order parabolic cylinder function $\mathcal{D}_0$, following the notation of Majda and Shefter (2001)

$$\mathrm{Proj}_{\mathcal{D}_0} \left\{ f(x,y,t) \right\} = \int_{-\infty}^{\infty} f(x,y,t) \mathcal{D}_0(y R_e^{-1}) dy \tag{5.15}$$

where we will express $\Gamma_{uR} = (3 - y^2 R_e^{-2})\Gamma'_{uR}$, and $\Gamma_{vR} = y\Gamma'_{vR}$ in order to make their meridional dependence explicit.

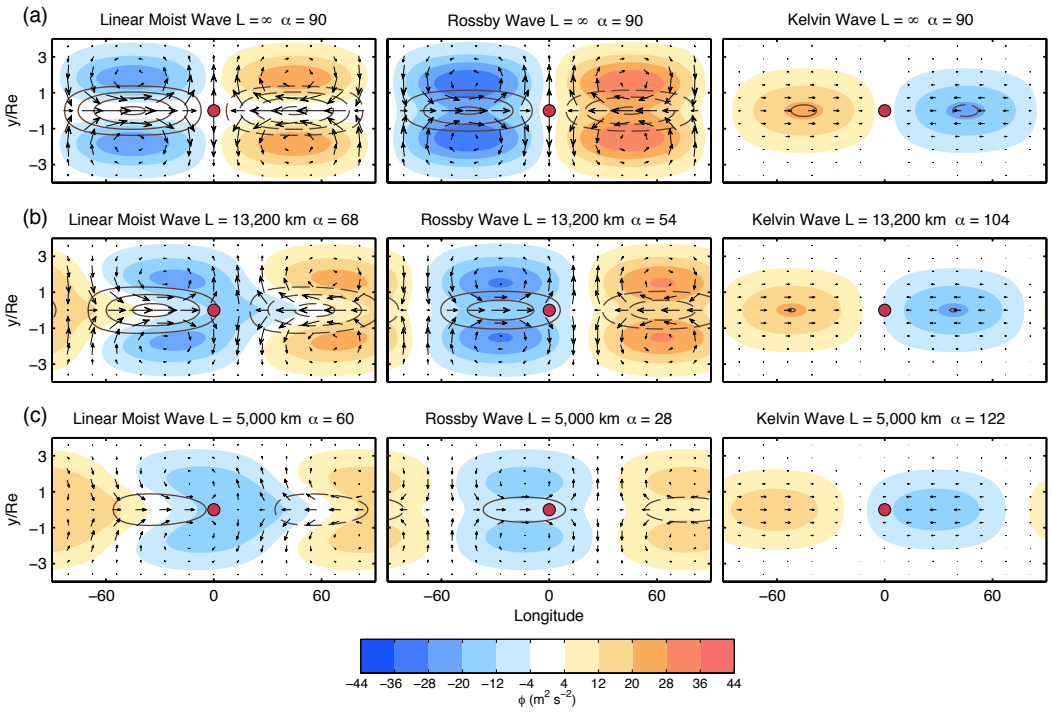

Figure 5.1: Horizontal structure of a zonal wavenumber 2 (left column) linear moist wave (as derived in Chapter 5.1), its Rossby wave contribution (middle column) and Kelvin wave contribution (right column), for values of the dissipation lengthscale L of (a) ∞ , (b) 13,200 km and (c) 5,000 km. ϕ' is shown as the shaded field, u' is contoured and the horizontal wind field $\mathbf{V}'$ is shown as arrows. Contour interval 0.75 m s^{-1}. The largest arrows correspond to wind anomalies of $\sim$1.6 m s^{-1}. Magnitudes corresponds to an initial moisture perturbation of $\langle b \rangle \hat{q} = 1 L_v$ J m^{-2} and $r = 0.2$. The red circle depics the region where q' is a maximum. The wind and ϕ anomalies are scaled to a surface value of Λ.

5.3 The linear moist wave's dispersion relation

By assuming that q' has a solution in the form of a zonally-propagating wave (Eq. 5.10), we obtain the following dispersion relation for the moisture equation projected onto $\mathcal{D}_0$ using

Eq. (5.15)

$$\tilde{\omega} = -\frac{i}{\tau_c}\left\{\frac{\sqrt{2}}{2}(\Gamma_{uK} + 2\Gamma'_{uR})\delta q_u - \frac{\sqrt{2}}{4}n\Gamma'_{vR}\bar{q}_0 + \tilde{M}^*_{eff}\right\} \tag{5.16}$$

where

$$\tilde{M}^*_{eff} = 1 - \frac{\sqrt{2}\bar{M}_{q0}}{2\bar{M}_s}(1+r) \tag{5.17}$$

is the projected effective gross moist stability. As noted by SM, this dispersion relation is complex and only the terms involving Γ_{uK}, Γ_{uR} and Γ_{vR}, which arise from the horizontal wind field through Eq. (5.12) can be real and determine the propagation of the moist wave, while the other terms determine the growth and dissipation. Separating the dispersion relation into its real and imaginary parts yields the following

$$\mathrm{Re}(\tilde{\omega}) = \frac{1}{\tau_c k}\left(\tilde{p}_K A_K + \tilde{p}_R A_R\right) \tag{5.18a}$$

$$\mathrm{Im}(\tilde{\omega}) = -\frac{1}{\tau_c}\left(\frac{\tilde{p}_K A_K}{k\tan\alpha_K} + \frac{\tilde{p}_R A_R}{k\tan\alpha_R} + \tilde{M}^*_{tot}\right) \tag{5.18b}$$

The real component of the dispersion relation is solely due to the Kelvin and Rossby waves inducing moistening and drying by horizontal and vertical moisture advection and modulating the mean surface latent heat fluxes and high-frequency eddy activity. We define this induced moistening/drying as

$$A_K = \frac{\sqrt{2}}{2}\delta q_u \hat{V}(1+r) \tag{5.19a}$$

$$A_R = \sqrt{2}\left(\delta q_u + 2n\bar{q}_0 L^{-1}\right)\hat{V}(1+r) \tag{5.19b}$$

which have units of m^{-1}, and can be thought of as the Kelvin (A_K) and Rossby wave (A_R) "*moisture advection parameters*": the rate at which the anomalous winds per unit of heating increase or decrease the amount of column-integrated moisture. The terms $\tilde{p}_K$ and $\tilde{p}_R$ are weighting functions of value ≤ 1 that account for the damping effect of free-tropospheric

dissipation on the Kelvin and Rossby wave-related wind fields.

$$\tilde{p}_K(k) = \frac{k^2}{L^{-2} + k^2} \tag{5.20a}$$

$$\tilde{p}_R(k) = \frac{k^2}{9L^{-2} + k^2} \tag{5.20b}$$

The difference between the two weights results from Rossby waves being damped at three times the rate in which Kelvin waves are damped, hence the factor of 9 in the denominator of $\tilde{p}_R$. We also define the phase angle α of the zonal winds in the Kelvin and Rossby waves with respect to q':

$$\tan \alpha_K = \frac{\mathrm{Im}(\Gamma_{uK})}{\mathrm{Re}(\Gamma_{uK})} = -\frac{k}{L^{-1}} \tag{5.21a}$$

$$\tan \alpha_R = \frac{\mathrm{Im}(\Gamma_{uR})}{\mathrm{Re}(\Gamma_{uR})} = \frac{k}{3L^{-1}} \tag{5.21b}$$

Finally, we have defined $\tilde{M}^*_{tot}$ as the projected *total effective gross moist stability*, since advection of mean moisture by the "Sverdrup" component of the anomalous meridional winds acts to destabilize the moist region

$$\tilde{M}^*_{tot} = \tilde{M}^*_{eff} - \frac{2\sqrt{2}}{3}\hat{V}n\bar{q}_0\,(1+r) \tag{5.22}$$

We can obtain the real phase speed and group velocity of the moist wave from Eq. (5.18a)

$$c_p = \frac{1}{\tau_c k^2}\left(\tilde{p}_K A_K + \tilde{p}_R A_R\right) \tag{5.23a}$$

$$c_g = -\frac{1}{\tau_c k^2}\left(\tilde{g}_K A_K + \tilde{g}_R A_R\right) \tag{5.23b}$$

where $\tilde{g}_K$ and $\tilde{g}_R$ are weighting functions similar to $\tilde{p}_K$ and $\tilde{p}_R$, which account for the damping effects of free-tropospheric dissipation on the propagation of wave energy in the Kelvin and Rossby waves, respectively

$$\tilde{g}_K(k) = \frac{k^2(k^2 - L^{-2})}{(L^{-2} + k^2)^2} \tag{5.24a}$$

$$\tilde{g}_R(k) = \frac{k^2(k^2 - 9L^{-2})}{(9L^{-2} + k^2)^2} \tag{5.24b}$$

5.4 The moist wave in the limit $L \to \infty$

The derived equations for the moist wave's dispersion in Eqs. (5.18)−(5.24) contain many terms that depend on the dissipation length scale L, which shapes the horizontal wind field. The impact of L in the moist wave's dispersion relation can be further understood after analyzing the wave's propagation characteristics in the absence of any free-tropospheric dissipation. In this limit the dispersion relation simplifies to

$$\mathrm{Re}(\tilde{\omega}) = \frac{A_{KR}}{\tau_c k} \tag{5.25a}$$

$$\mathrm{Im}(\tilde{\omega}) = -\frac{\tilde{M}^*_{tot}}{\tau_c} \tag{5.25b}$$

where $A_{KR} = A_K + A_R$ is the combined contribution from Kelvin and Rossby waves to propagation. The horizontal structure of the moist wave and the individual Kelvin and Rossby wave components is shown in row (a) of Fig. 5.1, the structure of the terms that lead to growth and eastward propagation are shown in Fig. 5.2. The relative contribution of the shaded terms in Fig. 5.2 are chosen so that they are qualitatively consistent with the results of Andersen and Kuang (2012); Kim et al. (2014); Adames and Wallace (2015), among others. In the absence of any free-tropospheric damping, the linear moist wave will exhibit the following properties:

1. The phase speed of the disturbance depends upon its wavelength, the moisture advection parameter A_{KR}, and the convective timescale τ_c. Larger values of A_{KR} will result in faster eastward propagation while larger values of k (shorter wavelengths) and τ_c result in a slower phase speed.

2. Only a negative total effective gross moist stability $\tilde{M}^*_{tot}$ can lead to growth of the wave disturbance. If $\tilde{M}^*_{tot} = 0$ then moisture is conserved following the wave since the

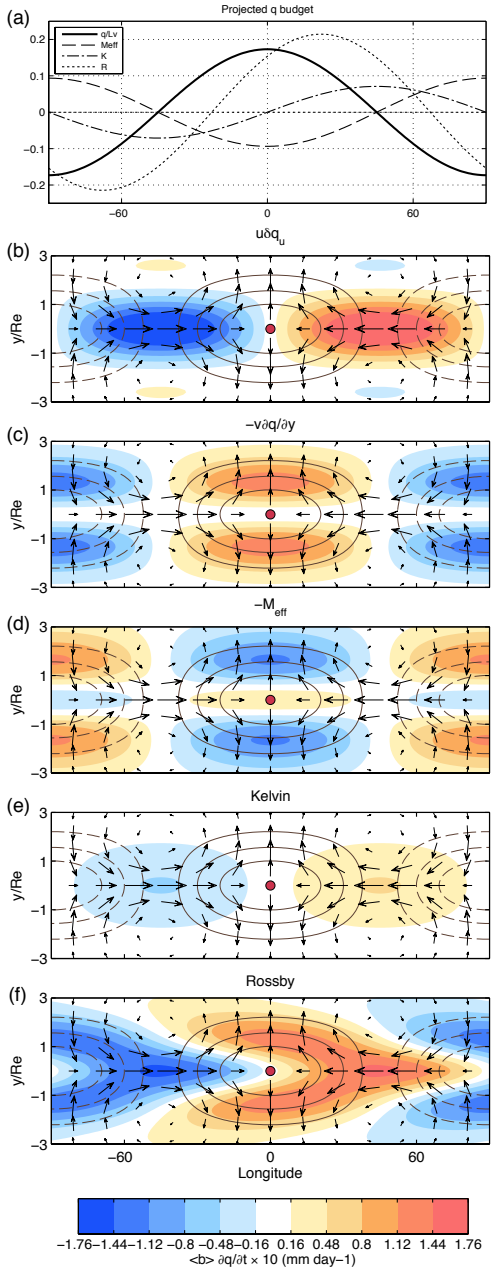

Figure 5.2: Propagation of the linear zonal wavenumber 2 moist wave solution for $L \to \infty$: (a) Moisture anomalies after using the projection operator (Eq. 5.15) (solid line), contribution from effective gross moist stability $\tilde{M}_{eff}$ to the moisture tendency (dashed line), and the Kelvin (dot-dash line) and Rossby (dotted line) wave contributions to the moisture tendency. Panels (b)-(f) show horizontal maps of the contribution of (b) moistening by the zonal flow, where $nq''_x = 3$ J m^{-3}, $C_u = -3$ J m^{-3} and $nq^*_z = 4.5\mathcal{D}_0$ J m^{-3}, (c) meridional moisture advection, (d) effective gross moist stability, (e) Kelvin wave and (f) Rossby wave to the moisture tendency. $\langle b \rangle q'$ is contoured in all panels. Contour interval $0.25L_v$ J m^{-2}. The horizontal wind field $\mathbf{V}'$ is shown as arrows. The largest arrows correspond to wind anomalies of $\sim$1.6 m s^{-1}. The wind and ϕ anomalies are scaled to a surface value of Λ.

meridional and vertical advection of moisture balances precipitation.

3. Because $\tilde{M}_{eff}$ changes polarity poleward of $1R_e$, it is the meridional advection of moisture by v' which reduces $\tilde{M}^*_{tot}$ poleward of $1R_e$, increasing moisture in this region. Thus meridional moisture advection can be thought of as widening the anomalous moist region, as suggested by Adames and Wallace (2015).

4. The wave is dispersive. In the limit $L^{-1} \to 0$, assuming $A_{KR} \neq 0$, the wave exhibits a group velocity that is equal and opposite to its phase speed, $c_g = -c_p$.

5. Moistening by the anomalous winds is dominated by the Rossby wave contribution, as seen in Figs. 5.2a, e and f. This dominance is due to the u' in the Rossby waves being 3 times stronger than in the Kelvin waves and v' being completely due to Rossby waves.

These properties account for some aspects of the observed and simulated MJO. Studies in which the MJO's background state is modulated (Arnold et al., 2013; Kang et al., 2013; Arnold et al., 2015), have suggested that increasing A_{KR} by increasing the horizontal and vertical moisture gradients results in faster MJO propagation, consistent with bullet (i). Many studies have shown the importance of a negative $\tilde{M}^*_{tot}$ in destabilizing of the MJO (Hu and Randall, 1994; Sobel and Gildor, 2003; Kim et al., 2011; Benedict et al., 2014), supporting bullet (ii). However, little evidence has been presented showing that the MJO is a dispersive wave with a westward group velocity. The dispersive properties of the MJO are documented in the next section and the relevance of points (iv)-(vi) to the observed MJO are discussed in Chapters 5.5 and 5.6.

5.5 Further evidence that the MJO is a dispersive wave

Hints of a group velocity in the MJO were shown in Part I. This westward group velocity is apparent in time-longitude sections of individual events, without the need for compositing.

Figure 5.3 shows a selection of sections for the 20-100 day filtered and MJO filtered (using the Hayashi 1981 method) OLR anomalies. The sequences shown in each column correspond to the three strongest events that occurred in three separate geographical regions, defined as the Indian Ocean (60°-100°E, 15°N/S), the Maritime Continent (100°-140°E, 15°N/S), and the western Pacific (140°-180°E, 15°N/S). In many of these sequences, the waves tend to be arranged in westward-migrating packets. The first wave in the packet is first discernible near or to the east of the Maritime Continent, between 120°E and the Date Line, and successive waves develop farther and farther toward the west. The behavior is analogous to the eastward dispersion of midlatitude Rossby waves (Chang, 1993) and the behavior of dispersive equatorially-trapped waves such as the Mixed Rossby-gravity and inertio-gravity modes (see Wheeler et al. 2000 Figs. 12, 16 and 20).

To further elucidate the westward migration of the MJO-related anomalies, lag regression analysis based on the time series of OLR anomalies for the three aforementioned sectors was performed on OLR, GPCP precipitation (P'), SSM/I-TMI precipitable water ($\langle q' \rangle$), and ERA-Interim 300 hPa vertical velocity (ω'). Time-longitude diagrams of the regressed fields are shown in Fig. 5.4. Westward-migrating wave packets are clearly evident as in Fig. 5.3. The group velocity is within the range -1.8 to -3 m s^{-1}, and all fields exhibit phase speeds within 5 or 6 m s^{-1}. The group velocity to phase speed ratio c_g/c_p for these four fields ranges between -0.3 and -0.5. The time-longitude diagrams of Knutson and Weickmann (1987); Hendon and Salby (1994); Wheeler and Kiladis (1999); Roundy and Frank (2004); Kiladis et al. (2005); Straub (2013), and Kim et al. (2014) also show a westward migration of the extrema in the MJO-related anomaly fields, similar to that in these twelve panels. Thus, a westward group velocity in the MJO can be seen in several individual events, and regressions based on different MJO indices.

5.6 The linear moist wave in relation to MJO structure and propagation

In Chapters 5.1-5.4 we derived a linear wave solution for a linear moist wave whose propagation is determined by the anomalous wind field in the Matsuno-Gill wave response to an

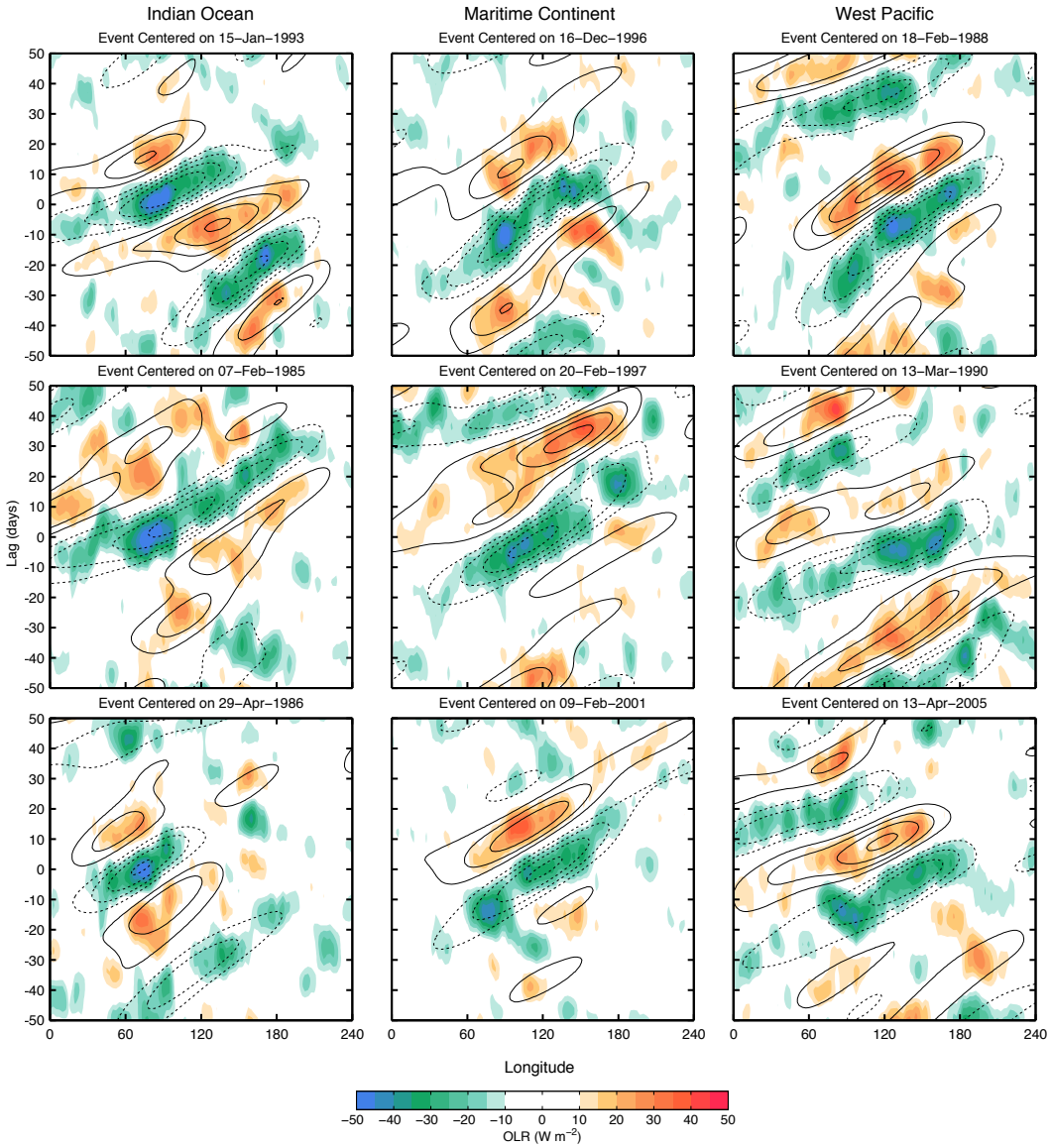

Figure 5.3: Time-longitude sections of MJO events for 20-100 day filtered OLR (shaded) and MJO-filtered OLR (contoured). The left column corresponds to the 3 strongest events for OLR anomalies averaged over the Indian Ocean Sector (60−100°E, 15°N/S averaged), the middle column corresponds to the 3 strongest events over Maritime Continent Sector (100−140°E, 15°N/S) that do not overlap with Indian Ocean events, and the right column corresponds to the 3 strongest events over the Western Pacific sector (140−180°E, 15°N/S) that do not overlap with the other two sectors. The reference time (lag day 0) corresponds to the date in the diagram's title. Contour interval 7.5 W m^{-2}.

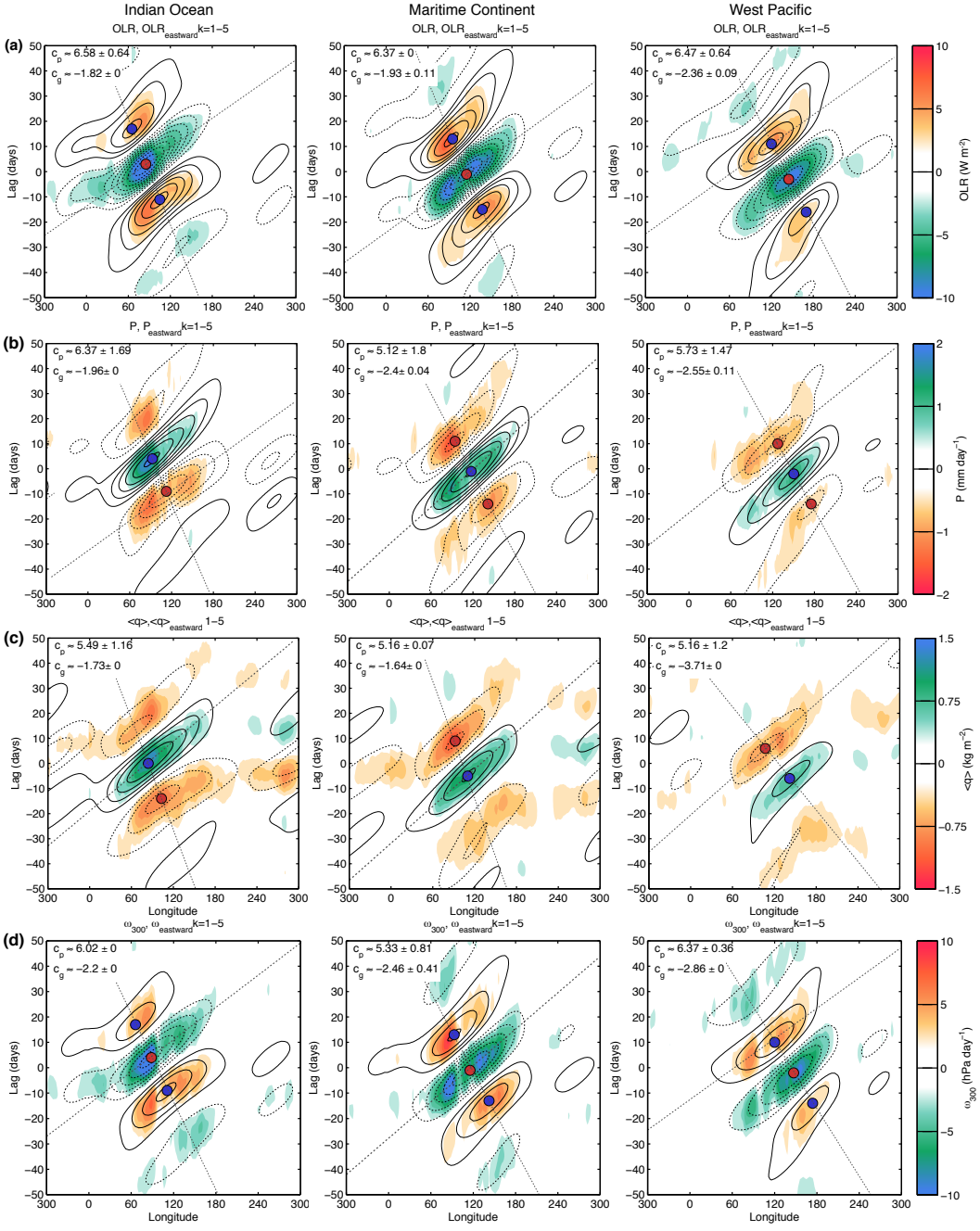

Figure 5.4: Time-longitude sections of filtered (shaded) and MJO-filtered (contoured) (*a*) OLR, (*b*) GPCP precipitation, (*c*) SSM/I-TMI precipitable water and (*d*) ERA-Interim 300 hPa vertical motion. The rows correspond to OLR anomalies that peak in the Indian Ocean sector (left row), Maritime Continent (middle row) and West Pacific (right row). The reference time (day 0) corresponds to the time when the MJO-filtered OLR anomalies are a minimum. The gray dashed lines are linear least-square fit estimates of the phase speed and group velocity for each field, and the circles represent a local extremum in the MJO-filtered field. The values of the calculated phase speeds and group velocities, along with their uncertainties, are shown in the top left corner of each panel.

equatorial heat source. In the previous section we showed observational evidence that the MJO is characterized by a dispersion relation in which the phase speed is eastward and the group velocity westward, consistent with the linear moist wave solution derived in Chapters 5.1-5.4. In this section, we will compare this model with the observed MJO. In order to make this comparison, however, a value for the dissipation length scale L and the convective adjustment timescale τ_c needs to be estimated.

5.6.1 Estimation of the dissipation length scale L in the tropical free troposphere and the convective adjustment timescale τ_c

For free-tropospheric motions, L depends on the phase speed of free Kelvin waves and on the dissipation timescale ($\tau_\varepsilon = \varepsilon^{-1}$). τ_ε is not a variable that can easily be measured with direct observations. The large uncertainty is reflected in the values ranging from 1 to 20 days that have been used in previous studies (Neelin et al., 1987; Seager, 1991; Lee et al., 2009). We can estimate a value of L from Eq. (5.23), by approximating the relative contribution of Kelvin (A_K) and Rossby waves (A_R) to propagation, and using the approximated group velocity to phase speed ratio implied by Fig. 5.4, which is

$$\frac{\bar{c_g}}{\bar{c_p}} \approx -0.40 \pm 0.12 \tag{5.26}$$

for an MJO with an effective horizontal wavenumber $\bar{k}$. In order to estimate $\bar{k}$, we perform a spectral analysis in longitude for each field in Fig. 5.4, within 10°N/S and for all days within 25 days of the reference time. The power spectrum is then averaged for all the latitudes and days included, and then normalized using the formula $\tilde{P}_{xx}(k) = P_{xx}(k)/\Sigma_{k=1}^{N} P_{xx}(k)$. The approximate wavenumber $\bar{k}$ is obtained by summing the zonal wavenumbers, weighting each one by its normalized power $\tilde{P}_{xx}$, which yields a value of 1.81.

The relative contributions of A_K and A_R to propagation can be inferred from previous observational studies (Kiranmayi and Maloney 2011; Adames and Wallace 2015; among others). These studies have shown that moistening processes related to the zonal wind

anomalies are comparable to those from meridional moisture advection. As such, it can be inferred from Eqs. (5.19a) and (5.19b) that Rossby waves contribute about 4 times more to the propagation of the moist wave than the Kelvin wave does. Substituting the values of $\bar{k}$ onto Eqs. (5.20) and (5.24), and solving Eq. (5.26) for L, noting that $A_R \approx 4A_K$, we obtain

$$L \approx 1.32 \times 10^7 m \tag{5.27}$$

Values of L of 1.18×10^7 m to 1.40×10^7 m can be obtained for values of A_R/A_K ranging from 2.5 to 6, and our results are insensitive to values of L within this range. Our estimated value is nearly an order of magnitude larger than that assumed by SM, which is more appropriate for the boundary layer rather than for the free troposphere. Our estimated value of L is also approximately equivalent to the distance that the Kelvin wave response travels in Fig. 5 of Matthews (2000), where it propagates $\sim$130° of longitude from the Maritime Continent to the coast of South America. For a free Kelvin wave phase speed of $\sim$50 m s^{-1}, we obtain a dissipation timescale of $\sim$3 days. This timescale is longer than the one-day timescale obtained by SM, smaller than the 5-day timescale used by Sugiyama (2009b), and within the range of convective damping timescale for large-scale circulations suggested by Romps (2014).

Another important parameter that needs to be estimated is the convective adjustment timescale τ_c, which in turn determines the magnitude of the phase speed, group velocity and wind-driven damping. τ_c was estimated to be of the order of 12-16 hours by Bretherton et al. (2004), while SM estimated τ_c to be on the order of 2.4 days using the following relationship

$$\tau_c = \frac{\langle \bar{q}_s \rangle}{a_d P_R} \exp\left(-a_d \frac{\langle \bar{q} \rangle}{\langle \bar{q}_s \rangle} \right). \tag{5.28}$$

where $\langle \bar{q}_s \rangle \approx 70 L_v$ J m^{-2} is the saturation column integrated latent energy, and $a_d = 15.6$ and $P_R = 8.22 \times 10^{-5}$ mm day^{-1}. We can estimate τ_c using the same values as in SM but estimating $\langle \bar{q} \rangle$ by averaging the annual-mean SSM/I-TMI PW over the warm pool region

$60° - 180°$E and 10°N/S, which yields a value of τ_c of ≈13.7 hours for a warm pool value of $\langle \bar{q} \rangle$ of ≈ 51.5 L_v J m^{-2}.

5.6.2 An approximate dispersion relation for the observed MJO

We can now obtain an approximate dispersion relation for the moist wave by using the A_R/A_K ratio. Once again defining a total moisture advection parameter $A_{KR} = A_K + A_R$, and noting that $A_{KR} \approx 5A_K$, we can obtain the following:

$$\mathrm{Re}(\tilde{\omega}) = \frac{\tilde{p} A_{KR}}{\tau_c k} \tag{5.29a}$$

$$\mathrm{Im}(\tilde{\omega}) = -\frac{1}{\tau_c}\left(\frac{\tilde{p} A_{KR}}{k \tan\alpha} + \tilde{M}^*_{tot}\right) \tag{5.29b}$$

where an approximate weight function $\tilde{p}$ for the dissipation of the total anomalous wind field takes the following form

$$\tilde{p}(k) = \frac{k^2(13L^{-2} + 5k^2)}{5(9L^{-2} + k^2)(L^{-2} + k^2)} \tag{5.29c}$$

and the phase angle of the combined Kelvin and Rossby wave-related zonal winds

$$\tan\alpha = \frac{(13L^{-2} + 5k^2)k}{(3L^{-2} + 11k^2)L^{-1}}. \tag{5.29d}$$

The simplified phase speed and group velocities take the form:

$$c_p = \frac{\tilde{p} A_{KR}}{\tau_c k^2} \tag{5.30a}$$

$$c_g = -\frac{\tilde{g} A_{KR}}{\tau_c k^2} \tag{5.30b}$$

where $\tilde{g}$ is a weighting function similar to $\tilde{p}$, of the form

$$\tilde{g}(k) = \frac{k^2(5k^6 - 11k^4L^{-2} - 5k^2L^{-4} - 117L^{-6})}{5(9L^{-2} + k^2)^2(L^{-2} + k^2)^2} \tag{5.30c}$$

5.6.3 The phase relationship between wind and moisture

In order to compare whether our moist wave solution, scaled by our estimated value of L, is consistent with the observed MJO, we calculated the zonal phase angle α between u' and q' using Eq (5.29d). The importance of α in the maintenance and propagation of the linear moist wave discussed in SM, but it is worth discussing here in relation to the observed MJO. In an atmosphere with no dissipation $L \to \infty$, Eq (5.29d) would tend to infinity and thus $\alpha = 90°$, which corresponds to u' and q' being in spatial quadrature at the equator, as discussed in Chapter 5.4 and shown in the top panel of Fig. 5.1.

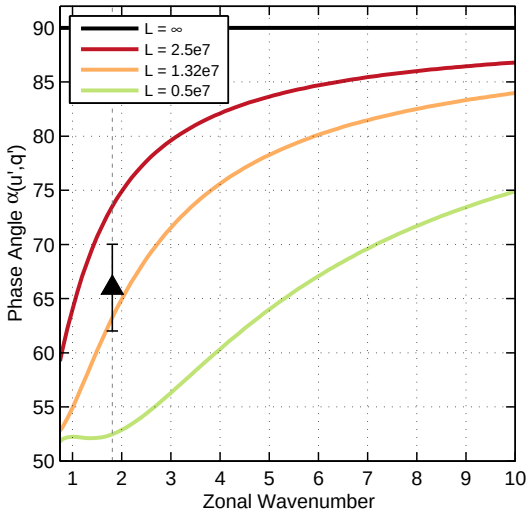

Figure 5.5: Phase angle between u' and q', as obtained from Eq. (5.29d) for values of L of ∞, 25,000 km 13,200 km and 5,000 km. The black triangle corresponds to α as inferred from SSM/I-TMI- precipitable water ($\langle q' \rangle$) and ERA-Interim 850 hPa u' (see text for further details). The 95% confidence interval based on a two-tailed t-test is depicted as an error bar.

As damping is increased, α decreases and the westerly wind anomalies are shifted eastward towards the heat source, as seen in rows (b) and (c) of Fig. 5.1, and shown in Fig. 5.5 for the first ten zonal wavenumbers. This displacement can be interpreted as follows: In the presence of free-tropospheric dissipation, both Rossby and Kelvin wave components influence

u' near the heat source. However, because the Rossby wave is characterized by a stronger zonal wind response (see Eq. C.2a), and exhibit a stronger shift towards the heat source than the Kelvin wave response does, then it follows that it will dominate u' near the heat source, as seen in rows (b) and (c) of Fig. 5.1.

An estimate of α for the observed MJO, $\bar{\alpha}$, indicated as a black triangle in Fig. 5.5, is obtained by calculating the spectral phase angle between ERA-Interim 850 hPa u' and SSM/I-TMI PW ($\langle q' \rangle$), for regressions based on the three sectors presented in Fig. 5.4. The phase angle is obtained by calculating the cross power spectrum in longitude between u' and $\langle q' \rangle$ within 10°N/S and for all days within 25 days of the reference time (Fig. 5.4). The cross spectrum is then averaged for all latitudes and days, and the phase angle is calculated as $\theta(k) = \tan^{-1}[\mathrm{Im}(P_{xy})/\mathrm{Re}(P_{xy})]$. An effective value of $\bar{\alpha}$ for the MJO can be estimated by summing the values of θ for each wavenumber, weighting each one by its normalized power $|\tilde{P}_{xy}(k)| = |P_{xy}(k)|/\Sigma_{k=1}^{N}|P_{xy}(k)|$, which yields a value of $\bar{\alpha}$ of ∼66°. A close correspondence is observed between the value of α from ERA-Interim u' and SSM/I-TMI $\langle q \rangle$ and the linear wave solution for L = 13,200 km. Based on the above discussion, this result indicates that westerlies from the Rossby wave response dominate the region of enhanced moisture and convection in the MJO, as was noted by Rui and Wang (1990); Hendon and Salby (1994); Kiladis et al. (2005); Adames and Wallace (2014b), among many others.

5.6.4 Propagation characteristics of the moist wave

Dissipation in the free troposphere acts to slow down the moist wave by weakening its horizontal wind field, as seen in Fig 5.1. But due to the east/west asymmetry in the wind field arising from the dissipation scale L, the phase speed is reduced much less than the group velocity. This relationship is illustrated graphically in Fig. 5.6 for a moist wave disturbance with a mean moisture advection parameter $\bar{A}_{KR}$ = 34.7 $\times 10^{-9}$ m^{-1} and a convective timescale τ_c of 13.7 hours, as calculated above. The value of $\bar{A}_{KR}$ is obtained through Eq. (5.30), using the inferred values of τ_c and L, the mean phase speed $\bar{c}_p$ estimated from Fig. 5.4, and an effective zonal wavenumber $\bar{k}$.

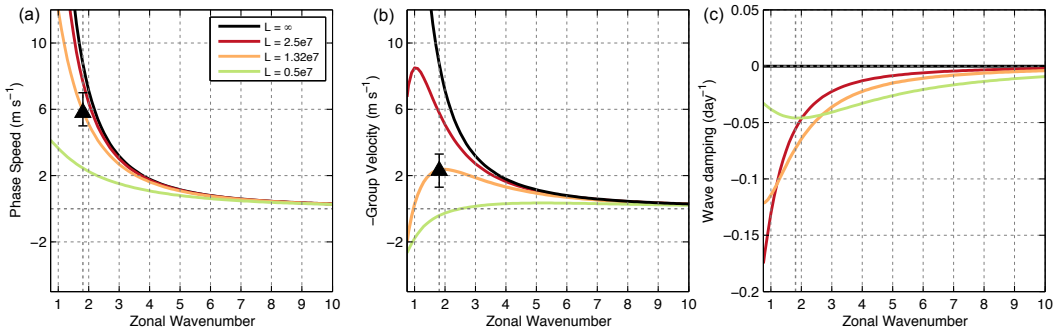

Figure 5.6: (a) Phase speed c_p, (b) group velocity $-c_g$ (the sign has been reversed in order to facilitate comparison with the phase speed), and (c) wave damping obtained from Eq. (5.29) for a linear moist wave with a moisture advection parameter A_{KR} of 34.7 mm km^{-2}, a convective time scale τ_c of 13.7 hours and a dissipation length scale L ranging from ∞, 25,000 km 13,200 km, and 5,000 km. The black triangle corresponds to the mean phase speed $\bar{c}_p$ and group velocity $\bar{c}_g$ inferred from the linear least squares fit in Fig. 5.4 and the error bars correspond to the range of uncertainty in the $\bar{c}_p$ and $\bar{c}_g$ values.

For a free troposphere with no dissipation, a moist wave with $\bar{k} = 1.81$ will be characterized by a phase speed and group velocity of $\sim$8.7 m s^{-1}. Including dissipation with the value of L obtained in Chapter 5.5 decreases the phase speed to $\sim$5.8 m s^{-1} while the group velocity is reduced to -2.3 m s^{-1} (indicated in Fig. 5.6 by a black triangle). However, for the inferred value of L, the phase speed decreases more quickly with increasing k than the group velocity as a result of α increasing with wavenumber. Thus the ratio between phase speed and group velocity is largest at the largest scales. It is worth noticing that, for the inferred value of L, the moist wave's group velocity is $\sim$0 for zonal wavenumber 1, the MJO group velocity inferred by Raymond (2001); Majda and Stechmann (2009), among others, but it is westward for all other zonal wavenumbers.

As discussed by SM, a value of α of less than 90° will lead to damping of the moist wave. This wave-driven damping corresponds to the first term on the right hand side of Eq. (5.29b). Its contribution to the total growth rate is shown in the right panel of Fig. 5.6, from which it is evident that the moist wave would be damped by these wind anomalies at

a rate of $\sim$0.07 day^{-1}, or roughly half the rate in which the anomalous wind field induces eastward propagation ($\bar{c_p}\bar{k} \approx 0.14$ day^{-1}).

In order to further illustrate the propagation mechanism of the moist wave, Fig. 5.7 shows the contribution of Kelvin and Rossby waves to propagation. Compared to the case where $L \to \infty$, the drying anomalies in the Rossby waves (panel c) are shifted eastward towards the heat source. In comparison, the Kelvin wave response is only weakly affected by the increased free-tropospheric damping. Thus it is the Rossby waves that dominate the increase in damping and the changes in phase speed and group velocity that we see for the inferred value of L. Observational evidence by Benedict and Randall (2007); Johnson and Ciesielski (2013); Adames and Wallace (2015) is qualitatively consistent the idea of Rossby waves producing damping within the moist region in the MJO .

5.7 Greenhouse enhancement feedbacks and MJO selection of horizontal scale

Because wind driven processes can only damp an eastward-propagating moist wave, then destabilization can only occur when $\tilde{M}^*_{tot}$ is negative. Additionally, wave-driven damping is strongest at the largest scales, and thus cannot account for the observed scale of the MJO. Thus both growth and scale selection may arise from a scale-dependence in $\tilde{M}^*_{tot}$. In previous studies it has generally been assumed that $\tilde{M}$ and r, and hence $\tilde{M}^*_{tot}$ are scale-independent, and hence have no bearing on the MJO's preferred scale. In this section we will reconsider the validity of this assumption.

The greenhouse enhancement parameter r is obtained from Eq. (5.7). Using the 20-100 day filtered OLR and GPCP rainfall anomaly fields at all points in time within 15°N/S, 60$-$180°E yields a value of r of $\sim$0.17 (top left panel of Fig. 5.8), consistent with the values obtained by Peters and Bretherton (2005), and Bretherton et al. (2005). In order to determine whether r could be zonal wavenumber dependent, we further decompose the 20-100 day filtered OLR and P anomalies into contributions from each zonal wavenumber, without separating them into eastward and westward-propagating components. A value of r is then calculated for each individual wavenumber through linear least squares fit. Scatterplots for

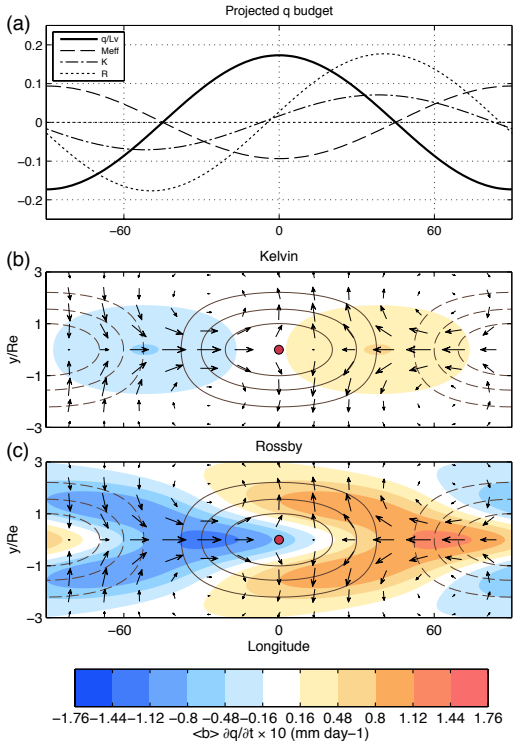

Figure 5.7: As in panels a, e and f of Fig 5.7 but for $L = 13{,}200$ km. Contour interval $0.25L_v$ J m^{-2}. The horizontal wind field $\mathbf{V}'$ is shown as arrows. The largest arrows correspond to wind anomalies of $\sim$1.6 m s^{-1}.

the density distribution of points for $k = 1$ and $k = 4$ is shown in the top panel of Fig. 5.8, for reference. The value of r for all zonal wavenumbers from 1-20 is shown in the bottom panel of Fig. 5.8. It is clear that r decreases as k increases. We can obtain an empirical relation for the k dependence on r through least squares fit, which yields the following relation:

$$r \approx r_0 e^{-L_r k} \tag{5.31}$$

where $r_0 \approx 0.21$ is the value of the greenhouse enhancement parameter for zonal wavenumber zero and $L_r \approx 243$ km is a lengthscale that characterizes the changes of r with k. The above fit has the advantage that r asymptotically approaches zero for large k and has a real value

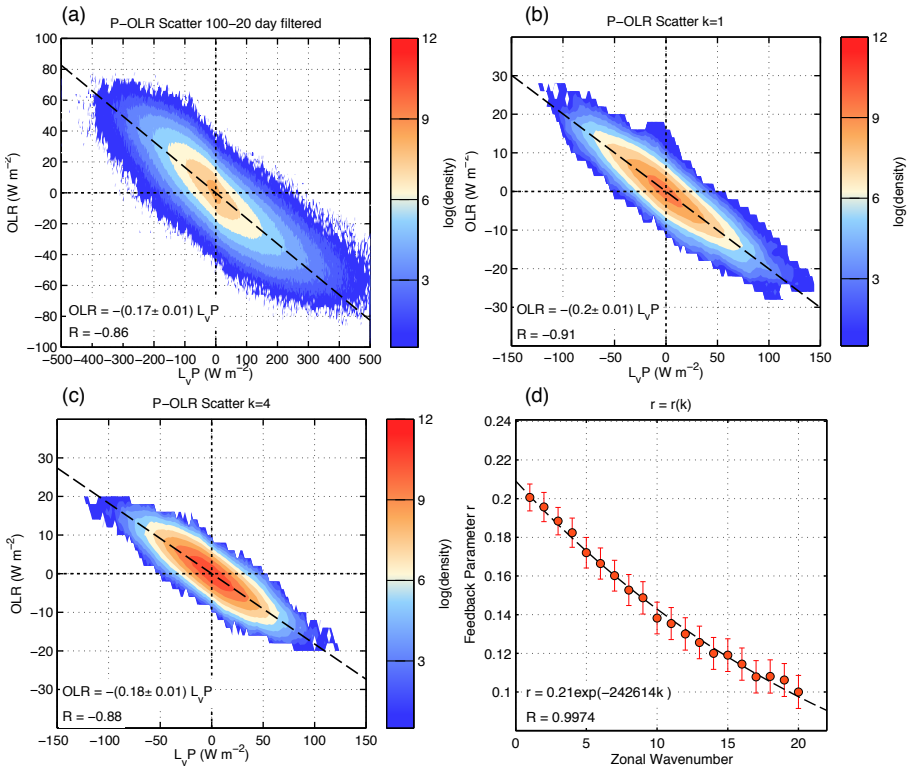

Figure 5.8: (a) Scatterplot of 20-100 day filtered precipitation (in W m^{-2} units) versus OLR anomalies. The shaded field in the scatterplot corresponds to the base 10 logarithm of the number of points located within 2 W m^{-2} $\times$ 2 W m^{-2} bins. The best fit linear regression is depicted as a dashed line, where the slope corresponds to the cloud-radiation feedback parameter r. Panels (b) and (c) are as in (a) but for 20-100 day filtered anomalies decomposed into zonal wavenumber 1 and 4, respectively. (d) Cloud-radiation feedback parameter r as a function of zonal wavenumber k. The best fit regression is depicted as a dashed line. Error bars correspond to the 95% confidence interval. For all plots the best fit regression equation and the correlation coefficient are shown in the bottom left corner.

for $k = 0$. Similar results were obtained for daily anomalies without filtering. A similar analysis was performed to seek a wavenumber dependence on $\tilde{M}$ with ERA-Interim data, but no clear relationship emerged.

A spatial relationship for R' and P' can be obtained by using the inverse Fourier transform

of Eq. (5.31), which has the following form

$$R'(x,y,t) \approx -\frac{r_0 L_r}{\pi} \int \frac{P'(x^*,y,t)}{L_r^2 + (x-x^*)^2} dx^* \tag{5.32}$$

The accuracy of the OLR (R) anomalies estimated through Eqs. (5.31) and (5.32) was verified by comparing them to NOAA OLR anomalies. A robust fit between the observed OLR and R' estimated from Eqs. (5.31) and (5.32) was seen, with a slope that is close to 1 and a correlation coefficient of 0.88 (Fig. 5.9).

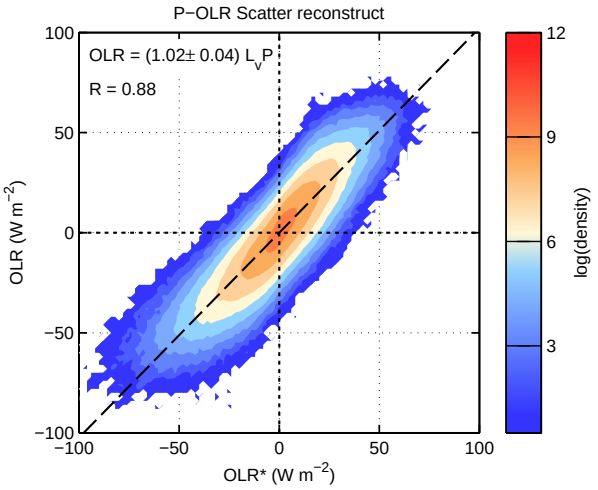

Figure 5.9: (a) Scatterplot of OLR obtained from GPCP 20-100 day filtered precipitation through Eq. (5.32), referred to as OLR* versus 20-100 day filtered OLR anomalies. The shaded field in the scatterplot corresponds to the base 10 logarithm of the number of points located within 2 W m^{-2} $\times$ 2 W m^{-2} bins. The best fit linear regression is depicted as a dashed line.

In order to elucidate the physical mechanism that leads to the observed wavenumber dependency in r, Fig. 5.10a shows an example of the OLR response to a point region of precipitation, as obtained from Eq. (5.32). The OLR response has a shape similar to a gaussian, with the anomaly decaying to half its original magnitude at a distance L_r from the region of precipitation. This shape is likely the result of longwave heating by upper-level

anvil clouds spreading horizontally away from the precipitating region, possibly enhanced by the environmental vertical wind shear (Ackerman et al., 1988; Lin and Mapes, 2004a). For several evenly spaced sources of precipitation (Fig. 5.10*b*), the OLR response is larger in zonal extent but also more than twice the amplitude. This is likely a result of cirrus clouds covering a greater fraction of the sky and forming thicker anvils in regions of aggregated, organized convection, leading to an enhanced greenhouse effect (see Fig. 13 of Ackerman et al. 1988).

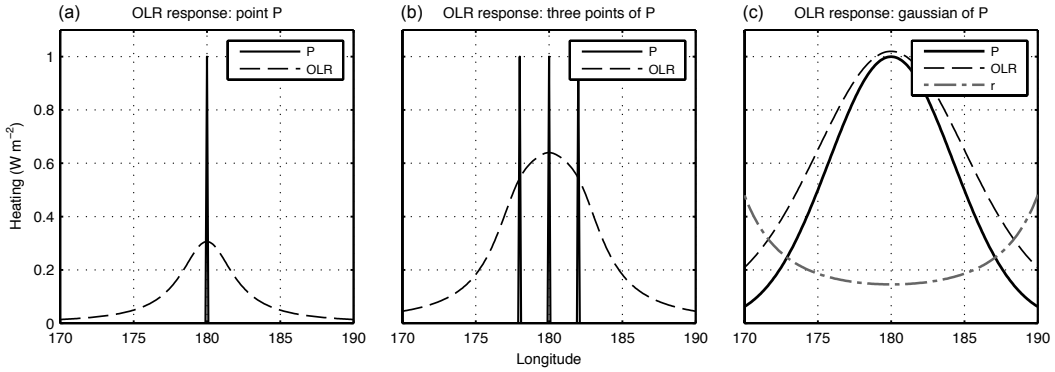

Figure 5.10: (*a*) OLR response (dashed line) to a point source of precipitation (solid line) at 180°, as estimated from Eq. (5.32). (*b*) As in panel (*a*), but for three point sources of precipitation located at 178°,180° and 182°. (*c*) OLR response to a Gaussian distribution of anomalous precipitation. The dot-dash line in this panel corresponds to the greenhouse enhancement parameter $r = R'/P'$. The OLR field has been multiplied by a factor of 100 in panels (*a*) and (*b*), and a factor of 7 in (*c*) in order to facilitate comparison.

Figure 5.10*c* shows the OLR response for a gaussian distribution in anomalous precipitation. Because the magnitude of precipitation decays more quickly with distance from the center of convection than the OLR anomalies diagnosed through Eq. (5.32) do, then regions of weaker precipitation within a convective complex exhibit a larger r, consistent with results from Kim et al. (2015). Their study also found, using 29 climate model simulations, that the greenhouse enhancement parameter in the weak precipitation regime has a robust statistical relationship with the MJO simulation capability of the models.

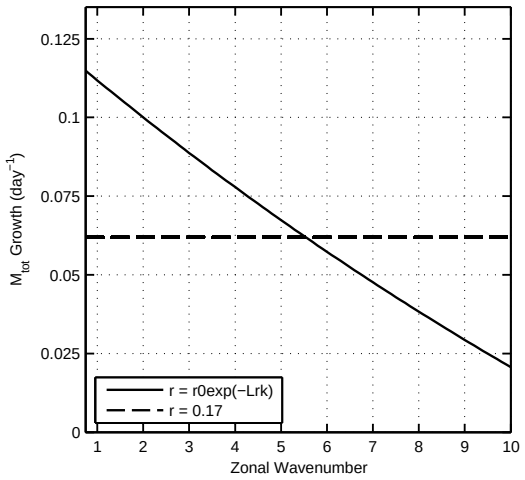

Figure 5.11: Total gross moist stability $\tilde{M}^*_{tot}$, as obtained from Eq. (5.22), as a function of zonal wavenumber k for r determined from Eq. (5.31) (solid line) and $r = 0.17$ (dashed line). Other values used in the calculation of $\tilde{M}^*_{tot}$ are shown in Tables 1 and 2.

The profile of $\tilde{M}^*_{tot}$ with values of r as determined by Eq. (5.31) is shown in Fig. 5.11 together with an $\tilde{M}^*_{tot}$ for a constant value of r of 0.17. With the profile $\tilde{M}^*_{tot}$ obtained from a wavenumber dependent r, zonal wavenumber 1 grows at nearly twice the rate of zonal wavenumber 6, and nearly 5 times the rate of zonal wavenumber 10. Thus, a wavenumber-dependent profile of $\tilde{M}^*_{tot}$ favors the growth of the largest-scale moist waves. It is worth noting that a wavenumber-dependent value of r causes A_{KR} to vary with k, but these variations are small.

Finally, the combined contribution of Rossby wave damping and $\tilde{M}^*_{tot}$ is shown in Fig. 5.12 as a function of k and A_{KR}. For the lowest values of A_{KR} considered, wind-driven damping is weak and the growth rate favors the development of moist waves with the largest zonal scales. As A_{KR} increases, so does the contribution from wind-driven damping to the growth rate and wavenumber 1 becomes unfavorable. For larger values of A_{KR} (upper right corner of Fig. 5.12), roughly corresponding to periods of 20-30 days, wind-driven damping favors the development of smaller-scale moist waves of zonal wavenumber 5 and larger, which

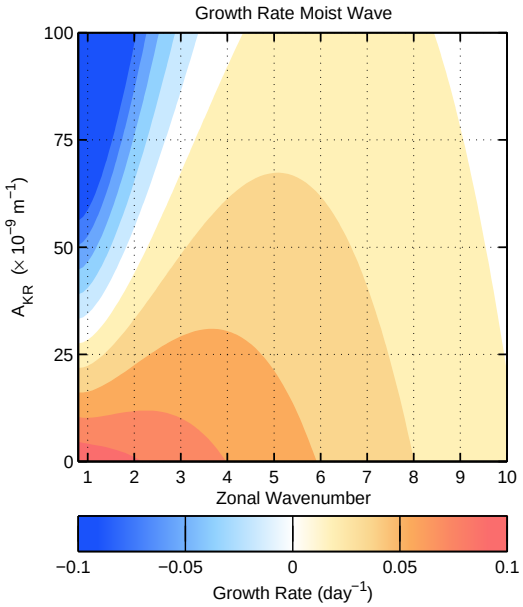

Figure 5.12: Growth rate, as obtained from Eq. (5.29b), as a function of k and A_{KR} for a linear moist wave where $L = 13{,}200$ km, $\tau_c = 13.7$ hours and r as determined by Eq. (5.31). Other values used in the calculation of the growth rate are shown in Tables 1 and 2.

might correspond to the "zonally-narrow MJO" described by Roundy (2014).

5.8 The MJO's dispersion relation in the wavenumber-frequency spectrum

Making use of the values of L and τ_c estimated in Chapter 5.5, we can use the dispersion relation in Eq. (5.29a), prescribing different values of A_{KR}, and compare it with the MJO's spectral signature in observations. The signal strength of OLR overlain by the dispersion relation derived in Eq. (5.29a), is shown in Fig. 5.13. Black triangles in the panel (a) depict the growth rate from $\tilde{M}^*_{tot}$ while the inverted triangles in panel (b) correspond to wave-induced damping. The sum of panels (a) and (b) is shown in panel (c). A robust fit between the observed signal and the derived dispersion relationship is observed. Most of the signal is concentrated between zonal wavenumbers 1-3 and at periods between 40 and 60 days, which roughly correspond to a value of A_{KR} between 20 and 40 $\times 10^{-9}$ m^{-1}. An

MJO with an effective zonal wavenumber $\bar{k} = 1.81$ and $\bar{A}_{KR} = 34.7 \times 10^{-9}$ m^{-1}, which best matches the phase speed and group velocity inferred from Fig. 5.4, is located near the centroid of the MJO's signal strength in all three diagrams (indicated by an asterisk).

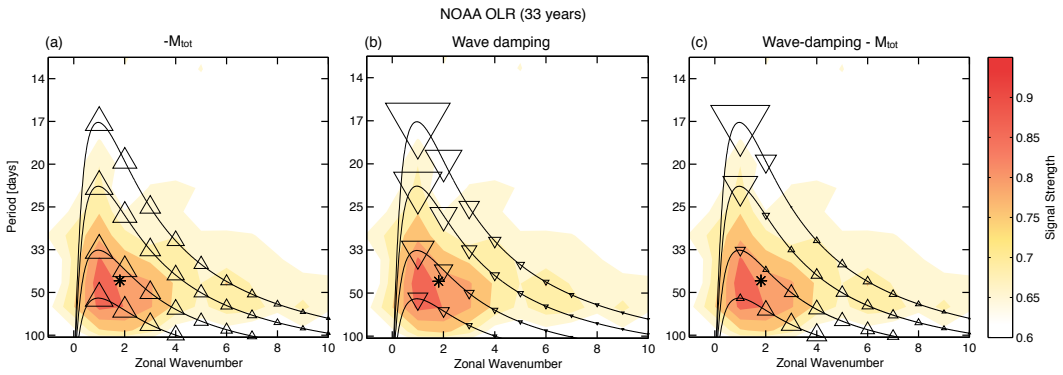

Figure 5.13: Signal strength of symmetric OLR averaged over the 15°S−15°N latitude belt. The curves correspond to frequencies obtained from Eq. (5.29a) for $L = 13{,}200$ km, $\tau_c = 13.7$ hours and A_{KR} of 25, 40 , 60 and 80 $\times 10^{-9}$ m^{-1} (appearing from bottom to top in the diagrams). Open black triangles in panel (a) depict the growth rate $\tilde{M}^*_{tot}$ obtained using Eq. (5.31) and are sized according to their magnitudes, inverted triangles in panel (b) correspond to wave damping (first term in Eq. 5.29b) and panel (c) shows the sum of the two terms. The asterisk corresponds to an MJO with $\bar{\tau} = 44$ days and $\bar{k} = 1.81$. Shading interval is 0.05 with the first contour beginning at 0.65.

An interesting feature of the MJO's signal in Fig. 5.13 is the extension of the signal strength to higher frequencies for zonal wavenumber 1, resulting in a triangular shape in the signal strength, a feature that has not been previously documented. The triangular shape of the wavenumber-frequency spectrum indicates that the MJO is a dispersive wave with an eastward phase speed and a westward group velocity, as documented in Part I and Chapter 5.4. The strongest signal is located over zonal wavenumbers 1 and 2, consistent with the growth rate from $\tilde{M}^*_{tot}$ (black triangles in Fig. 5.13a). It is also notable that the dispersion curves corresponding to larger values of A_{KR} (top curves) are associated with a weaker signal in zonal wavenumber 1 relative to the signal in wavenumbers 3 and 4, consistent with wave-driven damping being stronger at the largest scales, as shown by the larger size of

the inverted triangles over those locations in Fig. 5.13*b*. However, when both processes are considered together (Fig. 5.13*c*), wind driven damping exceeds the growth from $\tilde{M}^*_{tot}$ at the largest scales. The largest growth occurs instead in wavenumbers 4-6, whereas in the region where the spectral signature is strongest, wind driven damping and growth from $\tilde{M}^*_{tot}$ nearly cancel one another. This discrepancy between the linear moist wave and the observed MJO may be due to a time delay between the growth from $\tilde{M}^*_{tot}$ and the onset of wind-induced wave damping in observations (Zhao et al., 2012; Ling et al., 2013), that is not taken into account in our linear analysis. It is possible that the MJO's zonal scale is selected by the scale dependent r (Eq. 5.31) during initiation, well before the wind anomalies in the Rossby waves develop and begin to damp the moisture anomalies.

The MJO-derived dispersion curve alongside the dispersion curves for Kelvin, equatorial Rossby (ER) and tropical depression (TD) waves is shown in Fig. 5.14 in the format suggested by Wheeler and Kiladis (1999). In this diagram, A_{KR} plays a role analogous to the equivalent depth (h_e) characteristic of equatorial Kelvin and Rossby waves (see Kiladis et al. 2009). That the dispersion curve of the MJO so closely fits its observed spectrum, which is clearly separated from that of Kelvin waves, provides further evidence that it is driven by dynamics distinct from that of convectively coupled Rossby and Kelvin modes.

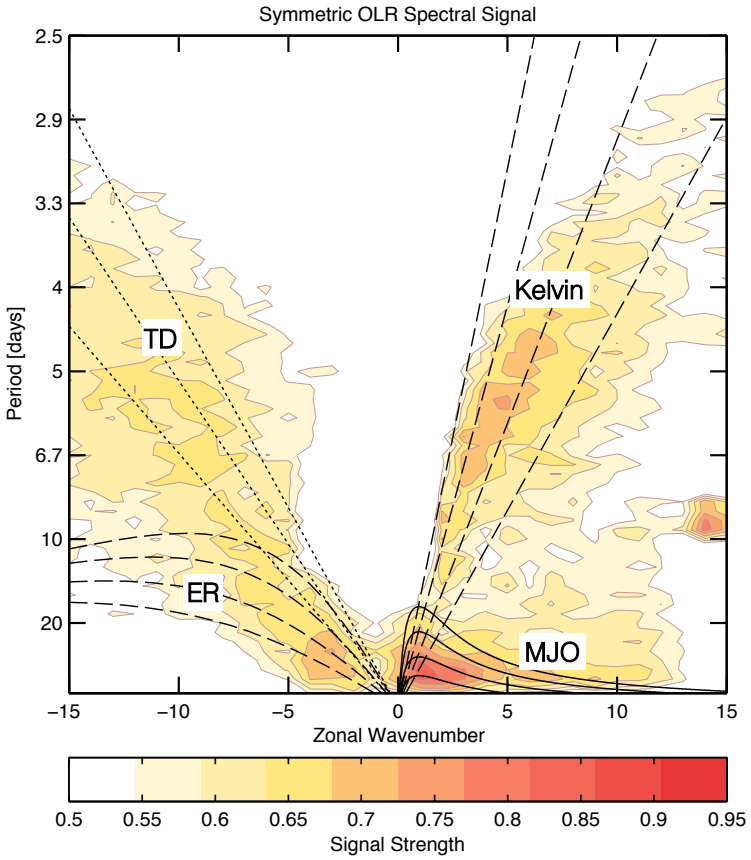

Figure 5.14: Signal strength of symmetric OLR anomalies averaged over the 15°S−15°N latitude belt. The MJO-related dispersion curves (solid lines) correspond to frequencies obtained from Eq. (5.29a) for L = 13,200 km, τ_c = 13.7 hours and A_{KR} of 25, 40, 60 and 80 $\times 10^{-9}$ m^{-1}. Dispersion curves are also plotted for Kelvin and equatorial Rossby (ER) (dashed lines), for equivalent depths (h_e) of 12, 25, 50, and 90 m. Dotted lines indicate constant phase speeds of 7.0, 9.0, and 11.0 m s^{-1} , which are representative of westward-propagating tropical depressions (TD) and easterly waves (see also Yasunaga and Mapes 2012). Contour interval is every 0.05 signal strength fraction begining at 0.55.

Chapter 6

SYNTHESIS AND CONCLUSIONS

6.1 Part I

In this part of the thesis, we used the global daily $\Delta\chi$ field as a time-varying MJO index and created "warm pool" composites by averaging the structure of the MJO as it propagates across the Indo-Pacific warm pool (60°E − 180°). In Chapter 3 we emphasized the upper and lower tropospheric structure of the MJO. We found that the bottom-up evolution in the vertical velocity and divergence fields in the MJO can be interpreted as the result of a superposition of zonal and meridional overturning circulations that are zonally shifted such that when they are added the resulting divergence field tilts westward with height.

In Chapter 4, we extended the analysis and results of Chapter 3 to construct a set of composites that yield a robust description of the structure and evolution of the moisture and precipitation fields, providing insight into the mechanisms that give rise to the eastward propagation of the MJO. While many previous studies have focused on the moisture budget of the MJO in the reanalysis fields (Benedict and Randall, 2007; Kiranmayi and Maloney, 2011; Hsu and Li, 2012), their analyses are largely based on the vertically integrated moisture or moist static energy budget. Our warm pool compositing simplifies the description of the MJO evolution; allowing a more concise identification of the salient features of its three-dimensional structure, shown schematically in Fig. 6.1. The composites indicate that a deep plume of ascent 20° to 60° to the east of the center of maximum ascent moistens the mid and upper troposphere through vertical moisture advection while diffuence above the BL widens the moist plume (bottom right panel of Fig. 6.1). Further analysis reveals that this plume of ascent is the result of strong boundary layer moisture convergence associated with the Kelvin wave response to equatorial heating, consistent with the interpretations of Wang

and Rui (1990); Maloney and Hartmann (1998); Hsu and Li (2012); and many others. Our warm pool composite analysis also reveals that horizontal moisture advection is an important moisture sink near and to the west of the region of maximum ascent, highlighting the role of the Rossby wave response in drying the region to the west of the enhanced convection.

We have also extended the use of the warm pool composite by using it to reconstruct the evolving MJO cycle as it propagates across the Indo-Pacific warm pool. When the MJO cycle is characterized as a dipole in convection, shown schematically in Fig. 6.2, we find that horizontal moisture advection plays an important role in moistening the lower troposphere to the east of the enhanced convection, in agreement with previous studies (Maloney, 2009; Andersen and Kuang, 2012; Pritchard and Bretherton, 2014; Kim et al., 2014; DeMott et al., 2014). At this time the anticyclones in the Rossby wave response to the suppressed convection over the western Pacific are moistening the region to the east of the region of maximum ascent (Figs. 4.15 and 4.16). The combined Kelvin and Rossby wave responses to the dipole heating pattern yield a moistening tendency that favors the growth and eastward propagation of the region of enhanced convection. The Rossby wave anticyclones produce horizontal moisture advection and the equatorial Kelvin wave produces vertical moisture advection (see Fig. 4.16 and bottom left panel of Fig. 6.2). The equatorial Kelvin wave response associated with the enhanced convection causes BL moisture convergence across the region of suppressed convection (bottom right panel of Fig. 6.2), which is associated with the anomalous moistening seen in the region of suppressed convection in Fig. 4.16 (denoted by a blue triangle).

Once the suppressed phase over the western Pacific decays, horizontal moisture advection contributes much less to the moistening tendency to the east of the enhanced convection. When we consider the MJO's complete cycle as it propagates across the Indo-Pacific warm pool (60°E−180°), we find that it is the vertical motion resulting from frictional convergence within the BL that provides the mid-tropospheric moistening required to explain the eastward propagation in the later stages, when the region of enhanced convection is propagating into the western Pacific. The moistening and drying by frictionally-driven vertical motion

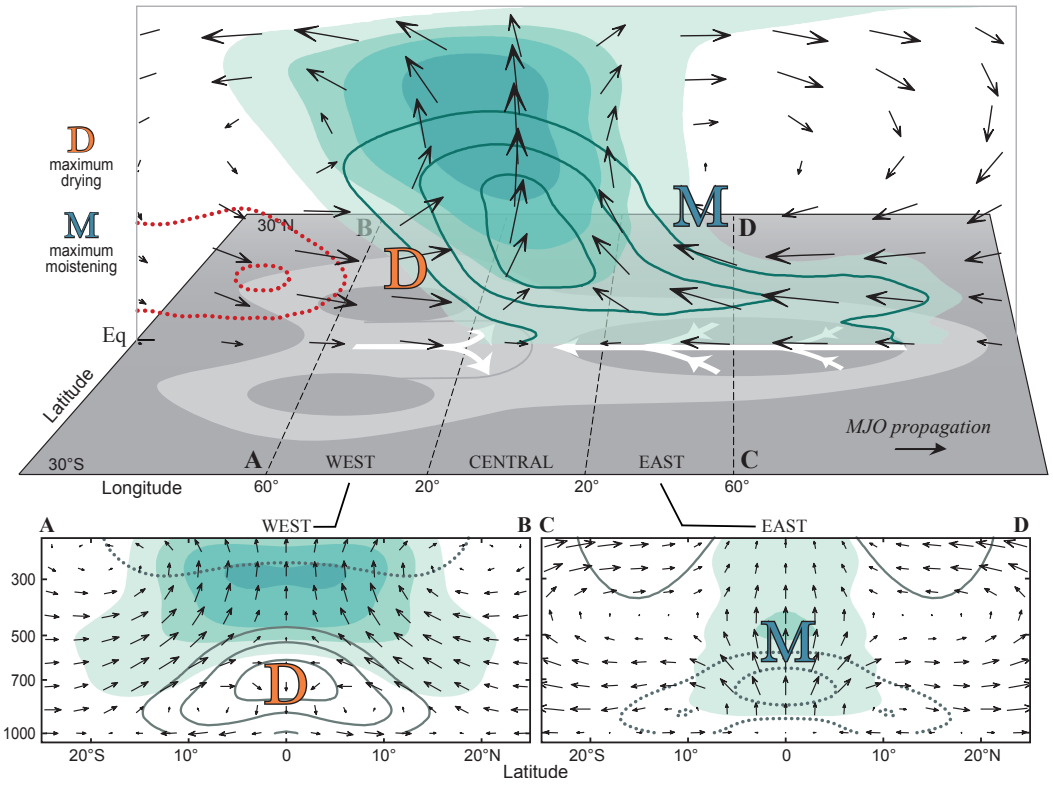

Figure 6.1: Schematic describing the three-dimensional structure of the MJO as described by the warm pool composite. The top panel shows specific humidity q (contoured) and relative humidity RH (shaded) and the zonal mass circulation (ρu, ρw) indicated by arrows. The horizontal plate corresponds to the observed surface geopotential height (Z) anomalies and the white arrows depict the flow in the boundary layer. **M** and **D** correspond to the regions in which the moisture tendency $\partial q/\partial t$ exhibits positive and negative extrema, respectively. The bottom panels are meridional cross sections as in the top left and right panels of Fig. 4.6, showing RH as colored shading, the zonal mass flux ρu as contours and the meridional mass circulation (ρu, ρw) as arrows. Only the equatorially symmetric component is shown with a reduced number of contours and gradations of shading. The conditions correspond to MJO phases 4 and 5 in the Wheeler and Hendon (2004) index.

and horizontal advection are inextricably linked to the "bottom up" evolution of the vertical motion profile and the "swallowtail shape" of the region of enhanced rainfall discussed in AW2, which were found to be attributable to the forced equatorial Kelvin and Rossby waves in the Matsuno-Gill response to an equatorial heat source. It follows that the forced equa-

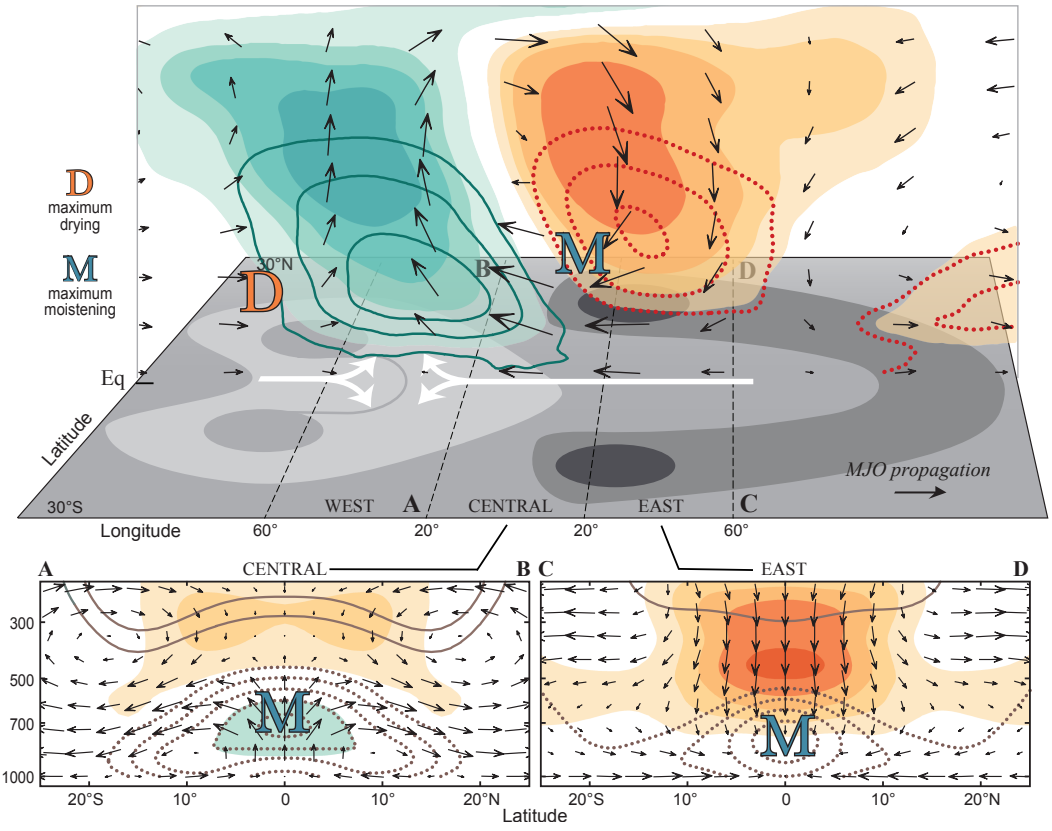

Figure 6.2: As in Fig. 6.1 but describing the three-dimensional structure of the MJO at the time when its center of enhanced convection is located over the Indian Ocean and the center of suppressed convection is located over the western Pacific. These conditions correspond to MJO phases 2 and 3 in the Wheeler and Hendon (2004) index.

torial Kelvin and Rossby waves can account for the observed lower-tropospheric structure of the MJO and the associated anomalous wind field is the primary mechanism that causes the eastward propagation of moisture anomalies.

6.2 Part II

In this part, we used the results of Part I to expand upon the theoretical model developed by Sobel and Maloney (2012, 2013) and made several important modifications in order to explain many of the observed characteristics of the MJO. These modifications are summarized as

follows:

1. Meridional and vertical dependences have been included in the form of parabolic cylinder functions and vertical basis functions, respectively, so that by doing this the horizontal structure of the Matsuno-Gill response can be treated explicitly and processes such as meridional moisture advection can be included.

2. It is assumed that the mean state varies only meridionally and vertically, and the basic equations are scaled accordingly (see Appendix).

3. Values for the free-tropospheric dissipation length scale L and the convective adjustment timescale τ_c have been determined directly from observational and reanalysis data.

As in Sobel and Maloney (2012, 2013), many of the processes included here are parameterized and meridionally truncated in order to make the mathematics more tractable: the possibility that we have oversimplified them is a caveat of this study. Despite these simplifications, a dispersion relation for the MJO is obtained that is largely in agreement with observations. This correspondence between theory and observations provides a strong case that the MJO is moist wave whose horizontal structure resembles the wave response to an equatorial heat source, as described in Matsuno (1966) and Gill (1980). Through the use of time-longitude sections we have shown that the MJO is characterized by a westward group velocity that is about 2/5 as large as its eastward phase speed, a feature of the MJO that has not been previously documented. This result is at odds with many previous studies (Wang and Rui, 1990; Raymond, 2001; Majda and Stechmann, 2009), who have suggested that the MJO is either non-dispersive or has zero group velocity. That the dispersion can be observed even without the use of composites, as seen in Fig. 5.3, attests to its significance.

The theoretical framework developed in Chapter 5 shows that the observed group velocity is a consequence of the anomalous wind field in the Matsuno-Gill response. In a free troposphere characterized by weak dissipation, the Rossby wave-related wind response causes the

westerlies to shift eastward towards the moist region (as seen in Fig. 5.1), resulting in wind-induced drying and a dispersion relation in which the westward group velocity is a fraction of its eastward phase speed. Furthermore, Rossby wave-induced damping is strongest at the largest scales and when the moisture advection parameter A_{KR} is larger. This wave damping at the largest scales is offset, to some extent, by the total gross moist stability, which favors the growth of the largest scales through feedbacks between clouds, moisture and longwave radiation.

The mechanism by which the group velocity enhances eastward propagation of the MJO is illustrated in Fig. 6.3. At lag -15 days, the dipole configuration of enhanced and suppressed convection results in strong wind anomalies from the interaction between the Kelvin wave response to the enhanced Indian Ocean convection and the anticyclonic Rossby wave response to the suppressed convection over the western Pacific. This superposition of the eastward phase propagation and the westward energy dispersion favors the amplification of the moist anomalies as they propagate across the Indian Ocean into the Maritime Continent, as seen at lag day -5 (roughly 1/4 cycle later). The phase speed and group velocity at the time when the MJO-related enhanced convection is centered over the Maritime Continent (lag day -5) favor the development of the suppressed phase in the Indian Ocean as the region of enhanced convection propagates into the western Pacific, which leads to the development of a dipole structure of reversed polarity, as shown in the bottom panel of Fig. 6.3.

The results presented in this study shed light on some of peculiar aspects of the MJO and on some of the results of previous studies. For example, Kim et al. (2014) found that when MJO-related enhancement of convection that develops over the Indian Ocean that are accompanied by suppressed convection over the west Pacific, it is able to propagate from the Indian Ocean into the Maritime Continent. Conversely, the flareups of convection whose structure is characterized as a monopole tend to decay without showing significant propagation (see their Fig. 4). Moreover, Adames and Wallace (2015) found that when the MJO is characterized by a dipole in convection, advection of mean moisture by the horizontal winds contributes not only to eastward phase propagation, but also to the amplification of

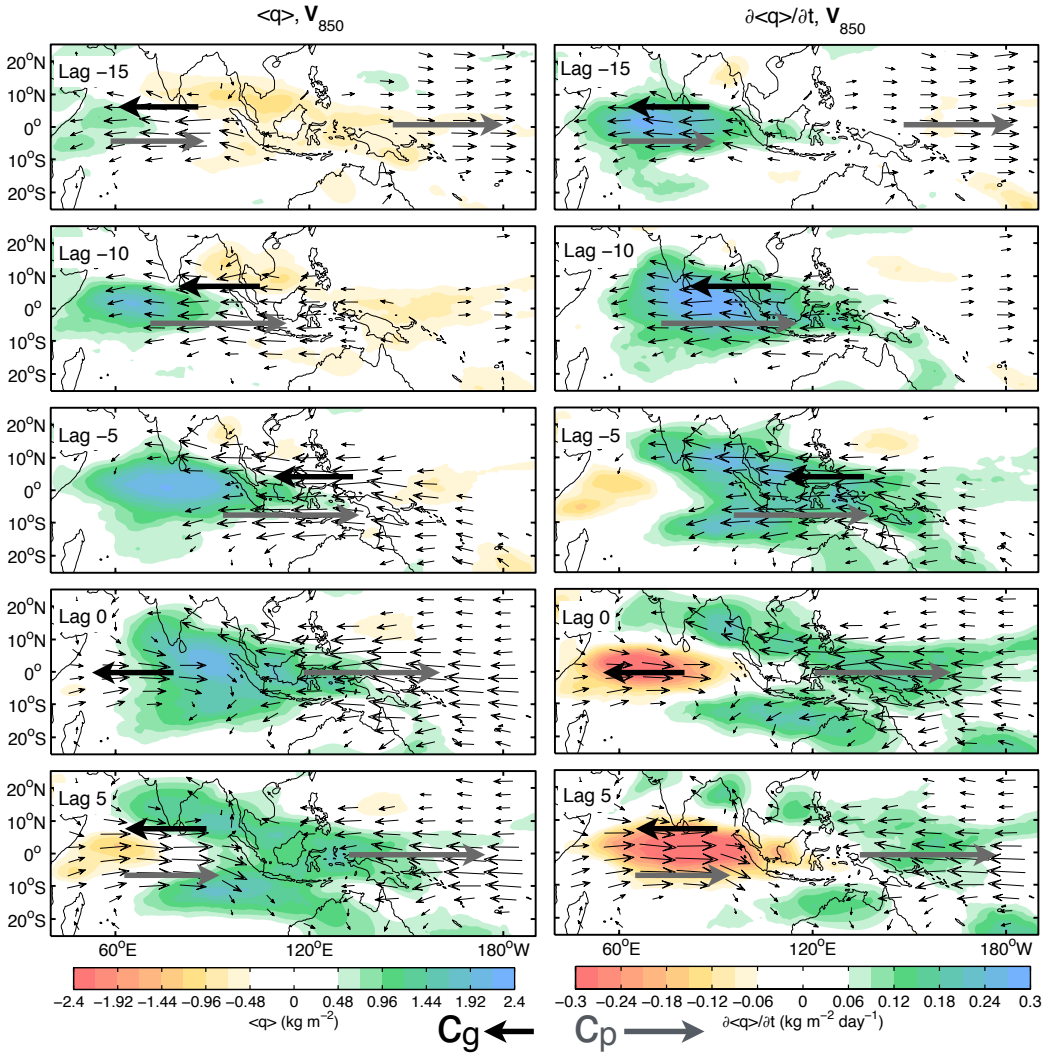

Figure 6.3: 5-panel schematic describing the dynamics of the dispersion relation derived in Eqs. (5.29) and (5.30) in relation to the observed MJO cycle. SSM/I-TMI PW ($\langle q \rangle$) is shaded in the left column while its temporal tendency ($\partial \langle q \rangle / \partial t$) is shaded in the right column, and arrows depict the 850 hPa horizontal wind anomalies. Lag day 0 corresponds to the time when OLR is a minimum over the Indian Ocean. The gray arrows depict the direction of the phase speed c_p and the black arrows correspond to the direction of the group velocity c_g. The position of the arrows and $\partial \langle q \rangle / \partial t$ correspond to the moisture anomalies 10 days later, which is roughly a quarter cycle of a composite MJO.

the anomalous moisture tendency to the east of the enhanced convection. These results indicate that in the absence of a region of suppressed convection over the western Pacific, the convective anomalies over the Indian Ocean lack the forcing required to enable them to propagate eastward across the warm pool and cannot maintain their structure against dissipation (wave damping). If the MJO were not a dispersive wave, this dichotomy between propagating and non-propagating MJO events wouldn't exist.

The largest growth in the linear wave in our analysis does not occur at the largest scales due to the strong effects of wind-driven damping. This is the result of our linear model assuming that the wind field is in instantaneous equilibrium with the diabatic heating. If we were to consider the time delay between the onset of convection and the balanced wind response, as seen in Fig. 6.3, then the spatial scale of the MJO could be explained, as it may be selected by cloud-moisture-radiation feedbacks during its developing stage, well before the wind anomalies of the wave response develop and begin to damp the wave and disperse energy. This observed scale-dependence in cloud-moisture-radiation feedback may be related to the process of "convective self aggregation". Such a result would be in agreement with results from Bretherton et al. (2005) and Arnold and Randall (2015), who found that longwave radiative feedbacks in association with upper-level clouds are responsible for large-scale self aggregation of convection. This mechanism may, in turn be related to the so-called "radiative-convective instability" discussed by Raymond (2000a); Wing and Emanuel (2014) and Emanuel et al. (2014).

All these results provide strong evidence that the coupling between tropospheric water vapor and deep convection is central to the MJO's dynamics, supporting Raymond and Fuchs (2009) labeling of the MJO as a "moisture mode" and the use of moisture as a prognostic variable. However, the MJO wouldn't exhibit its peculiar dispersive properties were it not for the central role of the Matsuno-Gill wave response in shaping the distribution of tropospheric humidity. Hence, it seems more appropriate to label the MJO as an *equatorial moisture wave* or a *Matsuno-Gill moist wave*, which can be thought of as a distinct type of moisture mode. This moisture wave can be considered to be an additional solution to Matsuno's

(1966) equatorial wave modes that arises when a prognostic moisture equation is coupled to equatorial heating.

The results presented in this study also suggest that the MJO is not a continuous cycle, as implied by 8-phase composites or regression maps based on two principal components. Rather, it should be considered to be a transient wavetrain in which new centers of enhanced and suppressed convection develop to the west of the existing ones. This transient wave nature of the MJO is analogous in some respects to that of midlatitude Rossby waves: the advection of moisture plays a role in the MJO analogous to that of advection of absolute vorticity in extratropical Rossby waves, and radiative-convective instability plays a role analogous to baroclinic instability in the midlatitudes. Additionally, the MJO-related moisture anomalies can also grow through advection of mean moisture by the anomalous flow (the group velocity) even in the absence of a positive growth rate, analogous to the role that ageostrophic fluxes of geopotential play in the downstream development of Rossby waves in the absence of baroclinic energy conversion, as discussed by Chang (1993) and Chang and Orlanski (1993). As such, the prognostic latent heat (moisture) equation shown in Eq. (5.8) could arguably be thought of as analogous to the quasi-geostrophic potential vorticity equation for Rossby wave motion, as suggested by Sobel (2002). In PV theory, however, the sources and sinks of PV are relatively small whereas large sources and sinks of moisture exist in the form of dissipation (non-infinite L) and a positive total gross moist stability (Eq. 5.18b).

6.3 Concluding Remarks

In Part I of this study, we have used the ERA-Interim vertical velocity ω field as a basis for interrelating the various MJO-related thermodynamic fields. It defines the reference longitude in our warm pool composites and it determines the strength of the leading terms in the moisture budget. Yet we have shown in Fig. 4.1 that the ERA-Interim precipitation field is substantially weaker than observed and is shifted slightly eastward of it. As pointed out by Mapes and Bacmeister (2012) this discrepancy is likely the result of an inadequate

parameterization of cumulus convection in the reanalysis. While this discrepancy is not large enough to invalidate the schematic shown in Fig. 6.1, it supports their conclusion that a rigorous quantitative diagnosis of the thermodynamics of the MJO will require analysis of fields across models that do and do not produce MJO-like disturbances that resemble observations, as well as observed fields.

In Parts I and II we show evidence of westward energy dispersion in the MJO and, and in Part II we developed a linear wave solution that describes many of its properties. In this framework, the amount of moisture available for the anomalous MJO flow to induce eastward propagation is defined as the "moisture advection parameter" A_{KR}. The processes considered here that are able to affect A_{KR} are horizontal and vertical moisture advection, surface latent heat fluxes and modulation of high frequency eddy activity. Many of these processes have been approximated and meridionally truncated in order to simplify the equations. Additionally, A_{KR} and τ_c are treated as spatially invariant in our analysis. In observations, zonal variations in the distribution of water vapor will cause A_{KR} and τ_c to vary in the horizontal plane. It would be interesting to carry out a simple modeling analysis in which the distribution of moisture is more realistic in order to obtain a more complete description of the dynamics of the MJO. Moreover, an observational analysis on how spatial variations in τ_c affect the relationship between moisture and precipitation during the MJO lifecycle has not been considered and remains a topic of future research.

Our results suggest that the total gross moist stability $\tilde{M}^*_{tot}$ plays a central role in the horizontal scale selection of the MJO through cloud-radiation interaction via a previously unidentified wavenumber dependence of the greenhouse enhancement parameter r. This dependence is the result of large-scale convection being more efficient at creating widespread regions of upper-level anvil clouds, which reduce OLR over the region. The details on how this scale dependence, convective self aggregation and the MJO interact are not entirely clear and remain the a possible for future research.

The dispersion relation derived in Chapter 5.3 and the greenhouse enhancement relation shown in Chapter 5.7 could prove to be a useful tools for model intercomparison. We expect

that models that produce a robust MJO will have a spectrum that follows the dispersion curves in Fig. 5.13, and values of r and L_r that resemble observations, while models in which the MJO is weak might be characterized by a signal that is shifted toward lower values of A_{KR} and smaller values of r and L_r. Moreover, the analysis of this study could be used to further understand how the MJO behaves in different climatic regimes.

BIBLIOGRAPHY

Ackerman, T. P., K.-N. Liou, F. P. Valero, and L. Pfister, 1988: Heating rates in tropical anvils. *J. Atmos. Sci.*, **45 (10)**, 1606–1623.

Adames, A. F., J. Patoux, and R. C. Foster, 2013: The contribution of extratropical waves to the MJO wind field. *J. Atmos. Sci.*, doi:10.1175/JAS-D-13-084.1.

Adames, Á. F., and J. M. Wallace, 2014a: Three-Dimensional Structure and Evolution of the MJO and Its Relation to the Mean Flow. *J. Atmos. Sci.*, **71 (6)**, 2007–2026.

Adames, Á. F., and J. M. Wallace, 2014b: Three-Dimensional Structure and Evolution of the Vertical Velocity and Divergence Fields in the MJO. *J. Atmos. Sci.*, **71 (12)**, 4661–4681.

Adames, Á. F., and J. M. Wallace, 2015: Three-Dimensional Structure and Evolution of the Moisture Field in the MJO. *J. Atmos. Sci.*, **72 (10)**, 3733–3754.

Andersen, J. A., and Z. Kuang, 2012: Moist Static Energy Budget of MJO-like Disturbances in the Atmosphere of a Zonally Symmetric Aquaplanet. *J. Climate*, **25 (8)**, 2782–2804.

Arnold, N. P., M. Branson, Z. Kuang, D. A. Randall, and E. Tziperman, 2015: MJO Intensification with Warming in the Superparameterized CESM. *J. Climate*, **28 (7)**, 2706–2724.

Arnold, N. P., Z. Kuang, and E. Tziperman, 2013: Enhanced MJO-like Variability at High SST. *J. Climate*, **26 (3)**, 988–1001.

Arnold, N. P., and D. A. Randall, 2015: Global-scale convective aggregation: Implications for the Madden-Julian oscillation. *J. Adv. Model. Earth Syst.*, n/a–n/a.

Bantzer, C. H., and J. M. Wallace, 1996: Intraseasonal Variability in Tropical Mean Temperature and Precipitation and Their Relation to the Tropical 40-50 Day Oscillation. *J. Atmos. Sci.*, **53 (21)**, 3032–3045.

Barlow, M., 2011: *The Madden-Julian Oscillation influence on Africa and West Asia. Intraseasonal Variability of the Atmosphere-Ocean Climate System*, Vol. 2. Praxis.

Barlow, M., M. Wheeler, B. Lyon, and H. Cullen, 2005: Modulation of daily precipitation over southwest asia by the madden–julian oscillation. *Monthly Weather Review*, **133 (12)**, 3579–3594.

Barnes, H. C., and R. A. Houze, 2013: The precipitating cloud population of the Madden-Julian Oscillation over the Indian and west Pacific Oceans. *J. Geophys. Res.*, **118 (13)**, 6996–7023.

Bechtold, P., J.-P. Chaboureau, A. Beljaars, A. K. Betts, M. Köhler, M. Miller, and J.-L. Redelsperger, 2004: The simulation of the diurnal cycle of convective precipitation over land in a global model. *Quart. J. Roy. Meteor. Soc.*, **130 (604)**, 3119–3137.

Benedict, J. J., E. D. Maloney, A. H. Sobel, and D. M. W. Frierson, 2014: Gross Moist Stability and MJO Simulation Skill in Three Full-Physics GCMs. *J. Atmos. Sci.*, **71 (9)**, 3327–3349.

Benedict, J. J., and D. A. Randall, 2007: Observed Characteristics of the MJO Relative to Maximum Rainfall. *J. Atmos. Sci.*, **64 (7)**, 2332–2354.

Bony, S., and K. A. Emanuel, 2005: On the Role of Moist Processes in Tropical Intraseasonal Variability: Cloud–Radiation and Moisture–Convection Feedbacks. *J. Atmos. Sci.*, **62 (8)**, 2770–2789.

Bretherton, C. S., P. N. Blossey, and M. Khairoutdinov, 2005: An energy-balance analysis of deep convective self-aggregation above uniform SST. *J. Atmos. Sci.*, **62 (12)**, 4273–4292.

Bretherton, C. S., M. E. Peters, and L. E. Back, 2004: Relationships between Water Vapor Path and Precipitation over the Tropical Oceans. *J. Climate*, **17 (7)**, 1517–1528.

Chang, E. K., and I. Orlanski, 1993: On the dynamics of a storm track. *J. Atmos. Sci.*, **50 (7)**, 999–1015.

Chang, E. K. M., 1993: Downstream Development of Baroclinic Waves As Inferred from Regression Analysis. *J. Atmos. Sci.*, **50 (13)**, 2038–2053.

Charney, J. G., 1963: A Note on Large-Scale Motions in the Tropics. *J. Atmos. Sci.*, **20 (6)**, 607–609.

Charney, J. G., and A. Eliassen, 1964: On the Growth of the Hurricane Depression. *J. Atmos. Sci.*, **21 (1)**, 68–75.

Dee, D. P., and Coauthors, 2011: The ERA-Interim reanalysis: configuration and performance of the data assimilation system. *Quart. J. Roy. Meteor. Soc.*, **137 (656)**, 553–597.

DeMott, C. A., C. Stan, D. A. Randall, and M. D. Branson, 2014: Intraseasonal Variability in Coupled GCMs: The Roles of Ocean Feedbacks and Model Physics. *J. Climate*, **27 (13)**, 4970–4995.

Deser, C., 1993: Diagnosis of the surface momentum balance over the tropical pacific ocean. *J. Climate*, **6 (1)**, 64–74.

Duchon, C. E., 1979: Lanczos Filtering in One and Two Dimensions. *Journal of Applied Meteorology*, **18 (8)**, 1016–1022.

Emanuel, K., A. A. Wing, and E. M. Vincent, 2014: Radiative-convective instability. *J. Adv. Model. Earth Syst.*, **6 (1)**, 75–90.

Fuchs, Ž., and D. J. Raymond, 2002: Large-scale modes of a nonrotating atmosphere with water vapor and cloud–radiation feedbacks. *J. Atmos. Sci.*, **59 (10)**, 1669–1679.

Fuchs, Z., and D. J. Raymond, 2005: Large-scale modes in a rotating atmosphere with radiative-convective instability and WISHE. *J. Atmos. Sci.*, **62 (11)**, 4084–4094.

Fuchs, Ž., and D. J. Raymond, 2007: A simple, vertically resolved model of tropical disturbances with a humidity closure. *Tellus A*, **59 (3)**, 344–354.

Ghil, M., and K. Mo, 1991: Intraseasonal Oscillations in the Global Atmosphere. Part II: Southern Hemisphere. *J. Atmos. Sci.*, **48 (5)**, 780–790.

Gill, A. E., 1980: Some simple solutions for heat-induced tropical circulation. *Quart. J. Roy. Meteor. Soc.*, **106 (449)**, 447–462.

Haertel, P. T., G. N. Kiladis, A. Denno, and T. M. Rickenbach, 2008: Vertical-Mode Decompositions of 2-Day Waves and the Madden–Julian Oscillation. *J. Atmos. Sci.*, **65 (3)**, 813–833.

Hagos, S., Z. Feng, K. Landu, and C. N. Long, 2014: Advection, moistening, and shallow-to-deep convection transitions during the initiation and propagation of madden-julian oscillation. *J. Adv. Model. Earth Syst.*, **6 (3)**, 938–949.

Hayashi, Y., 1981: Space-Time Spectral Analysis and its Application to Atmospheric Waves. *J. Meteor. Soc. Japan*, **60**, 156–171.

Heckley, W. A., and A. E. Gill, 1984: Some simple analytical solutions to the problem of forced equatorial long waves. *Quart. J. Roy. Meteor. Soc.*, **110 (463)**, 203–217.

Held, I. M., R. S. Hemler, and V. Ramaswamy, 1993: Radiative-Convective Equilibrium with Explicit Two-Dimensional Moist Convection. *J. Atmos. Sci.*, **50 (23)**, 3909–3927.

Hendon, H. H., and M. L. Salby, 1994: The Life Cycle of the Madden-Julian Oscillation. *J. Atmos. Sci*, **51**, 2225–2237, doi:10.1175/1520-0469.

Hendon, H. H., and M. C. Wheeler, 2008: Some Space-Time Spectral Analyses of Tropical Convection and Planetary-Scale Waves. *J. Atmos. Sci.*, **65 (9)**, 2936–2948.

Hoell, A., M. Barlow, and R. Saini, 2012: The leading pattern of intraseasonal and interannual indian ocean precipitation variability and its relationship with asian circulation during the boreal cold season. *J. Climate*, **25 (21)**, 7509–7526.

Hohenegger, C., and B. Stevens, 2013: Preconditioning Deep Convection with Cumulus Congestus. *J. Atmos. Sci.*, **70 (2)**, 448–464.

Holloway, C. E., and J. D. Neelin, 2009: Moisture Vertical Structure, Column Water Vapor, and Tropical Deep Convection. *J. Atmos. Sci.*, **66 (6)**, 1665–1683.

Houze, R. A., 1989: Observed structure of mesoscale convective systems and implications for large-scale heating. *Quart. J. Roy. Meteor. Soc.*, **115 (487)**, 425–461.

Houze, R. A., Jr., 1982: Cloud Clusters and Large-Scale Vertical Motions in the Tropics. *J. Meteor. Soc. Japan. Ser. II*, **60 (1)**, 396–410.

Hsu, P.-c., and T. Li, 2012: Role of the Boundary Layer Moisture Asymmetry in Causing the Eastward Propagation of the Madden-Julian Oscillation. *J. Climate*.

Hu, Q., and D. A. Randall, 1994: Low-frequency oscillations in radiative-convective systems. *J. Atmos. Sci.*, **51 (8)**, 1089–1099.

Huffman, G. J., and Coauthors, 2007: The TRMM Multisatellite Precipitation Analysis (TMPA): Quasi-Global, Multiyear, Combined-Sensor Precipitation Estimates at Fine Scales. *Journal of Hydrometeorology*, **8 (1)**, 38–55.

Jiang, X., and Coauthors, 2011: Vertical Diabatic Heating Structure of the MJO: Intercomparison between Recent Reanalyses and TRMM Estimates. *Mon. Wea. Rev.*, **139 (10)**, 3208–3223.

Johnson, R. H., and P. E. Ciesielski, 2013: Structure and Properties of Madden-Julian Oscillations Deduced from DYNAMO Sounding Arrays. *J. Atmos. Sci.*

Johnson, R. H., P. E. Ciesielski, J. H. Ruppert, and M. Katsumata, 2014: Sounding-Based Thermodynamic Budgets for DYNAMO. *J. Atmos. Sci.*

Kang, I.-S., F. Liu, M.-S. Ahn, Y.-M. Yang, and B. Wang, 2013: Role of SST structure on convectively coupled Kelvin-Rossby waves and its implication on MJO formation. *J. Climate*.

Karoly, D. J., 1989: Southern hemisphere circulation features associated with El Niño-Southern Oscillation events. *J. Climate*, **2 (11)**, 1239–1252.

Kiladis, G. N., K. H. Straub, and P. T. Haertel, 2005: Zonal and vertical structure of the Madden-Julian Oscillation. *J. Atmos. Sci.*, **62**, 2790–2809.

Kiladis, G. N., M. C. Wheeler, P. T. Haertel, K. H. Straub, and P. E. Roundy, 2009: Convectively Coupled Equatorial Waves. *Rev. Geophys.*, 1–42.

Kim, D., M.-S. Ahn, I.-S. Kang, and A. D. Del Genio, 2015: Role of Longwave Cloud–Radiation Feedback in the Simulation of the Madden–Julian Oscillation. *J. Climate*, **28 (17)**, 6979–6994.

Kim, D., J.-S. Kug, and A. H. Sobel, 2014: Propagating versus Nonpropagating Madden–Julian Oscillation Events. *J. Climate*, **27 (1)**, 111–125.

Kim, D., A. H. Sobel, and I.-S. Kang, 2011: A mechanism denial study on the Madden-Julian Oscillation. *J. Adv. Model. Earth Syst.*, **3 (4)**, n/a–n/a.

Kim, D., and Coauthors, 2009: Application of MJO Simulation Diagnostics to Climate Models. *J. Climate*, **22 (23)**, 6413–6436.

Kiranmayi, L., and E. D. Maloney, 2011: Intraseasonal moist static energy budget in reanalysis data. *J. Geophys. Res.*, **116 (D21)**, 1–12.

Knutson, T. R., and K. M. Weickmann, 1987: 30-60 Day Atmospheric Oscillations: Composite Life Cycles of Convection and Circulation Anomalies. *Mon. Wea. Rev.*, **115 (7)**, 1407–1436.

Kållberg, P., P. Berrisford, B. Hoskins, A. Simmmons, S. Uppala, S. Lamy-Thépaut, and R. Hine, 2005: ERA-40 Atlas. Tech. rep., ECMWF, 191 pp.

Kumar, V. V., A. Protat, C. Jakob, and P. T. May, 2014: On the Atmospheric Regulation of the Growth of Moderate to Deep Cumulonimbus in a Tropical Environment. *J. Atmos. Sci.*, **71 (3)**, 1105–1120.

Lau, K., and L. Peng, 1987: Origin of low-frequency intraseasonal oscillations in the tropical atmosphere. Part I: Basic theory. *J. Atmos. Sci.*, **44**, 950–972.

Lau, K.-M., and H.-T. Wu, 2010: Characteristics of Precipitation, Cloud, and Latent Heating Associated with the Madden–Julian Oscillation. *J. Climate*, **23 (3)**, 504–518.

Lee, S.-K., C. Wang, and B. E. Mapes, 2009: A Simple Atmospheric Model of the Local and Teleconnection Responses to Tropical Heating Anomalies. *J. Climate*, **22 (2)**, 272–284.

Li, T., and B. Wang, 1994: A thermodynamic equilibrium climate model for monthly mean surface winds and precipitation over the tropical pacific. *Journal of the atmospheric sciences*, **51 (11)**, 1372–1385.

Liebmann, B., and C. A. Smith, 1996: Description of a complete (interpolated) outgoing longwave radiation dataset. *Bull. Amer. Met. Soc.*, **77**, 1275–1277.

Lin, J.-L., and B. Mapes, 2004a: Wind shear effects on cloud-radiation feedback in the western Pacific warm pool. *Geophys. Res. Lett.*, **31 (16)**.

Lin, J.-L., and B. E. Mapes, 2004b: Radiation Budget of the Tropical Intraseasonal Oscillation. *J. Atmos. Sci.*, **61 (16)**, 2050–2062.

Lindzen, R. S., 1974: Wave-CISK in the Tropics. *J. Atmos. Sci.*, **31 (1)**, 156–179.

Ling, J., C. Zhang, and P. Bechtold, 2013: Large-Scale Distinctions between MJO and Non-MJO Convective Initiation over the Tropical Indian Ocean. *J. Atmos. Sci.*, **70 (9)**, 2696–2712.

Liu, F., and B. Wang, 2012: A Frictional Skeleton Model for the Madden–Julian Oscillation. *J. Atmos. Sci.*, **69 (9)**, 2749–2758.

López Carrillo, C., and D. J. Raymond, 2005: Moisture Tendency Equations in a Tropical Atmosphere. *J. Atmos. Sci.*, **62 (5)**, 1601–1613.

Madden, R., and P. Julian, 1971: Detection of a 40-50 day oscillation in the zonal wind in the tropical Pacific. *J. Atmos. Sci.*, **28**, 702–708, doi:10.1175/1520-0469(1971)028⟨0702DOADOI⟩2.0.CO;2.

Madden, R., and P. Julian, 1972: Description of global scale circulation cells in the tropics with a 40-50 day period. *J. Atmos. Sci.*, **29**, 1109 – 1123, doi:10.1175/1520-0469(1972)029⟨1109:DOGSCC⟩2.0.CO;2.

Majda, A. J., and B. Khouider, 2001: A numerical strategy for efficient modeling of the equatorial wave guide. *Proc. Natl. Acad. Sci.*, **98 (4)**, 1341–1346.

Majda, A. J., and M. G. Shefter, 2001: Waves and instabilities for model tropical convective parameterizations. *J. Atmos. Sci.*, **58 (8)**, 896–914.

Majda, A. J., and S. N. Stechmann, 2009: The skeleton of tropical intraseasonal oscillations. *Proc. Natl. Acad. Sci. USA*, **106 (21)**, 8417–8422.

Maloney, E. D., 2009: The moist static energy budget of a composite tropical intraseasonal oscillation in a climate model. *J. Climate*, **22 (3)**, 711–729.

Maloney, E. D., and M. J. Dickinson, 2003: The Intraseasonal Oscillation and the Energetics of Summertime Tropical Western North Pacific Synoptic-Scale Disturbances. *J. Atmos. Sci.*, **60 (17)**, 2153–2168.

Maloney, E. D., and S. K. Esbensen, 2003: The Amplification of East Pacific Madden–Julian Oscillation Convection and Wind Anomalies during June–November. *J. Climate*, **16 (21)**, 3482–3497.

Maloney, E. D., and D. L. Hartmann, 1998: Frictional moisture convergence in a composite life cycle of the Madden-Julian Oscillation. *J. Climate*, **11**, 2387–2403.

Maloney, E. D., and S.-P. Xie, 2013: Sensitivity of tropical intraseasonal variability to the pattern of climate warming. *J. Adv. Model. Earth Syst.*, **5 (1)**, 32–47.

Manabe, S., and R. F. Strickler, 1964: Thermal equilibrium of the atmosphere with a convective adjustment. *J. Atmos. Sci.*, **21 (4)**, 361–385.

Mapes, B. E., and J. T. Bacmeister, 2012: Diagnosis of Tropical Biases and the MJO from Patterns in the MERRA Analysis Tendency Fields. *J. Climate*, **25 (18)**, 6202–6214.

Masunaga, H., 2007: Seasonality and regionality of the Madden- Julian oscillation, Kelvin wave and equatorial Rossby wave. *J. Atmos. Sci.*, **64**, 4400–4416, doi:10.1175/2007JAS2179.1.

Masunaga, H., 2013: A Satellite Study of Tropical Moist Convection and Environmental Variability: A Moisture and Thermal Budget Analysis. *J. Atmos. Sci.*, **70 (8)**, 2443–2466.

Matsuno, T., 1966: Quasi-geostrophic motions in the equatorial area. *J. Meteor. Soc. Japan*, **44**, 25–43.

Matthews, A. J., 2000: Propagation mechanisms for the Madden-Julian Oscillation. *Quart. J. Roy. Meteor. Soc.*, **126**, 2637–2651.

Milliff, R. F., and R. A. Madden, 1996: The existence and vertical structure of fast, eastward-moving disturbances in the equatorial troposphere. *J. Atmos. Sci.*, **53 (4)**, 586–597.

Mo, K. C., and R. W. Higgins, 1998: The Pacific??South American Modes and Tropical Convection during the Southern Hemisphere Winter. *Mon. Wea. Rev.*, **126 (6)**, 1581–1596, doi:10.1175/1520-0493(1998)126⟨1581:TPSAMA⟩2.0.CO;2, URL http://dx.doi.org/10.1175/1520-0493(1998)126⟨1581:TPSAMA⟩2.0.CO2.

Muller, C. J., L. E. Back, P. A. O'Gorman, and K. A. Emanuel, 2009: A model for the relationship between tropical precipitation and column water vapor. *Geophys. Res. Lett.*, **36 (16)**, n/a–n/a.

Murakami, T., 1988: Intraseasonal Atmospheric Teleconnection Patterns during the Northern Hemisphere Winter. *J. Climate*, **1 (2)**, 117–131.

Myers, D. S., and D. E. Waliser, 2003: Three-Dimensional Water Vapor and Cloud Variations Associated with the Madden–Julian Oscillation during Northern Hemisphere Winter. *J. Climate*, **16 (6)**, 929–950.

Neelin, J. D., and I. M. Held, 1987: Modeling Tropical Convergence Based on the Moist Static Energy Budget. *Monthly Weather Review*, **115 (1)**, 3–12.

Neelin, J. D., I. M. Held, and K. H. Cook, 1987: Evaporation-wind feedback and low-frequency variability in the tropical atmosphere. *J. Atmos. Sci.*, **44**, 2341–2348.

Neelin, J. D., and J.-Y. Yu, 1994: Modes of tropical variability under convective adjustment and the madden–julian oscillation. part i: Analytical theory. *J. Atmos. Sci.*, **51 (13)**, 1876–1894.

Neelin, J. D., and N. Zeng, 2000: A Quasi-Equilibrium Tropical Circulation Model—Formulation*. *J. Atmos. Sci.*, **57 (11)**, 1741–1766.

Peters, M. E., and C. S. Bretherton, 2005: A simplified model of the Walker circulation with an interactive ocean mixed layer and cloud-radiative feedbacks. *J. Climate*, **18 (20)**, 4216–4234.

Powell, S. W., and R. A. Houze, 2013: The cloud population and onset of the Madden-Julian Oscillation over the Indian Ocean during DYNAMO-AMIE. *J. Geophys. Res.*, **118 (21)**, 11,979–11,995.

Pritchard, M. S., and C. S. Bretherton, 2014: Causal Evidence that Rotational Moisture Advection is Critical to the Superparameterized Madden–Julian Oscillation. *J. Atmos. Sci.*, **71 (2)**, 800–815.

Raymond, D. J., 2000a: The Hadley circulation as a radiative-convective instability. *J. Atmos. Sci.*, **57 (9)**, 1286–1297.

Raymond, D. J., 2000b: Thermodynamic control of tropical rainfall. *Quart. J. Roy. Meteor. Soc.*, **126 (564)**, 889–898, doi:10.1002/qj.49712656406, URL http://dx.doi.org/10.1002/qj.49712656406.

Raymond, D. J., 2001: A new model of the madden–julian oscillation. *J. Atmos. Sci.*, **58 (18)**, 2807–2819.

Raymond, D. J., and Ž. Fuchs, 2009: Moisture Modes and the Madden–Julian Oscillation. *J. Climate*, **22 (11)**, 3031–3046.

Raymond, D. J., S. L. Sessions, and Ž. Fuchs, 2007: A theory for the spinup of tropical depressions. *Quart. J. Roy. Meteor. Soc.*, **133 (628)**, 1743–1754.

Raymond, D. J., S. L. Sessions, A. H. Sobel, and Ž. Fuchs, 2009: The Mechanics of Gross Moist Stability. *J. Adv. Model. Earth Syst.*, **1 (3)**, n/a–n/a.

Romps, D. M., 2014: Rayleigh damping in the free troposphere. *J. Atmos. Sci.*, **71 (2)**, 553–565.

Roundy, P. E., 2014: Regression analysis of zonally narrow components of the MJO. *J. Atmos. Sci.*, **71 (11)**, 4253–4275.

Roundy, P. E., and W. M. Frank, 2004: A Climatology of Waves in the Equatorial Region. *J. Atmos. Sci.*, **61 (17)**, 2105–2132.

Rui, H., and B. Wang, 1990: Development Characteristics and Dynamic Structure of Tropical Intraseasonal Convection Anomalies. *J. Atmos. Sci.*, **47 (3)**, 357–379.

Schumacher, C., R. A. Houze, and I. Kraucunas, 2004: The Tropical Dynamical Response to Latent Heating Estimates Derived from the TRMM Precipitation Radar. *J. Atmos. Sci.*, **61 (12)**, 1341–1358.

Seager, R., 1991: A simple model of the climatology and variability of the low-level wind field in the tropics. *J. Climate*, **4 (2)**, 164–179.

Seo, K.-H., and W. Wang, 2010: The Madden–Julian Oscillation Simulated in the NCEP Climate Forecast System Model: The Importance of Stratiform Heating. *J. Climate*, **23 (18)**, 4770–4793.

Sobel, A., and E. Maloney, 2012: An idealized semi-empirical framework for modeling the Madden-Julian oscillation. *J. Atmos. Sci.*, **69 (5)**, 1691–1705.

Sobel, A., and E. Maloney, 2013: Moisture Modes and the Eastward Propagation of the MJO. *J. Atmos. Sci.*, **70 (1)**, 187–192.

Sobel, A., S. Wang, and D. Kim, 2014: Moist static energy budget of the MJO during DYNAMO. *J. Atmos. Sci.*, **71 (11)**, 4276–4291.

Sobel, A. H., 2002: Water vapor as an active scalar in tropical atmospheric dynamics. *Chaos*, **12 (2)**, 451–459, doi:http://dx.doi.org/10.1063/1.1480795.

Sobel, A. H., and C. S. Bretherton, 2000: Modeling Tropical Precipitation in a Single Column. *J. Climate*, **13 (24)**, 4378–4392.

Sobel, A. H., and H. Gildor, 2003: A Simple Time-Dependent Model of SST Hot Spots. *J. Climate*, **16 (23)**, 3978–3992.

Sobel, A. H., J. Nilsson, and L. M. Polvani, 2001: The Weak Temperature Gradient Approximation and Balanced Tropical Moisture Waves. *J. Atmos. Sci.*, **58 (23)**, 3650–3665.

Sperber, K. R., 2003: Propagation and the vertical structure of the Madden-Julian Oscillation. *Mon. Wea. Rev.*, **131**, 3018–3037.

Stevens, B., J. Duan, J. C. McWilliams, M. Münnich, and J. D. Neelin, 2002: Entrainment, Rayleigh friction, and boundary layer winds over the tropical Pacific. *Journal of climate*, **15 (1)**, 30–44.

Straub, K. H., 2013: MJO Initiation in the Real-Time Multivariate MJO Index. *J. Climate*, **26 (4)**, 1130–1151.

Sugiyama, M., 2009a: The Moisture Mode in the Quasi-Equilibrium Tropical Circulation Model. Part I: Analysis Based on the Weak Temperature Gradient Approximation. *J. Atmos. Sci.*, **66 (6)**, 1507–1523.

Sugiyama, M., 2009b: The Moisture Mode in the Quasi-Equilibrium Tropical Circulation Model. Part II: Nonlinear Behavior on an Equatorial β Plane. *J. Atmos. Sci.*, **66 (6)**, 1525–1542.

Sukhatme, J., 2014: Low-frequency modes in an equatorial shallow-water model with moisture gradients. *Quart. J. Roy. Meteor. Soc.*, **140 (683)**, 1838–1846, doi:10.1002/qj.2264, URL http://dx.doi.org/10.1002/qj.2264.

Waliser, D., and Coauthors, 2009: MJO Simulation Diagnostics. *J. Climate*, **22**, 3006–3030, doi:10.1175/2008JCLI2731.1.

Wallace, J. M., and D. S. Gutzler, 1981: Teleconnections in the Geopotential Height Field during the Northern Hemisphere Winter. *Mon. Wea. Rev.*, **109 (4)**, 784–812.

Wallace, J. M., and P. V. Hobbs, 2006: *Atmospheric science: an introductory survey*, Vol. 92. Academic press.

Wang, B., 1988: Dynamics of Tropical Low-Frequency Waves: An Analysis of the Moist Kelvin Wave. *J. Atmos. Sci.*, **45 (14)**, 2051–2065.

Wang, B., and T. Li, 1994: Convective Interaction with Boundary-Layer Dynamics in the Development of a Tropical Intraseasonal System. *J. Atmos. Sci.*, **51 (11)**, 1386–1400.

Wang, B., and H. Rui, 1990: Dynamics of the Coupled Moist Kelvin-Rossby Wave on an Equatorial β-Plane. *J. Atmos. Sci.*, **47 (4)**, 397–413.

Weickmann, K., W. Robinson, and C. Penland, 2000: Stochastic and oscillatory forcing of global atmospheric angular momentum. *Journal of geophysical ...*, **105 (D12)**, 15 543–15 557.

Weickmann, K. M., and P. D. Sardeshmukh, 1994: The Atmospheric Angular Momentum Cycle Associated with a Madden-Julian Oscillation. *J. Atmos. Sci.*, **51 (21)**, 3194–3208.

Wheeler, M., and G. N. Kiladis, 1999: Convectively coupled equatorial waves: Analysis of clouds and temperature in the wavenumber-frequency domain. *J. Atmos. Sci.*, **56**, 374–399, doi:10.1175/1520-0469(1999)056⟨0374:CCEWAO⟩2.0.CO;2.

Wheeler, M., G. N. Kiladis, and P. J. Webster, 2000: Large-scale dynamical fields associated with convectively coupled equatorial waves. *J. Atmos. Sci.*, **57**, 613 – 640, doi:10.1175/1520-0469(2000)057⟨0613:LSDFAW⟩2.0.CO;2.

Wheeler, M. C., and H. H. Hendon, 2004: An All-Season Real-Time Multivariate MJO Index: Development of an Index for Monitoring and Prediction. *Mon. Wea. Rev.*, **132 (8)**, 1917–1932.

Wing, A. A., and K. A. Emanuel, 2014: Physical mechanisms controlling self-aggregation of convection in idealized numerical modeling simulations. *J. Adv. Model. Earth Syst.*, **6 (1)**, 59–74.

Wu, Z., E. S. Sarachik, and D. S. Battisti, 2001: Thermally Driven Tropical Circulations under Rayleigh Friction and Newtonian Cooling: Analytic Solutions. *J. Atmos. Sci.*, **58 (7)**, 724–741.

Xu, W., and S. A. Rutledge, 2014: Convective Characteristics of the Madden–Julian Oscillation over the Central Indian Ocean Observed by Shipborne Radar during DYNAMO. *J. Atmos. Sci.*, **71 (8)**, 2859–2877.

Yanai, M., S. Esbensen, and J. Chu, 1973: Determination of bulk properties of tropical cloud clusters from large-scale heat and moisture budgets. *J. Atmos. Sci.*, **30**, 611–627, doi:10.1175/1520-0469(1973)030⟨0611:DOBPOT⟩2.0.CO;2.

Yanai, M., and M. Murakami, 1970: Spectrum analysis of symmetric and antisymmetric equatorial waves. *J. Meteor. Soc. Japan*, **48**, 331–347, doi:10.1175/1520-0469(2000)057⟨0613:LSDFAW⟩2.0.CO;2.

Yasunaga, K., and B. Mapes, 2012: Differences between More Divergent and More Rotational Types of Convectively Coupled Equatorial Waves. Part I: Space-Time Spectral Analyses. *J. Atmos. Sci.*, **69 (1)**, 3–16.

Zeng, N., J. D. Neelin, and C. Chou, 2000: A Quasi-Equilibrium Tropical Circulation Model—Implementation and Simulation*. *J. Atmos. Sci.*, **57 (11)**, 1767–1796.

Zhang, C., and J. Ling, 2012: Potential Vorticity of the Madden–Julian Oscillation. *J. Atmos. Sci.*, **69 (1)**, 65–78.

Zhao, C., T. Li, and T. Zhou, 2012: Precursor Signals and Processes Associated with MJO Initiation over the Tropical Indian Ocean*. *J. Climate*, **26 (1)**, 291–307.

Zhu, H., and H. Hendon, 2015: Role of large scale moisture advection for simulation of the MJO with increased entrainment. *Quart. J. Roy. Meteor. Soc.*, doi:10.1002/qj.2510.

Appendix A

SCALING OF THE PRIMITIVE EQUATIONS

The system of equations shown in Eq. (1) arise from scaling the primitive equations on an equatorial beta plane. The primitive equations have the following form:

$$\frac{\partial u}{\partial t} + \varepsilon u + \mathbf{V} \cdot \nabla u + \omega \frac{\partial u}{\partial p} - \beta y v = -\frac{\partial \phi}{\partial x} \tag{A.1a}$$

$$\frac{\partial v}{\partial t} + \varepsilon v + \mathbf{V} \cdot \nabla v + \omega \frac{\partial v}{\partial p} + \beta y u = -\frac{\partial \phi}{\partial y} \tag{A.1b}$$

$$\frac{\partial \phi}{\partial p} = -\frac{R_d T}{p} \tag{A.1c}$$

$$\nabla \cdot \mathbf{V} + \frac{\partial \omega}{\partial p} = 0 \tag{A.1d}$$

$$C_p \left(\frac{\partial T}{\partial t} + \varepsilon (T - \bar{T}) + \mathbf{V} \cdot \nabla T \right) + \omega \frac{\partial S}{\partial p} = Q_1 \tag{A.1e}$$

$$\frac{\partial q}{\partial t} + \mathbf{V} \cdot \nabla q + \omega \frac{\partial q}{\partial p} = Q_2 \tag{A.1f}$$

where Q_1 and Q_2 are the apparent heat and moisture sources and sinks, respectively (Yanai et al., 1973). The column integrals of Q_1 and Q_2 are $\langle Q_1 \rangle = P - R$ and $\langle Q_2 \rangle = E - P$.

We can rewrite the thermodynamic energy and moisture equations (Eqs. A.1e and A.1f) by expressing the vertical velocity as $\omega(x, y, p, t) \approx D(x, y, t)\Omega(p)$, where D is the horizontal divergence field and Ω is a structure function corresponding to deep convection.

$$C_p \left(\frac{\partial T}{\partial t} + \varepsilon (T - \bar{T}) + \mathbf{V} \cdot \nabla T \right) + D\Omega \frac{\partial S}{\partial p} = Q_1 \tag{A.2a}$$

$$\frac{\partial q}{\partial t} + \mathbf{V} \cdot \nabla q + D\Omega \frac{\partial q}{\partial p} = Q_2 \tag{A.2b}$$

Equations (A.2a) and (A.2b) are merged by eliminating D to form the following latent energy equation

$$\frac{\partial q}{\partial t} + \mathbf{V} \cdot \nabla q = Q_2 - (Q_1 - \Delta T) \left(\Omega \frac{\partial q}{\partial p} \right) \left(\Omega \frac{\partial S}{\partial p} \right)^{-1}$$

where

$$\Delta T = C_p \left(\frac{\partial T}{\partial t} + \varepsilon (T - \bar{T}) + \mathbf{V} \cdot \nabla T \right)$$

By separating Q_2 into its contribution from condensation and surface latent heat flux, $Q_2 = E - Q_c$, and Q_1 into its convective and radiative parts, $Q_1 = Q_c + Q_r$, we can write:

$$\frac{\partial q}{\partial t} + \mathbf{V} \cdot \nabla q = -\hat{M} Q_c - (1 - \hat{M})(Q_r - \Delta T) + E \tag{A.3a}$$

where

$$\hat{M} = 1 - \left(\Omega \frac{\partial q}{\partial p} \right) \left(\Omega \frac{\partial S}{\partial p} \right)^{-1} \tag{A.3b}$$

The field variables in the equations above are linearized by separating them into time-mean and anomaly fields $q = \bar{q} + q'$. The scaling values for the mean state and MJO-related anomalies, shown in Table 3, are consistent with observations and reanalysis data (Kiladis et al. 2005; Benedict and Randall 2007; Adames and Wallace 2015, among others). The moisture perturbations are much smaller (i.e. smaller by an order of magnitude) than the mean moisture field:

$$|q'| \ll |\bar{q}|$$

However, because the mean tropical moisture field is large, then small perturbations in moisture lead to anomalies in precipitation (latent heating) that are comparable (i.e. smaller, but not by an order of magnitude) to the mean precipitation (Bretherton et al., 2004). Since the anomalous heating is large and the mean tropical flow weak, then it follows that the wind response to anomalous heating is of similar magnitude than the mean flow

$$|\bar{u}| \sim |u'|$$

By scaling the equations with the values in Table 3, it can be verified that the leading terms in the primitive equations are as follows

$$\frac{\partial u'}{\partial t} + \varepsilon u' - \beta y v' = -\frac{\partial \phi'}{\partial x} \tag{A.4a}$$

$$\beta y u' = -\frac{\partial \phi'}{\partial y} \tag{A.4b}$$

$$\frac{\partial \phi'}{\partial p} = -\frac{R_d T'}{p} \tag{A.4c}$$

$$C_p \varepsilon T' + D' \Omega \frac{\partial \bar{S}}{\partial p} = Q'_c - Q'_r \tag{A.4d}$$

$$\frac{\partial q'}{\partial t} + v' \frac{\partial \bar{q}}{\partial y} = -\hat{M} Q'_c - (1 - \hat{M})(Q'_r + C_p \varepsilon T') + E' \tag{A.4e}$$

It is worth noting that we have kept the Newtonian cooling term in Eq. (A.4d), while the corresponding term in Eq.(A.4e) has been dropped. Our scaling shows that the Newtonian cooling term in the thermodynamic energy equation is smaller than other terms in Eq. (A.4d), but not by an order of magnitude. In the moist static equation, the contribution of newtonian cooling is comprised of temperature anomalies which increase in magnitude with distance from the equator (see Fig. 5.1) multiplied by $\bar{M}_q$, which decays exponentially with distance from the equator. This offsetting of the two terms causes newtonian cooling to be an order of magnitude smaller than the other terms in the moisture budget. By applying the meridional and vertical truncation shown in the following section, and adding the terms involving frictional convergence F' and modulation of high frequency eddies ψ'_q to Eq. (A.4e), Eq. (A.4) becomes Eq. (1).

The time tendency in Eqs. (A.4a) implies a solution that is composed of a steady state wave response (Gill, 1980), and free propagating waves. It was shown by Heckley and Gill (1984) that these solutions are separable, and can be written as

$$u' = u'_s + u'_f$$

Table A.1: Values used in the scaling of the primitive equations.

Variable	Symbol	Value/Units
Zonal scale	Δx	10^7 m
Meridional scale	Δy	10^6 m
Vertical scale	Δp	10^5 Pa
Timescale	Δt	10^6 s
Mean and anomalous zonal winds (u',$\bar{u}$)	U	10^0 m s^{-1}
Mean and anomalous meridional winds (v',$\bar{v}$)	V	10^{-1} m s^{-1}
Mean and anomalous vertical velocity (ω',$\bar{\omega}$)	W	10^{-2} Pa s^{-1}
Geopotential anomaly	$\Phi \sim cU$	10 m^2 s^{-2}
Temperature anomaly	$T \sim cU/R_d$	10^{-1} K
Anomalous latent heat	q'	10^2 J m^2
Mean Latent heat	$\bar{q}$	10^3 J m^2
Gross moist stability parameter	$\hat{M}$	10^{-1}
Heating from condensation	Q_c	10^{-3} J kg^{-1} s^{-1}
Radiative heating	$Q_r \sim rQ_c$	
Evaporative cooling	Q_e	10^{-4} J kg^{-1} s^{-1}
Rayleigh friction coefficient	ε	10^{-6} s^{-1}
Vertical change in mean dry static energy	$\Delta\bar{S}$	10^4 J kg^{-1}
Vertical change in anomalous dry static energy	$\Delta S'$	10^2 J kg^{-1}

where the subscript s denotes the steady-state component, while the subscript f denotes the free wave component. The free wave solutions are only weakly coupled to the moisture field, as noted by Majda and Stechmann (2009), but when added to the steady-state solution describe the evolution towards steady state from the moment the anomalous heat sources and sinks develop (see Heckley and Gill 1984). Because we are only interested in the moist wave at the time the wind field is in steady state with the heating, these free wave solutions will not be considered, and hence the temporal tendency in u' is omitted in Eq. (5.1a). However, the addition of the free wave solutions may be important when considering MJO initiation.

Appendix B

MERIDIONAL AND VERTICAL TRUNCATION OF THE EQUATIONS

The basic equations shown in Eq. 1 are truncated meridionally and vertically. For the vertical structure, only a single basis function is used, as in Neelin and Zeng (2000). We choose parabolic cylinder functions $\mathcal{D}_j$ to represent meridional variations, as in Majda and Shefter (2001); Majda and Khouider (2001); Majda and Stechmann (2009) and many others. Parabolic cylinder functions have the following equation

$$\mathcal{D}_j(\xi) = 2^{-j/2}\mathcal{H}_j\left(2^{-1/2}\xi\right)\exp\left(-\frac{\xi^2}{4}\right) \tag{B.1a}$$

$$\mathcal{H}_j(\xi) = (-1)^j \exp\left(\xi^2\right)\frac{d^j}{d\xi^j}\left\{\exp\left(-\xi^2\right)\right\} \tag{B.1b}$$

where $\mathcal{H}_j$ is the jth order Hermite polynomial. The expansion of the perturbation fields takes the following form

$$u'(x,y,p,t) = \left\{\sum_{j=1}^{\infty} u'_j(x,t)\mathcal{D}_j\left(yR_e^{-1}\right)\right\}\Lambda(p) \tag{B.2a}$$

$$v'(x,y,p,t) = \left\{\sum_{j=1}^{\infty} v'_j(x,t)\mathcal{D}_j\left(yR_e^{-1}\right)\right\}\Lambda(p) \tag{B.2b}$$

$$\omega'(x,y,p,t) = \left\{\sum_{j=1}^{\infty} D'_j(x,t)\mathcal{D}_j\left(yR_e^{-1}\right)\right\}\Omega(p) \tag{B.2c}$$

$$\phi'(x,y,p,t) = \left\{\sum_{j=1}^{\infty} \phi'_j(x,t)\mathcal{D}_j\left(yR_e^{-1}\right)\right\}\Lambda(p) \tag{B.2d}$$

$$T'(x,y,p,t) = \left\{ \sum_{j=1}^{\infty} T'_j(x,t)\mathcal{D}_j\left(yR_e^{-1}\right) \right\} a(p) \tag{B.2e}$$

$$q'(x,y,p,t) = \left\{ \sum_{j=1}^{\infty} q'_j(x,t)\mathcal{D}_j\left(yR_e^{-1}\right) \right\} b(p) \tag{B.2f}$$

The vertical velocity field is defined as in Neelin and Zeng (2000), in terms of a divergence field $D = \bar{D} + D'$ and a vertical structure Ω. Ω is bounded by the conditions that it must be equal to zero at the surface and at the tropopause $p_T = 100$. A simple formula that can decribe deep convective ascent with the aforementioned boundary conditions is the following:

$$\Omega(p) = \hat{p}\,(p/p_s)^{-1/2} \sin\left(mp - \theta_p\right) \tag{B.3}$$

where $\hat{p} = 80$ hPa is a reference value for vertical velocity, chosen to facilitate comparison with previous studies (Neelin and Zeng, 2000; Zeng et al., 2000; Sugiyama, 2009a,b), $m = 2\pi/p_\lambda$ is the vertical wavenumber, $p_\lambda = 1800$ hPa is the vertical wavelength, and $\theta_p = 2\pi/p_b$ is a phase shift angle, where $p_b = 100$ hPa . This formula is similar to that used by Haertel et al. (2008) and Kiladis et al. (2009) for the first baroclinic mode in vertical motion, and the resulting profile is similar to the leading EOF of vertical velocity (see Fig. 6 of Adames and Wallace 2014b). The structure Λ is obtained from Ω from the mass continuity equation:

$$\Lambda(p) = -\frac{\partial \Omega(p)}{\partial p} \tag{B.4}$$

while a is defined in accordance to the hydrostatic equation

$$a(p) = \frac{\partial \Lambda(p)}{\partial \ln p} \tag{B.5}$$

The vertical structure of Ω, Λ and a are shown in Fig. B.1*a*, for reference. Finally, the moisture structure function follows a formula similar to Neelin and Zeng (2000)

$$b(p) = (p/p_s)^{H/H_q} \tag{B.6}$$

where $H_q = 3$ km is a moisture scale height, which describes the decrease in moisture with decreasing pressure.

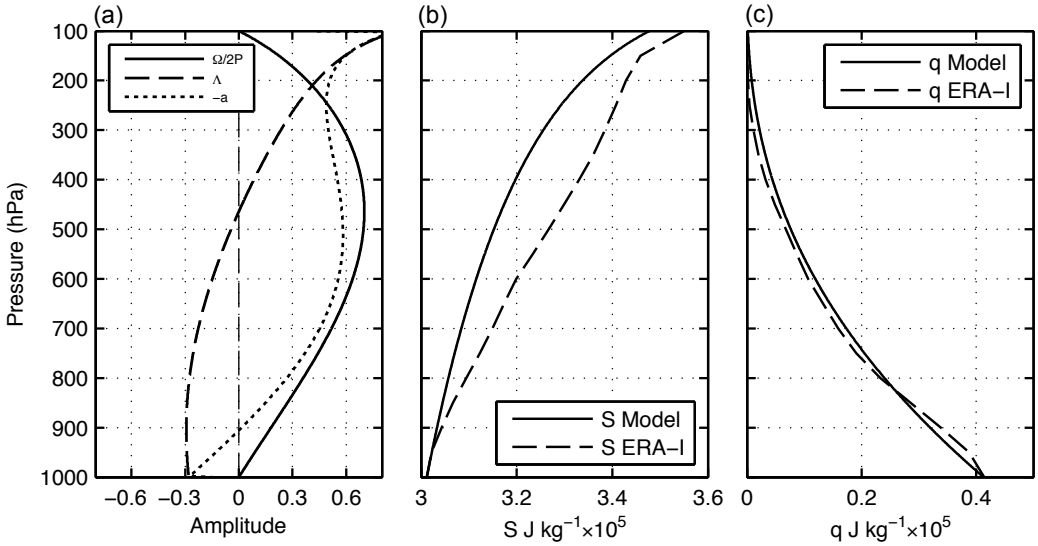

Figure B.1: (a) Vertical profiles of $\Omega/(2\hat{p})$ (solid), Λ (dashed), and $-a$ (dotted). Panels (b) and (c) are vertical profiles of (b) mean dry static energy $\bar{S}$ and (c) latent energy $\bar{q}$ obtained by using Eqs (B.7) and Eq. (B.6) (solid) and from ERA-Interim data (dashed). The profiles for ERA-Interim are averages for all calendar days over the 60-180°E, 10°N/S region. The model moisture profile is averaged over the 10°N/S latitude belt to facilitate comparison.

In order to obtain the mean profiles of $\bar{\phi}$ and $\bar{T}$, the weak temperature gradient approximation (Sobel et al., 2001) is assumed, and meridional variations in $\bar{T}$ and $\bar{\phi}$ are assumed small, such that, to first order, they are only a function of pressure. We can define the mean temperature and geopotential fields as follows

$$\bar{\phi}(p) = gH \ln (p_s/p) \tag{B.7a}$$

$$\bar{T}(p) = \bar{T}_s - \gamma H \ln (p_s/p) \tag{B.7b}$$

where $H = 7.3$ km is the scale height of the tropical atmosphere, $p_s = 1000$ hPa is the surface pressure, $\bar{T}_s = 300$ K is the surface temperature, and $\gamma = 7$ K km^{-1} is the environmental

lapse rate. The values of H and γ are chosen to be consistent with those of Kiladis et al. (2009). The dry static energy $\bar{S}$ obtained this way is compared with ERA-Interim $\bar{S}$ in Fig. B.1*b*. The profiles are similar, though the values obtained from Eq. (B.7) lead to smaller values of $\bar{S}$ in the midtroposphere compared to reanalysis.

The remaining mean state field used in this study, $\bar{q}$, is expressed in terms of the zeroth order parabolic cylinder function, and its variation in the vertical is expressed in terms of b, as in q'

$$\bar{q}(y,p) = \bar{q}_0 \mathcal{D}_0 \left(y R_e^{-1} \right) b(p) \tag{B.8}$$

The vertical profile of $\bar{q}$ is shown in of Fig B.1*c* next to ERA-Interim annual mean $\bar{q}$ averaged over the warm pool sector ($60^\circ - 180^\circ$ E, 10° N/S). A robust fit between the simple model field and reanalysis is observed. By applying these truncations to the scaled primitive equations in Eq. (A.4), we can obtain Eq. (1).

Appendix C

SOLUTION OF THE WAVE RESPONSE TO AN EQUATORIAL HEAT SOURCE

For a heating rate with a meridional profile equal to the zeroth order parabolic cylinder function, $\mathcal{D}_0$, Eqs. (5.1a)−(5.1c) become the dimensional, modal forms of the equations used by Gill (1980), where a response to an equatorially-trapped heat source is comprised solely of Kelvin and n=1 equatorial Rossby waves. As in SM and Wu et al. (2001), these solutions can be written in integral form by using a projection operator G:

$$u'(x,y,t) = \int G_u(x,x^*,y)\left\{P'(x^*,y,t) - R'(x^*,y,t)\right\}dx^* \tag{C.1a}$$

$$v'(x,y,t) = v'_s(x,y,t) + \int G_v(x,x^*,y)\left\{P'(x^*,y,t) - R'(x^*,y,t)\right\}dx^* \tag{C.1b}$$

$$\phi'(x,y,t) = \int G_\phi(x,x^*,y)\left\{P'(x^*,y,t) - R'(x^*,y,t)\right\}dx^* \tag{C.1c}$$

where $v'_s = (8/3)\hat{V}y(P' - R')$ is the Sverdrup balance component of the meridional flow in the absence of Rayleigh dissipation. The projection operators have the following form:

$$G_u(x,x^*,y) = \begin{cases} -\hat{V}e^{-(x-x^*)/L}, & x > x^* \text{ (Kelvin)} \\ (3 - y^2R_e^{-2})\hat{V}e^{3(x-x^*)/L}, & x < x^* \text{ (Rossby)} \end{cases} \tag{C.2a}$$

$$G_v(x,x^*,y) = \begin{cases} 0, & x > x^* \text{ (Kelvin)} \\ -8\hat{V}yL^{-1}e^{3(x-x^*)/L}, & x < x^* \text{ (Rossby)} \end{cases} \tag{C.2b}$$

$$G_\phi(x,x^*,y) = \begin{cases} -\hat{\Phi}e^{-(x-x^*)/L}, & x > x^* \text{ (Kelvin)} \\ -(1+y^2R_e^{-2})\hat{\Phi}e^{3(x-x^*)/L}, & x < x^* \text{ (Rossby)} \end{cases} \tag{C.2c}$$

where $\hat{V}$ and $\hat{\Phi}$ are dimensional constants. The factor of 3 in the exponent of the Rossby wave response reflects the fact that planetary equatorial Rossby waves propagate at 1/3 the group velocity of Kelvin waves. Note that the integrals in Eq. (C.2) incorporate parabolic cylinder functions $\mathcal{D}$ of order 0, 1 and 2 onto it. By using Eqs. (C.2) and (5.10), we can explicitly integrate Eq. (C.1), which yields Eqs. (5.12) and (5.13), and the following structure for ϕ'

$$\phi' = \langle b \rangle \left(\Gamma_{\phi K} + \Gamma_{\phi R}\right) q' \tau_c^{-1} \tag{C.3a}$$

where

$$\Gamma_{\phi K}(k) = -\hat{\Phi}(1+r)\frac{L^{-1} - ik}{L^{-2}+k^2} \tag{C.3b}$$

$$\Gamma_{\phi R}(k) = -\hat{\Phi}(1+r)(1+y^2R_e^{-2})\frac{3L^{-1}+ik}{9L^{-2}+k^2}. \tag{C.3c}$$

VITA

Ángel F. Adames-Corraliza was born in Mayagüez, Puerto Rico (PR). He was raised in the town of San Sebastián, PR. He earned a bachelor's degree in Physics in 2010 from the University of Puerto Rico, Mayagüez (UPRM). He immediately went to graduate school in the department of Atmospheric Sciences where he obtained his M.S. in 2013. Ángel specializes in tropical meteorology, in particular the Madden-Julian Oscillation. He uses a combination of statistical techniques applied to data as well as theory to understand the critical processes that lead to the eastward propagation of the MJO.